UNIVERSIDADE DE BRASÍLIA – UNB

FACULDADE DO GAMA

PROGRAMA DE PÓS-GRADUAÇÃO EM INTEGRIDADE DE MATERIAIS DA ENGENHARIA

NUMERICAL TECHNIQUE APPLIED TO DAMAGE IDENTIFICATION IN BOLTED STRUCTURES USING TIME-DOMAIN DYNAMIC RESPONSES

JALUSA MARIA DA SILVA FERRARI

ADVISOR: PROF. DR. JHON NERO VAZ GOULART
CO-ADVISOR: PROF. DR. SERGIO HENRIQUE DA SILVA CARNEIRO

UNIVERSIDADE DE BRASÍLIA – UNB
FACULDADE DO GAMA

NUMERICAL TECHNIQUE APPLIED TO DAMAGE IDENTIFICATION IN BOLTED STRUCTURES USING TIME-DOMAIN DYNAMIC RESPONSES

JALUSA MARIA DA SILVA FERRARI

ADVISOR: PROF. DR. JHON NERO VAZ GOULART
CO-ADVISOR: PROF. DR. SERGIO HENRIQUE DA SILVA CARNEIRO

MASTER THESIS IN INTEGRITY OF MATERIALS ENGINEERING
ISSUE: 106A/2023

BRASÍLIA/DF, NOVEMBER 2023

UNIVERSIDADE DE BRASÍLIA – UNB
FACULDADE DO GAMA
PROGRAMA DE PÓS-GRADUAÇÃO EM INTEGRIDADE DE MATERIAIS DA ENGENHARIA

NUMERICAL TECHNIQUE APPLIED TO DAMAGE IDENTIFICATION IN BOLTED STRUCTURES USING TIME-DOMAIN DYNAMIC RESPONSES

JALUSA MARIA DA SILVA FERRARI

MASTER'S THESIS SUBMITTED TO THE POSTGRADUATE PROGRAM IN INTEGRITY OF MATERIALS ENGINEERING AT UNIVERSITY OF BRASILIA, AS PART OF THE REQUIREMENTS FOR OBTAINING A MASTER'S DEGREE.

APPROVED BY:

PROF. DR. JHON NERO VAZ GOULART
ADVISOR - CAMPUS GAMA/UNIVERSIDADE DE BRASÍLIA

PROF. DR. SERGIO HENRIQUE DA SILVA CARNEIRO
CO-ADVISOR - CAMPUS GAMA/UNIVERSIDADE DE BRASÍLIA

DR. MARIA ALZIRA ARAÚJO NUNES
EXAMINER - CAMPUS GAMA/UNIVERSIDADE DE BRASÍLIA

DR. LIÉRCIO ANDRÉ ISOLDI
EXAMINER - CAMPUS CARREIROS/UNIVERSIDADE FEDERAL DO RIO GRANDE

ATA DE SELEÇÃO ASSINADA ELETRONICAMENTE VIA SISTEMA SEI, DOCUMENTO 10491607, PROCESSO 23106.119007/2023-16.

BRASÍLIA/DF, NOVEMBER 2023

CATALOGRAPHIC CARD

FERRARI, JALUSA MARIA DA SILVA
Numerical Technique Applied to Damage Identification in Bolted Structures using Time-Domain Dynamic Responses [Distrito Federal], 2023.
87p., 210 × 297 mm (FGA/UnB Gama, Master in Integrity of Materials Engineering, 2023).
Master Thesis – University of Brasília. Faculty of Gama.

1. Inverse problem	2. Damage identification
3. Structural dynamic	4. Uncertainties
I. FGA/UnB.	II. Title (series).

REFERENCE

FERRARI, JALUSA MARIA DA SILVA (2023). Numerical Technique Applied to Damage Identification in Bolted Structures using Time-Domain Dynamic Responses. Master's Thesis in Integrity of Engineering Materials, Publication 106A/2023, Postgraduate Program, Faculty of Gama, University of Brasília, Brasília, DF, 87p.

ASSIGNMENT OF RIGHTS

AUTHOR: Jalusa Maria da Silva Ferrari

TITLE: Numerical Technique Applied to Damage Identification in Bolted Structures using Time-Domain Dynamic Responses

DEGREE: Master

YEAR: 2023

jalusaferrari@gmail.com

Brasília, DF – Brazil

”A scientist in his laboratory is not just a technician: he is also a child faced with natural phenomena that impress him like fairy tales.”

Marie Curie

Dedico esta dissertação à minha mãe e à minha avó, com todo amor.

ACKNOWLEDGEMENTS

To God, for guiding me and taking care of me at all times.

To my mother, Vanuzia Silva, my grandmother, Maria Alves, my godmother Vanilce, my aunt Vaneuma, and my sister, for their constant belief in me, encouragement and support throughout my entire journey.

I express my deep gratitude to my advisors, Professor Jhon Goulart and Professor Sergio Carneiro, as well as Professor Ariosto Bretanha. Their wisdom, guidance and patience were fundamental to the development of this work.

To my friends, especially Jessica Maciel and Monica Damasceno, who were always by my side providing moments of lightness during my academic journey.

To my coworkers who encouraged me to complete this stage, with special recognition to Ivan Chaves, for believing in the importance of this research.

To my partner, Iago Cintra, to whom I dedicate special thanks for his constant support and assistance throughout this journey.

I extend my gratitude to the academic community and colleagues at the GMEC laboratory, who shared countless significant moments during the completion of this work.

To those who believed in me in moments of doubt and to those who challenged me in periods of growth, my sincere thanks.

To CAPES, FAP-DF and DPG, for the fundamental financial support in the development of this work.

This work is dedicated to all of you, whose support and inspiration shaped this achievement. Thank you so much for being part of my journey.

RESUMO

TÉCNICA NUMÉRICA APLICADA À IDENTIFICAÇÃO DE DANOS EM ESTRUTURAS PARAFUSADAS USANDO RESPOSTAS DINÂMICAS NO DOMÍNIO DO TEMPO

Em diversos campos da engenharia, a necessidade de identificar e monitorar danos em estruturas complexas e de difícil acesso ainda apresenta um grande desafio para as técnicas não destrutivas de monitoramento existentes. Os métodos baseados em *Structural Health Monitoring* (SHM) demonstram o potencial de identificar e monitorar danos em estruturas através de um sistema *on-board* de comparação imediata com uma base de dados existentes. Nesse sentido, o presente trabalho propõe um estudo numérico usando método de predição de dano SHM com a solução do problema inverso. A estrutura de estudo foi uma viga engastada com condições de contorno elásticas modelada através de um modelo de baixa ordem de fidelidade. Usando elementos finitos, uma junta aparafusada com 4 parafusos NAS6208-16 foi modelada no *Ansys Parametric Design Language* (APDL) usando o elemento COMBIN14 a partir de 6 rigidezes, onde 3 rigidezes são de torção e 3 são de flexão. Uma análise de convergência foi realizada, resultando na avaliação da modelagem do problema com condições elásticas e em uma discretização de 20 elementos usando funções de interpolação quadrática entre os nós. Os danos da viga foram definidos através de uma perda de torque de aperto nos parafusos variando de 5% a 50%, resultando em uma perda de rigidez na conexão da viga. Foi proposto um índice-R capaz de avaliar os resultados com base na aceleração na direção vertical e normalizado em relação ao sinal de aceleração máxima coletada. Simulações transientes usando superposição modal foram realizadas para avaliar a robustez do índice-R. Como primeiro resultado, observou-se que o índice-R selecionado é robusto em relação à mudança na posição de aplicação da força e na quantidade e distribuição de nós para leitura de dados. Foi possível aproximar os resultados através de uma única curva quadrática, a partir das médias obtidas do índice-R. Foram traçadas curvas de limite de confiança de 95% a partir dos valores médios, possibilitando uma tentativa na solução do problema inverso. Com a adição de ruído de 1% a 5% nos dados obtidos de aceleração vertical, a detecção de perda de torque em baixos níveis foi prejudicada. Apesar disso, através da análise do intervalo de confiança, o método ainda se mostrou capaz de identificar satisfatoriamente perdas de torque acima de 25%, principalmente quando foi considerado o uso da média dos valores obtidos nos sensores para o cálculo do índice-R.

Palavras-chave: problema inverso, identificação de dano, dinâmica de estruturas, incertezas, SHM.

ABSTRACT

In several engineering fields, the need to identify and monitor damage in complex and difficult-to-access structures still presents a major challenge for existing non-destructive monitoring techniques. Methods based on Structural Health Monitoring (SHM) demonstrate the potential to identify and monitor damage to structures through an on-board system for immediate comparison with an existing database. In this sense, the present work proposes a numerical study using the SHM damage prediction method with the solution of the inverse problem. The study structure was a fixed beam with elastic boundary conditions modeled using a low-order fidelity model. Using finite elements, a bolted joint with 4 NAS6208-16 bolts was modeled in Ansys Parametric Design Language (APDL) using the COMBIN14 element from 6 stiffnesses, where 3 stiffnesses are torsional and 3 are flexural. A convergence analysis was performed, resulting in the evaluation of the modeling of the problem with elastic conditions and discretization of 20 elements using quadratic interpolation functions between the nodes. Beam damage was defined as a loss of tightening torque on the bolts ranging from 5% to 50%, resulting in a loss of stiffness in the beam connection. An R-index capable of evaluating results based on acceleration in the vertical direction and normalized with the maximum acceleration signal collected was proposed. Transient simulations using modal superposition were performed to evaluate the robustness of the R-index. As a first result, it was observed that the selected R-index is robust about changes in the force application position and in quantity and distribution of nodes for data reading. It was possible to approximate the results through a single quadratic curve, based on the averages obtained from the R-index. 95% confidence limit curves were drawn from the average values, enabling an attempt to solve the inverse problem. With the addition of noise of 1% to 5% in the vertical acceleration data obtained, the detection of torque loss at low levels was impaired. Despite this, through the analysis of the confidence interval, the method was still capable of satisfactorily identifying torque losses above 25%, especially when the use of the average of the values obtained from the sensors was considered to calculate the R-index.

Keywords: inverse problem, structural dynamics, damage identification, uncertainties, SHM.

Contents

List of Tables

List of Figures

LIST OF NOMENCLATURES AND ABBREVIATIONS

APDL Ansys Parametric Design Language

BEM Boundary Element Method

CNN Convolutional Neural Network

DOF Degree of Freedom

DNN Deep Neural Network

ECPT Eddy Current Pulsed Thermography

FEM Finite Element Method

ICAF International Committee on Aeronautical Fatigue

NAS National Aerospace Standard

NDT Non-Destructive Testing

PoD Probability of Detection

RUL Remaining Useful Life

SHM Structural Health Monitoring

LIST OF SYMBOLS

$\mathbf{A}$	Tensile Stress Area
$\mathbf{A_m}$	Effective Material Area
$\mathbf{A_t}$	Threaded Portion Area
$\mathbf{A_d}$	Unthreaded Portion Area
$\mathbf{C}$	Stiffness Constant
$\mathbf{C_b}$	Bolted Joint Constant
$\mathbf{CI}$	Confidence Interval
$\mathbf{d}$	Bolt Diameter
$\mathbf{E}$	Modulus of Elasticity
$\mathbf{E_b}$	Bolt Modulus of Elasticity
$\mathbf{E_m}$	Material Modulus of Elasticity
$\mathbf{F}$	Applied Force
$\mathbf{f}$	Force Vector
$\mathbf{K}$	Spring Stiffness
$\mathbf{K_b}$	Bolt Stiffness
$\mathbf{K_m}$	Material Stiffness

$\mathbf{K_i}$	Torque Coefficient
$\mathbf{K_j}$	Joint Stiffness
$\mathbf{K_c}$	Set Joint Stiffness
$\mathbf{K_{rot}}$	Rotational Stiffness
$\mathbf{K_u}$	Flexural Stiffness
$\mathbf{L}$	Beam Length
$\mathbf{l}$	Effective Length of the Bolt
$\mathbf{l_d}$	Length of Unthreaded Portion in Grip
$\mathbf{l_t}$	Length of Threaded Portion in Grip
$\mathbf{M}$	Mass Matriz
$\mathbf{N}$	Samples Number
$\mathbf{n}$	Matrix Dimension
$\mathbf{q}$	Vector of Generalized Coordinates
$\mathbf{R}$	Normalized Residue
$\mathbf{R_{NN}}$	Autocorrelation Function of a Signal
$\mathbf{S_{NN}}$	Power Spectral Density of the Noise

$\mathbf{s}$	Standard Deviation
$\mathbf{T_i}$	Initial Torque
$\mathbf{t}$	Time
$\mathbf{u}$	Mode Shape Vector
$\overline{\mathbf{X}}$	Population Mean
$\mathbf{y}$	Distante Between Bolt and Beam Center in y-direction
$\mathbf{Z}$	Z-score of Confidence Level
δ	Delta Dirac
ϵ	Percent Error
τ	Torque Loss
$\omega_\mathbf{n}$	Natural Frequency

1 INTRODUCTION

1.1 BACKGROUND

Environmental and operational conditions have a great influence on the behavior and durability throughout the life cycle of structures, causing changes in the material and geometric properties, such as modulus of elasticity, boundary conditions, cross-sectional area, and system integrity (Razavi and Hadidi, 2021). Aerospace and automotive vehicles operate under a wide variety of conditions, often unpredictable, making it extremely difficult to predict all operational scenarios (Ross, 2016).

Analyzing some key parameters makes it possible to provide the state of structure integrity. Structural Health Monitoring (SHM) tools make the understanding of the damage through continuous observation of the structure. Detecting damage before the structure fails would make it last longer, be safer, more reliable, and decrease maintenance cost (Chaupal and Rajendran, 2023).

SHM is a technique that uses sensors to continuously monitor the integrity of a structure. The concept behind SHM is to create a system analogous to the human nervous system capable of processing all information received in real time through sensors.

The SHM can be used in many engineering applications to meet safety and performance requirements. The commercial aviation industry seeks solutions capable of detecting damage to metal and composite structures that justify the investment, given that a large part of the operating cost of an aircraft comes from the maintenance program (Rulli *et al.*, 2016).

However, in the human body, there are some singularities due to the absence of nerves in some areas, such as the bones. Therefore, a bone fracture could go unnoticed or cause only minor discomfort, all due to a lack of nerves or an 'SHM system' in the bones (Speckmann and Henrich, 2004). Therefore, it is important to position sensors in strategic regions in order to optimize information reading.

For an aircraft, for example, sensors act like nerves and must be strategically positioned to monitor more critical or strategic areas to ensure the integrity of the structure, as presented in Figure 1.1. If any damage occurs, these sensors would be able to detect the damage at an early stage and even present a prognosis of the structure (Speckmann and Henrich, 2004).

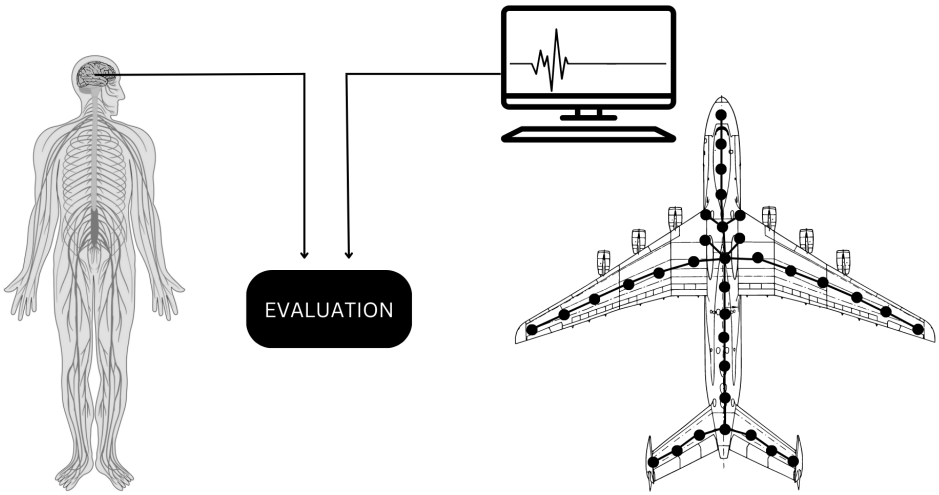

Figure 1.1. SHM system compared to human nervous system. Adapted from Speckmann and Henrich (2004).

SHM is an active area of research and considerable research efforts have been dedicated to improving the capability of damage identification. As a result, SHM is constantly evolving, offering promising solutions to address safety, optimize maintenance strategies, and extend the lifespan of critical infrastructures (Cao *et al.*, 2023). With that in mind, it's important to present some definitions of damage detection levels in the context of SHM. According to Sivasuriyan *et al.* (2021), the damage prediction process is built upon 5 layers of complexity:

Stage 1: Recognizing the presence of damage;

Stage 2: Recognizing both the presence and location of damage;

Stage 3: Recognizing the presence, location, and type of damage;

Stage 4: Recognizing the presence, location, type, and severity of damage;

Stage 5: Where a comprehensive understanding of the damage is establish, along with the prediction on damage future behavior.

Proceeding through the levels, the degree of complexity of the system also increases.

In the context of SHM, severity refers to the magnitude or degree of damage correlated with safety factors established by material standards. This assessment provides a deeper understanding of the analyzed structure, allowing a characterization of the structure focused on its security. This phase, for instance, could help in prioritizing damage repair efforts.

The lack of knowledge to generate a prognosis in Level 5, also known as prognosis level, requires an advanced data processing software and real condition evaluation (Sivasuriyan *et al.*, 2021). Prognosis is defined as predicting or forecasting the future condition and behavior of a structure based on the analysis of its current health data. It involves using data and

models to anticipate how the structure might degrade or develop issues over time, helping to make informed decisions about maintenance and potential risks (Moradi *et al.*, 2023).

As summarized in Figure 1.2, an SHM system may be able to provide two features: diagnostic and prognostic. For the diagnosis stage, it is necessary to locate, identify and quantify the damage or issues in the structure. For diagnosis, it is necessary to detect, locate, and quantify the damage or issues in the structure. These provide information about the presence, location, and severity of damage. For the prognosis stage, all previous steps are well defined and the Remaining Useful Life (RUL) can be determined (Giannakeas *et al.*, 2023).

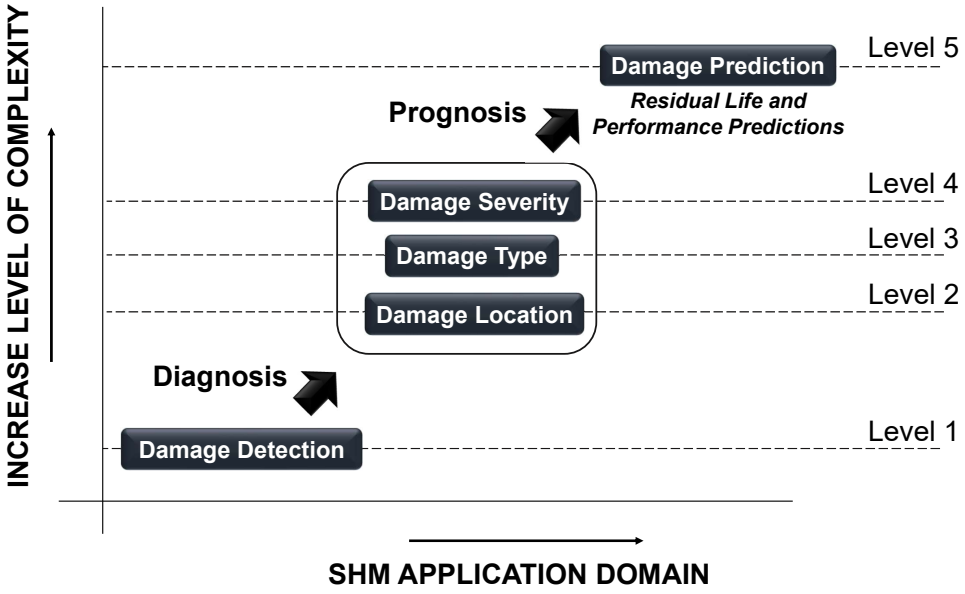

Figure 1.2. Overview of SHM damage prediction process. Adapted from Sivasuriyan *et al.* (2021).

There are two different approaches used to numerically represent a complex system: model-based models and physics-based models. Model-based methods can be used to offer relevant insights into the structure health in the context of SHM (Concli *et al.*, 2021). Model-based models are derived from only a data pattern given by some mathematical approach. They can be advantageous in reducing the requirement for awareness of the total physical characteristics of a structure, as engineers and analysts develop models and make predictions without extensive knowledge of the complex features involved in the system (Bender, 2023).

When using the physical principles, laws and equations to discretize a structure, the numerical approach is based on the physics of the problem. Developing a physics-based model requires a thorough understanding of the pertinent physical principles governing the system and expertise in employing mathematical techniques. Moreover, one must account for real-

world complexities and uncertainties to develop models that could reflect a higher degree of realism and reliability. For this reason, methods based on the physics of the problem are limited to simpler problems with well-defined boundary conditions (Cunha *et al.*, 2023).

As shown in Figure 1.1, sensors are used to collect data that can be used for a model-based approach, which is the case of this study. However, it should be noted that sensors can provide incorrect information due to a lack of calibration or sensor failures. This is why the modeling must be able to identify the damage despite the presence of measurement uncertainties. Uncertainties can be found not only in sensor measurements but also in loading conditions and environmental effects, limiting the analysis efficiency. To reduce the effect of uncertainties, a probabilistic approach may be used through the Probability of Detection (PoD) studies. The PoD probabilistically defines the capability of a Non-Destructive Testing (NDT) method in damage analysis, originally proposed for military maintenance use, it has been used in other maintenance fields such as aeronautics and in nuclear power plant components (Chen *et al.*, 2021).

This study was developed as a representative model of an airplane wing using a beam connected with elastic boundary conditions simulating real fasteners in a bolted joint. As Spinelli (2004) highlighted, a bolted joint can be easily assembled and disassembled, and can be removed to facilitate inspection, repairs or replacement of the entire part. Also, the most common failures in aeronautical structures occur precisely in joints, so they must be well designed during the project to guarantee a correct load transmission between the joined structures.

Bolted joint structures under vibration have been deeply studied and their mechanical behavior is of great interest in the context of engineering machinery (Liao *et al.*, 2016). Nikravesh and Goudarzi (2017) stated the advantages of using bolts as the ability to bear relatively heavy loads at moderate costs, simple installation process and acceptable reliability. For these reasons, they are commonly used structures, as shown in Figure 1.3. To satisfy the fatigue requirements, the joint design must either 1) keep stress levels below the limit or 2) ensure that the crack growth will be slow, to ensure that the life cycle of the component will be greater than the design service (Adeppa *et al.*, 2012).

(a) Steel structure joints.

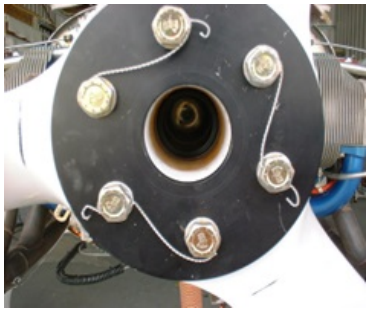

(b) Propeller joints.

(c) Vehicle suspension joints.

Figure 1.3. Examples of the use of bolted joints in engineering.

The correct understanding of joint parameters and how they affect joint behavior through supported cycles is extremely relevant. As mentioned by Popp (1998), ”the joint models must

be as simple as possible and as accurate as necessary". Among the possibilities of failure with bolts, the main ones are stress concentration, cracks, corrosion, and looseness. Over time, bolted joints must be periodically inspected, maintained and replaced due to fatigue. In assembled structures, the dynamic behavior is determined by the load or moment transfer behavior in the joint (Gaul and Nitsche, 2001).

1.2 JUSTIFICATION

The problem under analysis in this work arose from the interests observed in the commercial aviation industry, according to the Technological Demonstrator Platform project written by Bretanha (2020). According to the author, research involving inverse methods and uncertainties presents a promising path for exploration within the scope of interests of the International Committee on Aeronautical Fatigue (ICAF) in Brazil. For instance, in engineering, inverse methods can be employed to reconstruct material properties, optimize designs, or identify flaws in structures. By using inverse methods, valuable information can be obtained only from observed data, which is particularly relevant in situations where direct measurements may be challenging or limited.

The inverse problem consists of locating the damage in the damaged structure from some available information, simulating a real-life scenario, and considering the uncertainties associated with sensor information. Frequently, this involves learning unclear information about the health and state of the structure. On the other hand, the forward problem involves obtaining data from a known model with boundary conditions defined based on a physical theory basis.

A Finite Element Method (FEM) approach was selected to model a complex structure as the wing-fuselage connection through a low-order of fidelity model, to generate a fast solution to perform multiple runs. The use of finite elements to numerically simulate an inverse problem with bolted joints is justified by the ability of this approach to model the complex behavior of joints under different conditions. Finite elements allow the accurate representation of the mechanical characteristics of the materials and the interactions between the components of the joint. Furthermore, this approach offers the flexibility to vary parameters such as torque, load, and geometry, enabling analysis of joint responses under different scenarios.

When simulating an inverse problem, where one seeks to deduce the unknown parameters from observed data, finite elements facilitate the comparison between simulated results and realistic data, allowing the precise identification of characteristics such as stiffness, load, and torque, fundamental for the understanding and optimizing the behavior of bolted joints in a variety of applications. Figure 1.4 briefly presents the problem that will be presented in this work. It is important to highlight that other models for solving the inverse problem may exist, using or not using the finite element modeling step, or even including other steps.

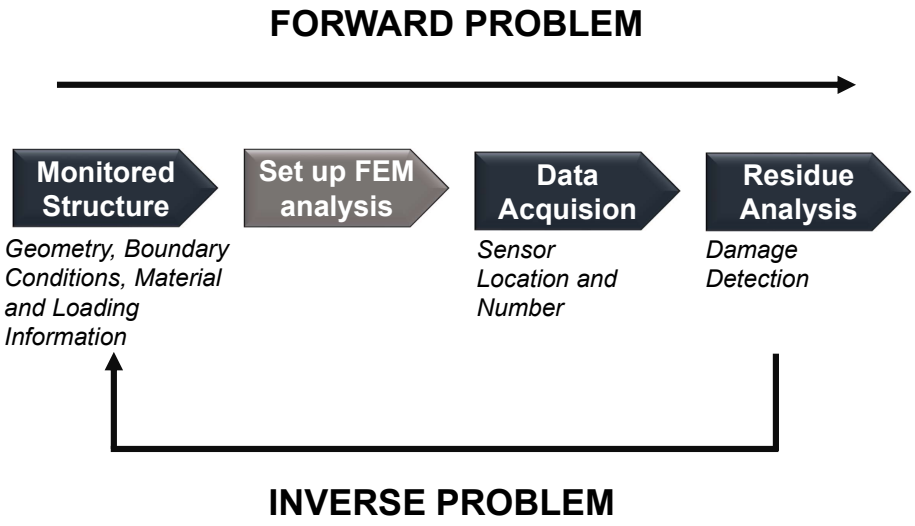

Figure 1.4. Forward and inverse modelling with model-based approach using FEM.

Several aircraft use bolted joints in wing connections, including the Cessna 172, some models of the Boeing 737, some designs of the Airbus A320 series, and some of the Embraer E-Jet jets, for example. The number of bolts used may vary according to aircraft size, wing type, construction conditions, or design limitations.

In aeronautical design, a complex study involving a detailed analysis of loads, materials, and safety requirements is met. In the present study, the joint construction used an aeronautical bolt in a robust architecture, since the joint definition was used only to calculate the stiffness coefficients. Thus, the elaboration and detailing of the joint arrangement project is not part of the scope of this work.

Connection losses were applied and controlled through stiffness parameters. Residuals, based on the response obtained from the healthy and 'damaged' beam, where 'damaged' refers to the loss of stiffness in the joint, were used as an attempt to observe a pattern of responses in the time domain. To replicate real-world circumstances with uncertainties in measurements, Gaussian White noise was added to the captured data. All analyses in the present study were performed in the time domain. Finally, an approximation of the solution of the inverse problem was proposed using a polynomial equation of the simplified metamodel.

1.3 OBJECTIVES

1.3.1 General Objective

Monitoring torque loss of a beam-like structure and its connection with elastic boundary conditions with a numerical model by solving an inverse problem with a low order of fidelity

model.

1.3.2 Specific Objectives

- Model the forward and inverse problem of the beam with elastic connection;
- Model a bolted joint and present a procedure for calculating rotational and flexural stiffness;
- Solve the inverse problem from time response residues to estimate torque loss with associated uncertainties.

1.4 TEXT ORGANIZATION

The document's organization begins with an ”Introduction” providing theoretical context, justification, and objectives. The ”Bibliographic Review” provides existing research on damage identification, stiffness definition in bolted joints, and modeling with uncertainty. The ”Theoretical Foundation” section outlines basic concepts including bolt and joint stiffness, followed by the ”Methodology” section detailing finite element modeling, torque-induced damage, and residue analysis. ”Results and Discussions” present findings on refinements, joint stiffness, residue analysis, and confidence bounds. The ”Conclusion” summarizes outcomes and suggests future research, and ”Appendices” offer supplementary materials. The ”Reference List” cites sources used.

2 BIBLIOGRAFIC REVIEW

2.1 DAMAGE IDENTIFICATION

Hou and Xia (2021) made a review on vibration-based damage identification methods over the past 10 years. Vibration-based methods identify structural changes by variations in the vibration spectrum and are considered a global method. According to Hou and Xia (2021), this methodology can be classified into three categories: 1) time domain, which uses time-history responses, 2) frequency domain, which uses modal parameters, and 3) time-frequency domain methods, which is based on time-frequency tools. Different techniques were presented by the authors where the applicability and effectiveness depends on damage type, structural configuration, and available data.Hou and Xia (2021) mentioned that statistical time series methods, such as the one that will be used in this work, are successful in discovering the presence and location of damage, and are limited to levels 1-2 due to their limitation in finding damage severity. It was discussed that due to the variety of applications of a structure, a universal method capable of identifying all damage types remains yet to be developed. The authors also affirm that only a few algorithms can predict the remaining service life of structures, which is the last stage in damage detection. Therefore the prognosis stage is still a challenging step in this field.

Li *et al.* (2021) proposed a damage identification method for solving an inverse problem using an element with a low-order model. The study used the strain field and the complete modal data of a cantilever plate with a concentrated force of 98 N applied at the right end. The plate was subjected to single-damage and multi-damage conditions. The FEM model was generated using SHELL181 elements with boundary conditions as a fixed constraint applied to the left end. Numerical results indicated that the methodology used was capable of reconstructing the deformation. The strain mode difference was capable of identifying the damage with errors less than 5%. The authors found that the qualitative damage degree identification with single damage conditions is better than with multi-damage conditions. This happened due to the damage index, which was defined as the difference between the damaged positions information, not allowing to qualitatively identify damages. Still, the authors noticed a significant sensitivity using the inverse method to find the damage, but for better results, the authors recommended a higher fidelity model concurrently with the acquisition of more node data.

Zhan *et al.* (2021) analyzed the influence of the randomness of structural parameters on the accuracy of Convolutional Neural Network (CNN) used in structural damage identification. The authors presented the definition of CNN based on damage identification, which should be considered in practical engineering projects and it is an important step in training the network.

The finite element model used was a simply supported concrete beam with 20 beam elements. To simulate damage, some reduction of material stiffness EI was used. The results showed that the randomness of structural parameters affects the recognition accuracy of CNN, meaning that the randomness effects cannot be ignored. Also, the combination of the randomness of parameters will increase the impact on accuracy, and the mass and elastic modulus play a major role in this subject. As mentioned by the authors, under the combined effect of random structural parameters and sampling noise, the results showed that CNN presented a notable anti-noise ability.

Fernandez-Navamuel *et al.* (2022) proposed a supervised deep learning approach with FEM for damage identification in bridges. The method used the stiffness variations to identify the presence of damage and some experimental measurements were employed to adjust the properties of the parametrization. By grouping the structural properties, they developed a database including different scenarios with the presence of measurement errors. Then, the authors validated the methodology with two full-scale cases to reduce errors in damage location and severity using the proposed Deep Neural Network (DNN). DNN methods require a training phase to learn the relationship between the structure and its healthy response. The work focused on the development of the offline part of the DNN training, in which all the required steps to build the damage identification were included. The results showed that the neural network was capable of providing adequate predictions even with the measurement errors. The authors stated that the proposed method allows a feasible adaption to other structures with complex parametrizations and structural particularities.

Giannakeas *et al.* (2023) presented a study with SHM for estimating the residual strength of damaged composite panels. The authors developed a routine with two phases: an initial offiline phase to creat database and training models and an online phase to realibility assessment. It combines physics-based and data-driven models as simulated SHM damage data were compared with experimental observations to enhance prediction accuracy. Also, due to this methodology it was possible to capture model uncertainties during tests. The authors used a Damage Index based on the amplitude of the residual signal to compare damage-free state and damaged panels. The method considers various uncertainties, making it a valuable tool for assessing structural integrity and guiding maintenance decisions.

2.2 BOLTED JOINT STIFFNESS

Gaul and Nitsche (2001) provided an overview of the methods that characterize the nonlinear transfer behavior of bolted joints over time. The authors described the mathematical models for the sliding friction interface in a joint connection, highlighting that the joint contact area is rough, and the true area is much smaller than the apparent contact area which leads to high local normal pressure. Depending on the type of application, a constitutive or phenomenological approach can be chosen to model the joint. If the objective is to perform a local analysis, a constitutive model should be selected for describing the microscale process as the finite element method. The phenomenological joint models with reduced Degree of Free-

dom (DOF) can be used for control tasks and were applied for eg. in research about designing model-based controllers.

Xue *et al.* (2011) developed a numerical analysis using finite elements to observe the mechanical behavior of a composite truss joint in the steel-concrete bridge. According to the authors, there was a lack of literature on the design and construction of the joint. The spring element used to simulate the headed studs was the Ansys COMBIN14, which is the same element that will be used in this work. They were positioned in tangential directions and coupled in the axial directions, and the 2D steel plate was modeled with SOLID45 elements. The stiffness of the spring element in finite element analysis was obtained through the experimental push-out tests. An experimental specimen truss with a scale of 1:2 was built to collect some understanding of the safety and serviceability of the model. The tests used the worst-case load as found by the FEM results to measure strains in the joint model. A stepped loading was used, where 10% of the design load was applied at each step of 10 minutes until 170% of the design load was achieved after 17 load steps. As a result, the authors found that there was a substantial safety threshold for composite joints under 1.7 times the design load. Also, FEM results showed that the headed studs remained in the elastic zone at all load steps. In general, the finite element results showed fairly good agreement with the experimental ones, stating that the finite element analysis was capable of providing relevant data on the study of composite joints.

Liu *et al.* (2013) investigated a simply supported composite truss bridge with a three-dimensional finite element model compared to tested results with a scale of 1:4.5. The authors related fatigue tests and crack appearance, providing a reference for future design of composite joints in composite truss bridges. The composite joints were also represented by a spring element COMBIN14 to simulate shear and axial forces in three directions. Fatigue tests were conducted with 3 cycles per second with a load amplitude of 150 kN in three joints with different connectors: headed studs, concrete dowels, and perforated plate. The fatigue tests showed that repeated cycles gradually reduced the joint stiffness. However, only a few cracks at the steel-concrete interface were observed after 2 million repeated loading cycles, slowly developing as the loading cycles were repeated. Although the cracks could be caused by a failure in bond stress at the interface, no damage to the joint structure was observed despite the reduction in joint stiffness in this area.

Liu *et al.* (2016) made an extensive study about the stability and strength of steel tube-coupler scaffolds with many connection joints using an experimental and finite element model. FE model was used to obtain the stress distribution, strength, and failure modes. As used by Xue *et al.* (2011) and Liu *et al.* (2013), the spring element COMBIN14 was used to model the right-angle couplers, where the spring constant was adopted as the mean initial rotational stiffness obtained from previous coupler tests. Two specimens with a torque of 40 N m were tested experimentally to obtain rotational stiffness. For the numerical simulation, a beam was modeled with Ansys element BEAM188, which also will be used in this work, defined with 10 elements, a number obtained after a convergence study on the model. The failure modes and friction force distributions were obtained from nonlinear analysis. The authors concluded that

the main failure mode of the steel tube coupler was the slipping and the fracture of right-angle couplers. The FEM failure modes and displacement were in agreement with the experimental results with a maximum difference of 11.08%.

Jalali *et al.* (2019) made a study on the capability of different contact joint models to sense the effects of variations in preload and surface roughness quality. A numerical and experimental model was used to shape a joint of contact and the accuracy of the joint models was also analysed. In the numerical setup, to obtain the contact between two rough surfaces, spring elements in three different directions were used. Numerical results showed that changes in preload were captured by changes in the stiffness of the spring elements, thus being observed that only one parameter is enough to determine the dynamic behavior of the joint model. According to Jalali *et al.* (2019), the contact interfaces in the joint define the dynamic response of assembled structures. Forces and moments are transferred between components by their frictional contact interfaces. The authors affirmed that despite many studies in the past decades, the dynamic behavior of friction remains a challenge. Thereat, the authors proposed a new generic joint model to design contact interfaces in joints and examine the effect of surface roughness quality on joint model parameters.

Nikravesh and Goudarzi (2017) explored a few papers about the evaluation of the axial force of bolted structures. Knowing that bolted joints are subject to flaws, the authors target the main causes as stress concentration, crack, corrosion, and looseness. The process of looseness initiates with slipping caused by external forces, vibration, or inadequacy of axial force applied to the bolt. According to Nikravesh and Goudarzi (2017), there are two methods to measure the axial force of bolts: one can estimate the force directly and the other one calculate it directly by controlling physical parameters. In direct measurement methods, the applied torque and axial force should be monitored. Indirect measurement methods are more complex than direct ones, but they allow online monitoring and for this reason, they have received more attention in recent years. Among indirect measurement methods, the vibration-based method is a low-cost method based on monitoring variations of linear parameters but with less accuracy when compared to non-linear methods.

Initial tensile stiffness of a bolted connection was obtained by an empirical equation proposed by Zadanfarrokh and Bryan (1992), which considers the thickness of two connected sheets, a factor relating to the position of the shear plane and the load pattern of the bolt. A modification factor was included by Wang *et al.* (2021) to identify the connection flexibility of a four-layer connection and a series of numerical studies were performed to examine the rotation stiffness of the specimens. To calculate the rotation stiffness two considerations were necessary: 1) The bolt group center must coincide with the rotational center of the joint, and 2) The magnitudes of the bolt forces are proportional to the distance between the bolt holes and the rotation center. The authors found that the mod9ified proposed formula could predict the joint rotation stiffness with some limitations, e.g., bolts without pretension force, requiring some verification of the physic characteristics of the joint. Wang *et al.* (2021) made experimental and numerical work on the load-resistance performance of a joint in a steel beam-column. The work demonstrated the effectiveness of the numerical approach in assessing the stiffness

of joints between two thin plates. The authors used the experimental findings to validate the finite element analysis on a bolted cold-formed steel, achieving very similar results with both approaches. The numerical work used flat sheets modeled with Ansys elements, such as SOLID186 and spring elements represented by COMBIN39. The element COMBIN39 is set up by a spring stiffness defined by a tri-linear load-displacement relationship.

2.3 MODELING WITH UNCERTAINTY

According to (Fan *et al.*, 2020), measurement noise is inevitably found in vibration data when using vibration-based methods in SHM. Measurement noise presents a significant influence on the quality and probability of damage detection. Therefore, the method selected to monitor the structure must be capable of minimizing the noise effect during damage characterization.

Baskaran *et al.* (2021) studied the integration of multiple response signals with a probability of detection modeling in an aluminum plate with a flaw. According to the authors, for a study on PoD a great amount of data might be necessary to develop a good model. Since it is generally expensive to obtain large data experimentally, most surveys choose to rely on data-driven models. The numerical simulations used the Boundary Element Method (BEM) with a simple geometry and semi-analytical modeling. After analytically evaluating the BEM model, experimental data were used to increase accuracy. The features used in the correlation were the peak values of the impedance measured by a coil in two different frequencies. The coil scanned a very narrow linear notch over a conducting plate along the direction of the notch. The results obtained could qualitatively be extended to the study of a multiple flaw parameter.

Kim *et al.* (2021) used x-ray computed tomography as a NDT technique to investigate additive manufacturing flaws. The authors used PoD for qualifying the technique/process empirically using a two-piece phantom. The authors affirmed that PoD studies are generally empirical and this makes them relatively expensive and limited by the number of measurements. Incorporating uncertainty in the measurements, the X-ray results were integrated with experimental results using a multi-level Bayesian model. The X-ray technique considered factors that the experimental results were not capable of accessing. The authors used a non-linear relationship between the measurement signal and the true flaw volume, which was the major contribution of their work.

Qiu *et al.* (2021) made an experimental work on the tensile stress effect using thermal variation around cracks with Eddy Current Pulsed Thermography (ECPT). ECPT is a nondestructive technique that has been extensively used for crack detection, using a multi-physics-field analysis in conductive materials. Analyzing the PoD curves, the authors concluded that the stress can increase the detection of superficial cracks using ECPT. The computed PoD curves were obtained as a function of the crack depth under different stress conditions.

Gao *et al.* (2022) developed a general method for averaging and probability of detection estimation using Lamb wave crack detection in a metal plate. Lamb waves are ultrasonic-guided waves sensitive to disruption in their propagation paths and their use has been extensively

studied with damage quantification. The authors only considered the data-driven crack size quantification models, where each of the damage quantifications was treated as a discrete uncertain variable. The crack size and damage signals were processed with a hierarchical probabilistic model for Lamb wave detection formulated in a Bayesian framework. Experimental results showed that the proposed method could deliver a balance between accuracy and reliability that traditional PoD methods suffer to find.

Jorge *et al.* (2022) presented in three volumes several studies using inverse methods to monitoring damage also focusing on uncertainty modeling. In the third volume that focus in uncertainty modeling and quantification, different approaches are presented, such as experiment design, response surface methodology, Bayesian approaches, and metamodels. Over the chapters, several applications can be found in engineering. Furthermore, the book presents the challenges encountered in modeling model errors, random errors, and discretization errors, for example. In summary, the authors presented a practical overview of essential tools and concepts for modeling uncertainty in structural engineering problems.

2.4 FINAL REMARKS

The findings from Hou and Xia (2021) highlighted the necessity for efficient methods to detect and monitor damage in different structural configurations, aligning with the primary aim of this research. The utilization of the Structural Health Monitoring (SHM) techniques to identify and monitor damage in structures relates to the work of Li *et al.* (2021), who also utilized low-order fidelity models in their study to predict structural damages.

A finite element analysis was used to model a bolted joint, which was the method employed by Wang *et al.* (2021) and Xue *et al.* (2011) when assessing joint stiffness and structural behavior. Similar to the methodology employed in Hou and Xia (2021), this study will integrate a time domain analysis

This work uses a similar methodology to understand the behavior of bolted joints as made by Zadanfarrokh and Bryan (1992), Xue *et al.* (2011), Liu *et al.* (2013), and Wang *et al.* (2021) in evaluating bolted connections, and the relationship between joint stiffness and rotation stiffness. The concept of using spring elements, such as COMBIN14, to represent joints in finite element models, as used in this work, is also in line with the approaches taken by Liu *et al.* (2016), and Jalali *et al.* (2019). They employed similar elements to model contact interfaces and assess the dynamic behavior of joints.

This work introduces the concept of an R-index to evaluate damage severity based on acceleration data, similar to the approach proposed by Fernandez-Navamuel *et al.* (2022), which uses deep learning techniques for damage identification. Furthermore, as seen by Giannakeas *et al.* (2023), the use of a residual is a common choice in SHM approaches to damage identification and the residual proposed in this work is similar to the one used by the authors.

This study also analyses the effects of noise in vibration data, aligning with the issues raised by Nikravesh and Goudarzi (2017) regarding the influence of measurement noise on

damage detection using vibration-based methods.

In addition, this work considers the impact of randomness in structural parameters, a factor also explored by Zhan *et al.* (2021), who analyzed the effects of randomness on the accuracy for structural damage identification.

3 THEORETICAL CONCEPTS ON BOLTED JOINTS

According to Bickford (2007), during the assembly process, an initial tensioning force is applied to the bolt and this initial tension is extremely important due to the durability and effectiveness of the joint strongly depend on the correct initial tightening.

If the tightening goes beyond the elastic limit, the bolt cannot be reused and could also damage the joint structure. If the tightening is too loose, the tendency is to cause unwanted vibration in the structure and, consequently, increase joint loosening. Bolts with inappropriate preload are probably the most common cause of joint failure and misbehavior.

Therefore, the correct clamping force on the bolt must be assured. As the joint is tightened, most of the bolt and the joint members behave elastically, although some plastic deformation may occur in some bolt threads. In practice, both joint members and bolts operate similarly to rigid springs, one experiences compression and the other stretching. Like springs, the potential energy is stored, which enables bolts to maintain the necessary clamping force between joint members.

Bolted joints can be classified by the service forced applied: if the loads and forces are applied parallel to the bolt axes, the joint is defined as tensile or tension joint, and if the loads are perpendicular to the bolt axes, then the joint is defined as a shear joint.

A bolted joint under a axial load P can be represented as shown in Figure 3.1. The bolted joint can also be related to a springs set, where the material parts operate as different springs, where $\mathrm{K_b}$ is the bolt stiffness and $\mathrm{K_m}$ is the material stiffness.

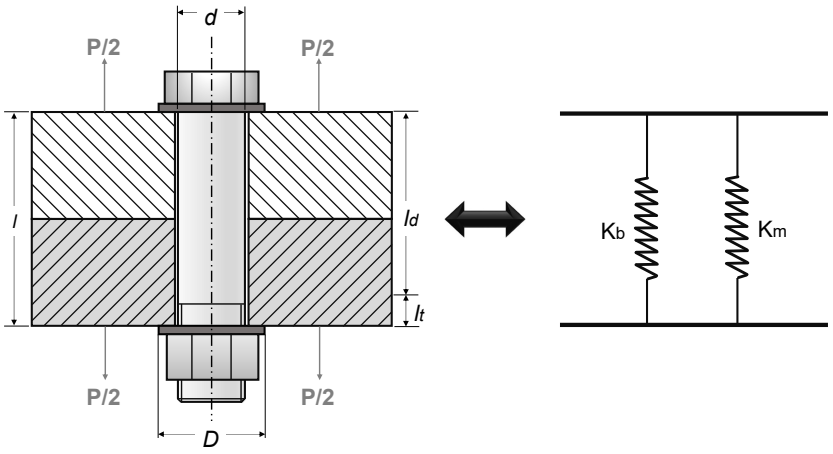

Figure 3.1. A tensile joint under the axial load P related to a parallel connection of springs. Adapted from Lourenço (2004).

As described by Inman (2014), the rules to calculate the equivalent stiffness $\mathrm{K_e}$ for parallel springs, as showed in Figure 3.1, is:

$$\mathrm{K_e} = \mathrm{K_b} + \mathrm{K_m} \tag{3.1}$$

Considering a joint with two identical plates a relation for material stiffness $\mathrm{K_m}$ is defined as a relation of the effective material area $\mathrm{A_m}$ and the material modulus of elasticity $\mathrm{E_m}$ can be found in:

$$\mathrm{K_m} = \frac{\mathrm{A_m\,E_m}}{\mathrm{l}} \ . \tag{3.2}$$

Norton *et al.* (2000) states the applied load P is divided in two components absorved by the material, $\mathrm{P_m}$, and the bolt, $\mathrm{P_b}$. Therefore, the deflection caused by the load P (Figure 3.1) on the plates and on the bolt can be assumed as being the same. Thus,

$$\mathrm{P} = \mathrm{P_b} + \mathrm{P_m} \ . \tag{3.3}$$

Furthermore, the bolt deflection is equal to the material deflection. Then:

$$\frac{\mathrm{P_b}}{\mathrm{K_b}} = \frac{\mathrm{P_m}}{\mathrm{K_m}} \ . \tag{3.4}$$

Rearranging the terms with Equation 3.3,

$$\mathrm{P_b} = \frac{\mathrm{K_b}}{\mathrm{K_m} + \mathrm{K_b}} \mathrm{P} \rightarrow \mathrm{P_b} = \mathrm{CP} \ . \tag{3.5}$$

where

$$\mathrm{C} = \frac{\mathrm{K_b}}{\mathrm{K_m} + \mathrm{K_b}} \ . \tag{3.6}$$

C is known as the stiffness constant and, in general, $\mathrm{C} < 1$. If, nonetheless, $\mathrm{K_b}$ is much smaller than $\mathrm{K_m}$, then C will be very small and, in this case, it would indicate that the bolt suffers only with a small amount of the load P.

For a circular bolt with a diameter d and subjected to an axial load over a threaded length within its clamped region of length l, the bolt stiffness $\mathrm{K_b}$ is given by (Norton *et al.*, 2000):

$$\mathrm{K_b} = \frac{\mathrm{A_t\, A_d}}{\mathrm{A_d\, l_t + A_t\, l_d}} \mathrm{E_b} \ , \tag{3.7}$$

where

$\mathrm{A_t}$ is the cross-sectional area of the threaded portion,

$\mathrm{A_d}$ is the cross-sectional area of unthreaded portion,

$\mathrm{l_t}$ is the length of the threaded portion,

$\mathrm{l_d}$ is the length of the unthreaded portion, and

$\mathrm{E_b}$ is the modulus of elasticity of the bolt.

For bolts in tension and dynamically loaded assemblies, Norton *et al.* (2000) suggests that a preload of 75% or more of proof load is typically used. The preload, $\mathrm{F_i}$, is defined as a relation of the bolt-proof strength, which is specified by SAE grade number, bolt material, and the area, $\mathrm{A_t}$. Then, the preload will be assumed as:

$$\mathrm{F_i} = 0,75\, \mathrm{S_p\, A_t} \ . \tag{3.8}$$

The preload is an important definition in bolt design. A convenient way to control the preload is through the initial torque applied to the nut. The desirable initial torque, $\mathrm{T_i}$, is proposed based on the torque coefficient, $\mathrm{K_i}$, the preload and the bolt diameter, d, as:

$$\mathrm{T_i} \cong \mathrm{K_i\, F_i\, d} \ . \tag{3.9}$$

The torque coefficient, $\mathrm{K_i}$, depends on surface hardness, lubrication, and friction coefficient. Based on Shigley (2011), $\mathrm{K_i}$ was adopted as 0.21 to find the tightening torque $\mathrm{T_i}$ in lubricated threads.

Once the bolt stiffness and preload are defined, the joint stiffness can be estimated by some approaches. Bickford (2007) presents a quick way to estimate the stiffness that can be

employed for the joint that is presented in this present work. The method expresses a joint-to-bolt stiffness relation $\mathrm{K_j}/\mathrm{K_b}$ as a function of the bolt slenderness ratio $\mathrm{L_b}/\mathrm{D}$, with $\mathrm{L_b}$ being the effective length of the bolt and D the bolt diameter. Through the experimental results presented by Bickford (2007), the relationship between joint and bolt stiffness was established as:

$$\frac{\mathrm{K_j}}{\mathrm{K_b}} \sim 3.3 \; . \tag{3.10}$$

The relationship presented in 3.10 is valid for a single bolt. Considering a set of *n* bolts, the stiffness of the set is approximated by $\mathrm{K_c}$ and:

$$\mathrm{K_c} = n\,\mathrm{K_j} \; . \tag{3.11}$$

According to Nguyen and Kim (2014), "the connection stiffness about the weak-axis of the section was assumed to be one-fifth of the stiffness about the strong-axis". Now, to calculate the rotational and flexural stiffness, the relations are proposed:

$$\mathrm{K_{rot}} = 2\,\mathrm{K_c}\,\mathrm{y}^2 \; , \tag{3.12}$$

and

$$\mathrm{K_u} = \mathrm{C_b}\,\mathrm{K_c} \; , \tag{3.13}$$

Where y is the distance between the bolt-beam center and $\mathrm{C_b}$ is, initially, adopted as 1/5. In this way, a relationship was established for the calculation of stiffness from the initial torque to be able to apply a loss of torque impacting the loss of stiffness.

The equations described above were used to find the values of torsional and flexural stiffness after defining the bolted joint. To control damage to the beam connection, torque losses ranging from 5% to 50% in 5% intervals were applied. Once the losses were applied to the torque, and the connection elements were defined through the torsional and flexural stiffnesses, then from the new torque value the stiffness values were recalculated.

The calculated values for flexural and torsional stiffness are shown in the chapter in the Table 4.1. As the flow shown in Figure 3.2, the initial step is to define the initial torque and, through the presented equations, find the rotational and flexural stiffness. This process, however, was only carried out after the initial calculation of the stiffnesses. Only then was it possible to apply damage to the initial torque. The stiffnesses were then calculated and inserted as a joint parameter in the numerical model.

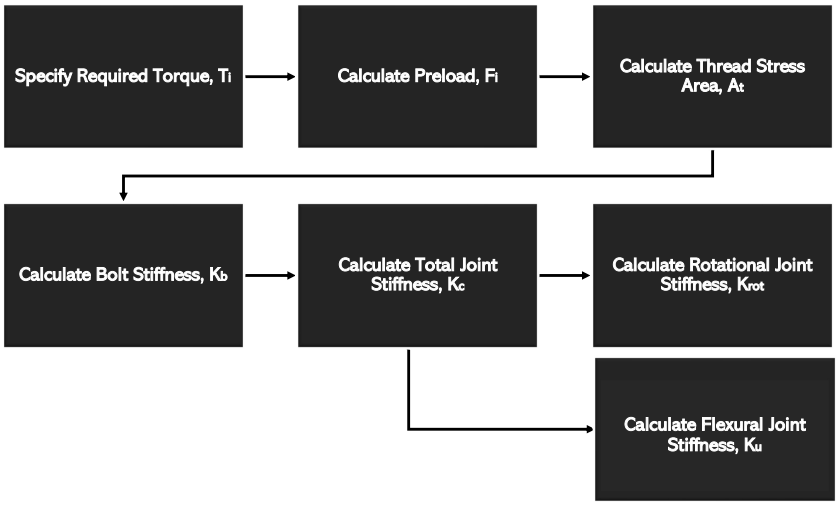

Figure 3.2. Procedure for calculating stiffness parameters when applying damage as loss of torque.

4 METHODOLOGY

In structural engineering, the analysis of complex systems using numerical methods and simulations is highlighted in understanding the dynamic behavior of structures. The steps below describe the process used in the present work where the Ansys software for finite element analysis is combined with the analytical capacity of MATLAB. In Figure 4.1 the steps are combined into a flowchart to facilitate understanding of the methodology that will be presented in the chapter.

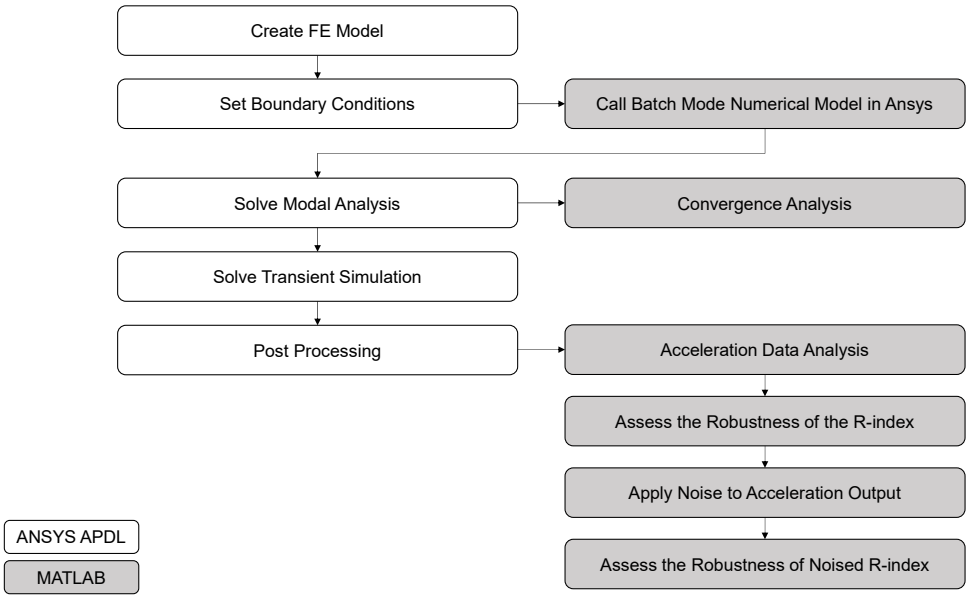

Figure 4.1. Flowchart with the steps developed in this work.

- Create FE Model:
  - In this step, a finite element model is created in Ansys software. This model will serve as the numerical representation of the analyzed structure.
- Set Boundary Conditions:
  - In Ansys, elastic boundary conditions in the finite element model are defined.
- Call Batch Mode Numerical Model in Ansys:

  - Using MATLAB, the numerical model is called in batch mode in Ansys. This allows MATLAB to interact with Ansys to perform specific analyses.

- Solve Modal Analysis:
  - Ansys performs modal analysis to calculate the natural frequencies and vibration modes of the system.

- Convergence Analysis:
  - In MATLAB, a convergence analysis is conducted. At this stage, the convergence of numerical solutions is verified about the analytical model and also in relation to a more refined model to define an acceptable refinement for the model. In convergence, the natural frequencies of the models are analyzed to define the model that meets the expected verification criteria.

- Solve Transient Simulation:
  - Once the model is defined, a transient simulation is carried out to evaluate the structure's response to dynamic loads over time.

- Post Processing:
  - Transient analysis results are processed in Ansys to extract relevant information about the dynamic behavior of the structure. In this step, acceleration information in the y direction is collected.

- Acceleration Data Analysis:
  - Using MATLAB, an analysis of the acceleration data obtained from the transient simulation is conducted. Dynamic response patterns are observed.

- Assess the Robustness of the R-index:
  - An assessment of the robustness of the R-index is performed in MATLAB. The main objective is to check how the index behaves in different conditions.

- Apply Noise to Acceleration Output:
  - Noise is applied to acceleration data in MATLAB, simulating real-world conditions where measurements may be subject to disturbance or interference.

- Assess the Robustness of Noised R-index:
  - The robustness of the R index, now with the introduction of noise into the data, is again evaluated in MATLAB. This allows you to understand how the index responds in less ideal conditions.

Numerical simulations were conducted on a computer with the following specifications:

- Operating System: Windows 11 x64;
- Processor: Intel Core i7-11390H, 11th Gen @ 3.40GHz (Base) 2.92GHz (Boost);
- RAM memory: 16 GB;
- Graphics Card: MX 450 (2 GB).

The software used for the simulations included:

- ANSYS 2019 R2;
- MATLAB R2018a.

4.1 THE JOINT DESIGN

For the joint in this work, four bolts were used to ensure a robust arrangement with two bolts at each end of the joint evenly spaced. The bolt selected was a National Aerospace Standard (NAS) fastener, the NAS6208 UNJF-3A, which is a short thread bolt hexagon-head with 20 threads. The family NAS6203 thru NAS6210 are close tolerance bolts made of alloy steel used in many aerospace applications. NAS6208 series plays an essential role in aerospace applications. They can be found in aircraft, rockets, and satellites, being fundamental for structures that demand bolts with durability and robustness. NAS6208 bolts are designed to withstand extreme conditions found in their applications, such as high-temperature fluctuations, intense vibrations, and pressure variations.

Shigley (2011) stated that the bolt has an ideal bolt length when one or two threads remain from the nut after it is tightened. The total thickness of the joint is defined with 1 aluminum plate, which is the same beam's material, and one alloy steel plate which is the same bolt material, with 15 mm each. To define the minimum bolt length, considering the two plates and a nut of 0.5 D, the bolt length must be longer than 36.35 mm.

To meet the length requirements described, the bolt NAS6208-17 was selected with its 40.386 mm length and 12.7 mm diameter, as presented in Figure 4.2. The bolt material is a 4140 alloy steel, which is employed in components subjected to high and moderate levels of stress, such as shafts, connecting rods, crankshafts, bolts, and more. At room temperature, the elasticity modulus and density are $2.1 \times 10^{11}\ \mathrm{N/m^2}$ and 7800 $\mathrm{kg/m^3}$, respectively.

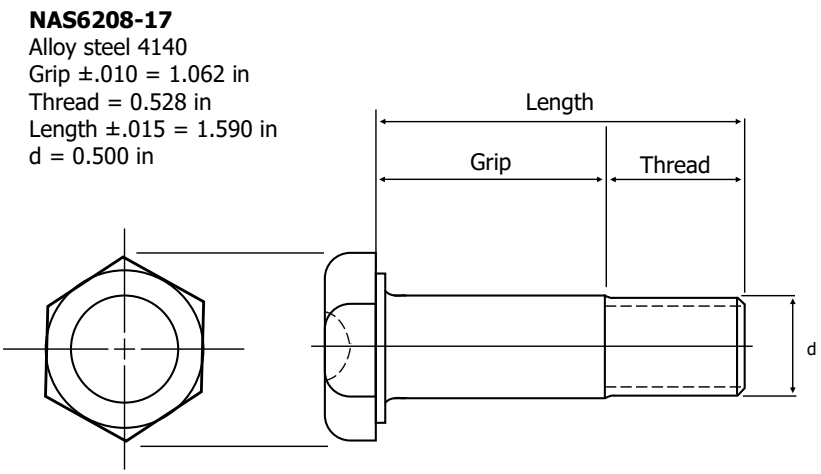

Figure 4.2. Hex head bolt NAS6208-16 of alloy steel 4140.

After bolt selection, an arrangement of the joint was proposed with four bolts arranged as shown in Figure 4.3. The bolts are evenly distributed, aligning the joint's centroid with the beam's centroid. The vertical distance is half of the horizontal distance, resulting in a rectangular joint. Figure 4.3 illustrates the cross section of the joint. In the numerical model, only the stiffness information of the problem is inserted, and the geometric characteristics of the joint are used to calculate these stiffnesses.

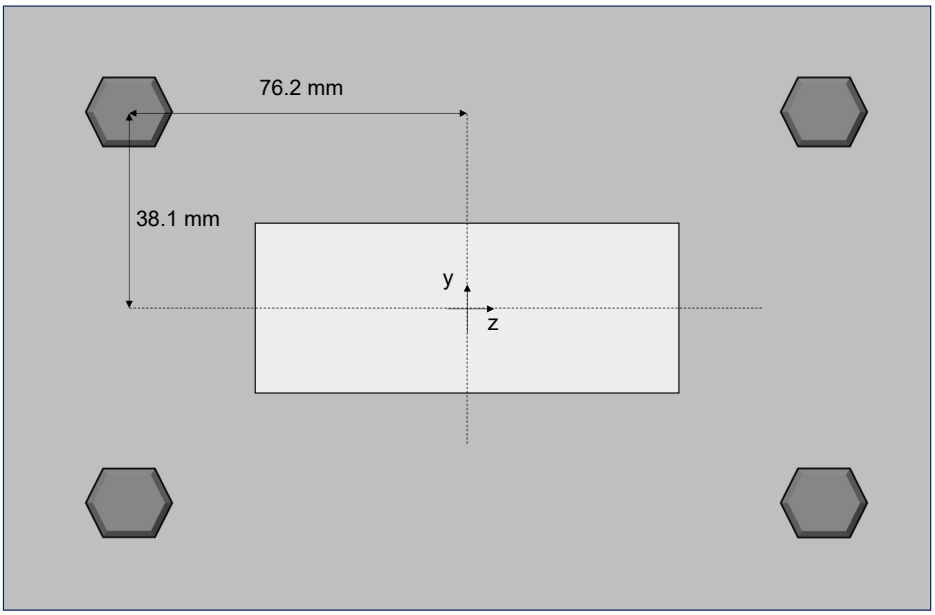

Figure 4.3. Joint schematic with four NAS6208-17 bolts.

4.2 NUMERICAL MODEL

The use of Finite Element Model (FEM) enables the subdivision of complex objects into smaller units known as elements. These elements replicate the physical characteristics of their respective portions, making this approach especially useful for detecting damage. In this work, a numerical analysis was conducted using the FEM to model a beam with elastic boundary conditions in Ansys Parametric Design Language (APDL) version 2019 R2.

APDL enables a connection among finite element concepts with practical implementation with accurate simulations. In Ansys APDL, there are two ways to build a model: using the software's toolbox or by writing command lines.

For this work, the approach of utilizing the command lines was selected to facilitate the future automation of numerical simulations that are integrated with MATLAB software. The MATLAB software was employed to automate simulation routines within APDL, allowing the systematic optimization of total simulation by managing parameter variations in the model.

The beam fixed through connectors initially simulating a cantilever beam was elaborated to create a low-order fidelity model of an airplane wing able to offer some insights about the real behavior of the problem. As mentioned by García-Macías *et al.* (2020), the geometry complexity aligned with a large number of simulations, which is generally the case in damage localization problems with FEM, has a high computational cost and causes a major limitation in practice.

Surrogate models present an attractive alternative, as their outcomes can be validated through experimental analysis or more faithful simulations of the problem. Given that, the beam was defined as a 1000 mm long beam and with a rectangular section of 40 mm wide and 10 mm thick, as presented in Figure 4.4.

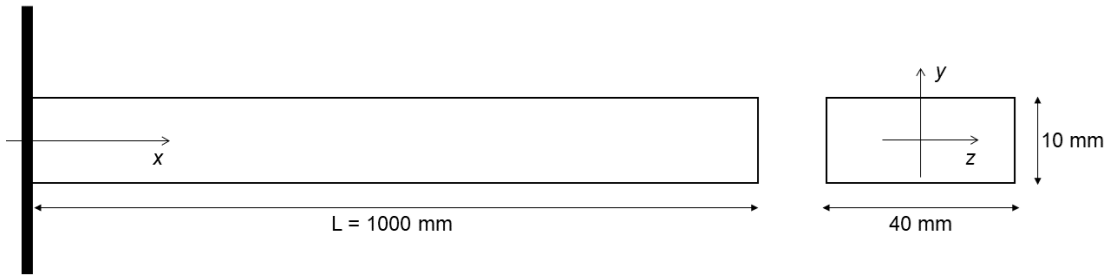

Figure 4.4. Beam setup.

The element BEAM188 was used to create the beam and the joint was represented by stiffness values which allowed a series of simulations with damage applied. In this study, BEAM188 is configured with 6 degrees of freedom at every node, including translations along the x, y, and z axes, as well as rotations about the x, y, and z axes. This element uses a 3-D linear, quadratic, or cubic two-node beam element. The element BEAM188 is based on Timoshenko beam theory, meaning that has a first-order shear deformation theory with transverse shear strain constant through the cross-section. After the deformation, the cross-section

remains plane and undistorted. According to Ansys Documentation, the element BEAM188 is a better fit for linear, large rotation, and/or large strain nonlinear applications. The beam's cross-section is characterized as a property of the beam.

In Figure 4.5, face 1 denotes -z normal direction, face 2 denotes -y normal direction, face 3 denotes +x tangential direction, face 4 denotes +x axial direction, and face 5 denotes -x axial direction. I and J denote the end nodes.

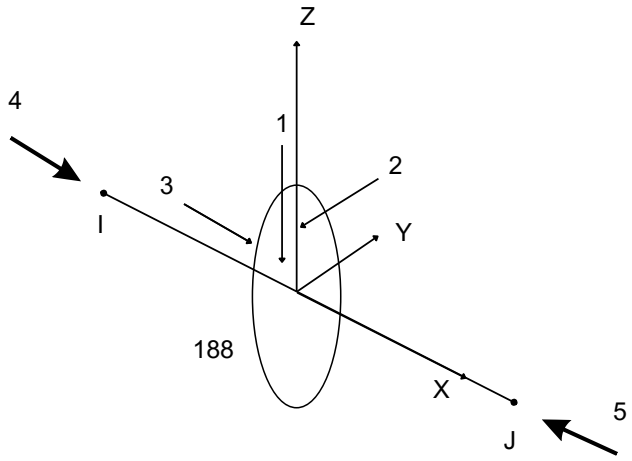

Figure 4.5. BEAM188 geometry. Source: Ansys APDL.

Damage in this case means a torque reduction which is applied to the system as a reduction in joint rigidity, that is, a detachment of the joint. As such, the Ansys element COMBIN14 was used to create a 3D spring damper contact between two nodes to define rotational, $\mathrm{K_{rot}}$, and flexural stiffness, $\mathrm{K_u}$, values for the joint. The contact condition between the beam and the spring is considered note-to-node contact. According to Ansys Documentation, the element COMBIN14 has no mass and it can be used as a longitudinal or torsional spring-damper in 1-D, 2-D, or 3-D application, as shown in Figure 4.6. $\mathrm{C_v}$ is the damping coefficient and k the stiffness.

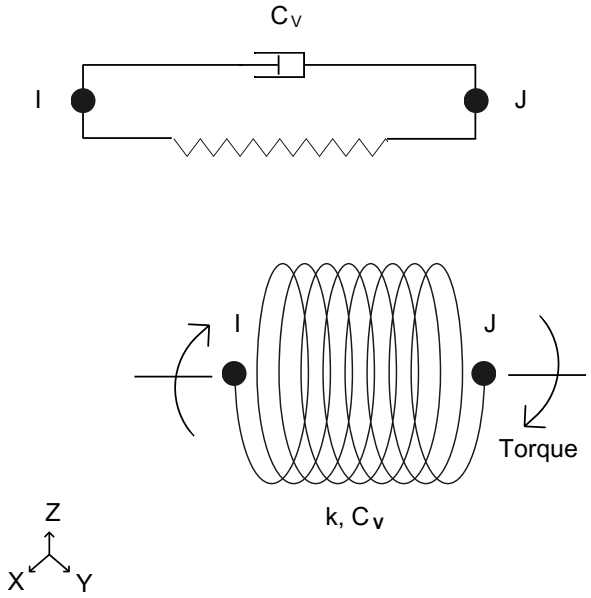

Figure 4.6. COMBIN14 geometry. Source: Ansys APDL.

Two spring elements were applied at each direction (x, y and z-axis), totaling 6 elements to simulate the joint. The rotational stiffness were named as $\mathrm{K_{rotx}}$, $\mathrm{K_{roty}}$, and $\mathrm{K_{rotz}}$ to simulate rotation in planes zy, xz, and xy, respectively. The flexural stiffness were named as $\mathrm{K_{ux}}$, $\mathrm{K_{uy}}$, and $\mathrm{K_{uz}}$ to simulate bending in planes x, y and z, respectively. Figure 4.7 represents a substantial simplification of wing-fuselage connection modeled with the APDL elements as described above.

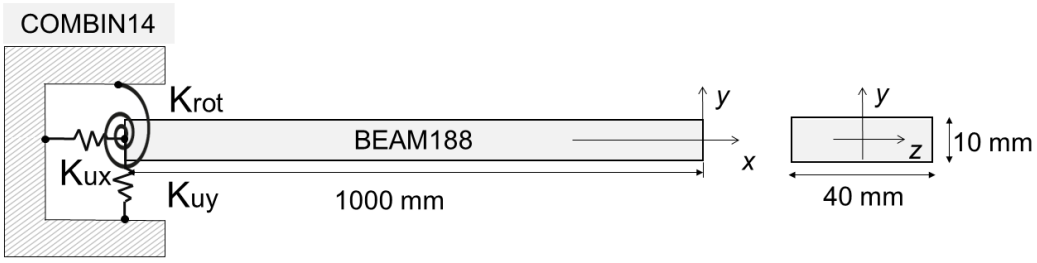

Figure 4.7. Sketch of the low-order model with COMBIN14 and BEAM188 elements.

As shown in Figure 4.8a, the beam was discretized in 20 elements, which was several elements defined through the refinement analysis process that will be described below. The

beam is represented as a two-node beam element with six degrees of freedom at each node, as mentioned above. Figure 4.8b shows the finite element model created with 20 elements in Ansys.

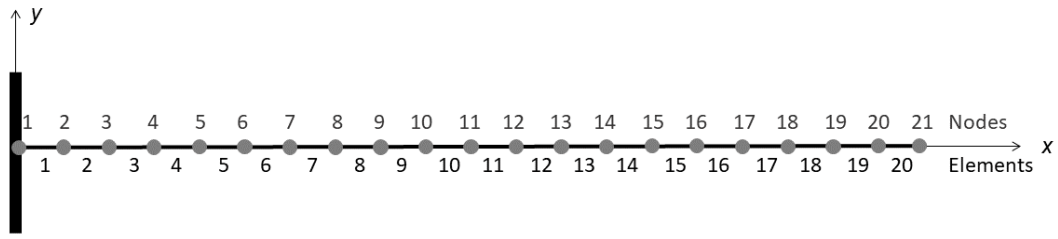

(a) Model representation with 20 elements.

(b) Ansys model with 20 elements.

Figure 4.8. Finite element model created to represent a beam with elastic connection.

After verifying the behavior of the problem without noise, modifications were made to the geometry of the problem to approximate the geometry of an aircraft wing, as was raised in the motivation of this work. Therefore, aircraft wings generally have a hollow internal structure to reduce weight without compromising strength. Therefore, the section became hollow with walls of thickness t = 3 mm. To ensure that the analysis takes into account the realistic proportions and structural characteristics associated with the wings, the length of the beam is now L = 3000 mm.

The same number of nodes was maintained so that the resolution of your simulation was maintained. This means maintaining the ability to capture fine details of the structural response without compromising computational efficiency.

Then, the new section had a rectangular hollow with a 200 mm base, 100 mm height, and t = 3 mm thick walls. The new beam length was defined as L = 3000 mm and the 21 sensors were distributed equally spaced on the new beam. Figure 4.9 presents the schematic of the new section used.

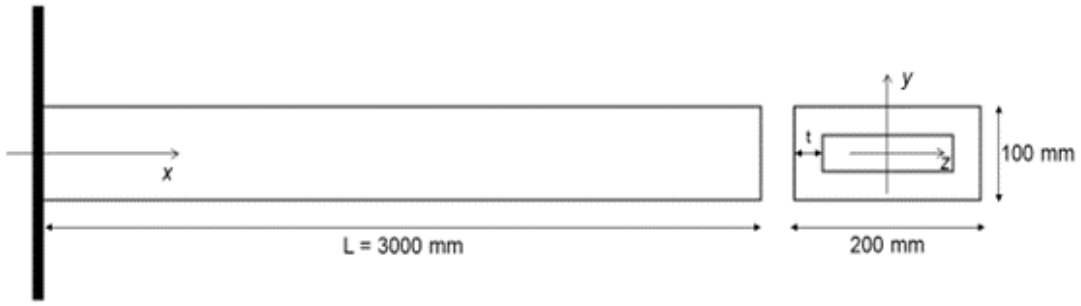

Figure 4.9. New section beam setup to assess the problem with noise in acceleration readings.

The BEAM188 is a 3D finite element that allows cross section definitions selecting the section shape and setting the shape dimensions. For the model shown in Figure 4.8b, the model is then considered as a two-dimensional representation of a 3D beam and the analysis assumes that the deformation occurs mainly along the xy plane. Even so, the section has relevant quantities such as area of integration, position, Poisson function, and others, defined through section commands. For this study, the beam was defined with an isotropic and homogeneous aluminum material with a modulus of elasticity (E) and Poisson ration (ν) defined as 2.068E11 Pa and 0.33, respectively (Callister Jr, 2007).

The great advantage of using modal analysis is that the machine time to calculate the dynamic response is greatly reduced since not all the modes are needed in the solution and still gets a satisfactory accuracy. For that reason, the superposition method was selected to obtain the dynamic response of the problem. First, a modal analysis was solved by Ansys to compute the eigenvectors and, then, the solver could combine the mode shapes to represent the deformations. The first 19 modes in xy-plane were collected to capture relevant mode shapes to this problem, as will be discussed in Section 5.1.

The choice of force is justified based on realistic modeling of the dynamic loading conditions that the structure may experience in practice. A cosine function allows the representation of a high-frequency oscillatory loading, being appropriate for the purpose of studying the behavior of the structure in the context of SHM. A force of $\mathrm{F} = 100\cos(1000\pi\mathrm{t})$ N was initially applied in the middle of the beam, at x = L/2. However, other positions of force were also analyzed, as will be discussed in Section 5.3. Sinusoidal forces are a common choice to analyze structural dynamics and vibration systems. For realistic representation, in several real-world scenarios, periodic or oscillatory forces act on structures that are of interest in the context of SHM. Also, the frequency of the applied force was defined so that it did not coincide with the natural frequencies of the system.

Simulations were carried out for 4 s using the modal superposition method. Based on the frequency of the force, time steps were defined as 1×10^{-4} s. The Nyquist frequency suggests that the time step should be less than half the lowest frequency present in the signal to avoid the phenomenon of aliasing Oppenheim *et al.* (1997). Therefore, the proposed time step is small enough to capture the dynamics of the applied force.

4.3 DAMAGE BY TORQUE REDUCTION

In this work, the damage has been described as a torque reduction, transferring a reduction in stiffness of the beam connecting elements. Thus, the damaged beam refers to the beam with loss of connection, that is, loss of torque leading to a reduction of joint stiffness.

The values used for torsional and flexural stiffness were obtained from the calculation presented in Section 3 with Equations 3.12 and 3.13, respectively. As shown in Figure 3.2, the damage applied to the beam connection was controled by a loss of torque. From the torque value, new torsional and flexural stiffness values are calculated to insert as a parameter in the connection elements in the numerical model. Table 4.1 presents the values calculated and used during this study when referring to simulations with damages applied to torque losses.

Table 4.1. Values obtained for stiffness from the loss of initial torque.

Torque Reduction	$\mathrm{T_i}$ [Nm]	$\mathrm{F_i}$ [N]	$\mathrm{A_t}$ [$\mathrm{m^2}$]	$\mathrm{K_b}$ [N/m]	$\mathrm{K_j}$ [N/m]	$\mathrm{K_c}$ [N/m]	$\mathrm{K_{rotz}}$ [Nm/rad]	$\mathrm{K_{uy}}$ [N/m]
0%	3.34×10^3	8.07×10^2	1.12×10^{-4}	3.56×10^5	8.55×10^5	3.42×10^6	1.54×10^7	5.13×10^6
5%	3.17×10^3	7.67×10^2	1.06×10^{-4}	3.53×10^5	8.48×10^5	3.39×10^6	1.53×10^7	5.09×10^6
10%	3.00×10^3	7.26×10^2	1.01×10^{-4}	3.50×10^5	8.39×10^5	3.36×10^6	1.51×10^7	5.04×10^6
15%	2.84×10^3	6.86×10^2	9.47×10^{-5}	3.46×10^5	8.30×10^5	3.32×10^6	1.49×10^7	4.98×10^6
20%	2.67×10^3	6.46×10^2	8.94×10^{-5}	3.42×10^5	8.20×10^5	3.28×10^6	1.48×10^7	4.92×10^6
25%	2.50×10^3	6.05×10^2	8.38×10^{-5}	3.37×10^5	8.09×10^5	3.24×10^6	1.46×10^7	4.86×10^6
30%	2.34×10^5	5.65×10^2	7.82×10^{-5}	3.32×10^5	7.97×10^5	3.19×10^6	1.43×10^7	4.78×10^6
35%	2.17×10^3	5.25×10^2	7.26×10^{-5}	3.26×10^5	7.83×10^5	3.13×10^6	1.41×10^7	4.70×10^6
40%	2.00×10^3	4.84×10^2	6.70×10^{-5}	3.20×10^5	7.68×10^5	3.07×10^6	1.38×10^7	4.61×10^6
45%	1.83×10^3	4.44×10^2	6.14×10^{-5}	3.13×10^5	7.51×10^5	3.00×10^6	1.35×10^7	4.50×10^6
50%	1.67×10^3	4.04×10^2	5.59×10^{-5}	3.04×10^5	7.31×10^5	2.92×10^6	1.32×10^7	4.38×10^6

Figure 4.10 illustrates the $\mathrm{K_{uy}}$ curve, while Figure 4.11 represents the $\mathrm{K_{rotz}}$ curve, both derived from the data in Table 4.1. These figures show the two gradual decreases in the $\mathrm{K_{uy}}$ and $\mathrm{K_{rotz}}$ values corresponding to torque loss. However, it is important to note that the relationship between torque loss and stiffness reduction is not linear. Consequently, a 10% torque loss does not represents a 10% decrease in stiffness.

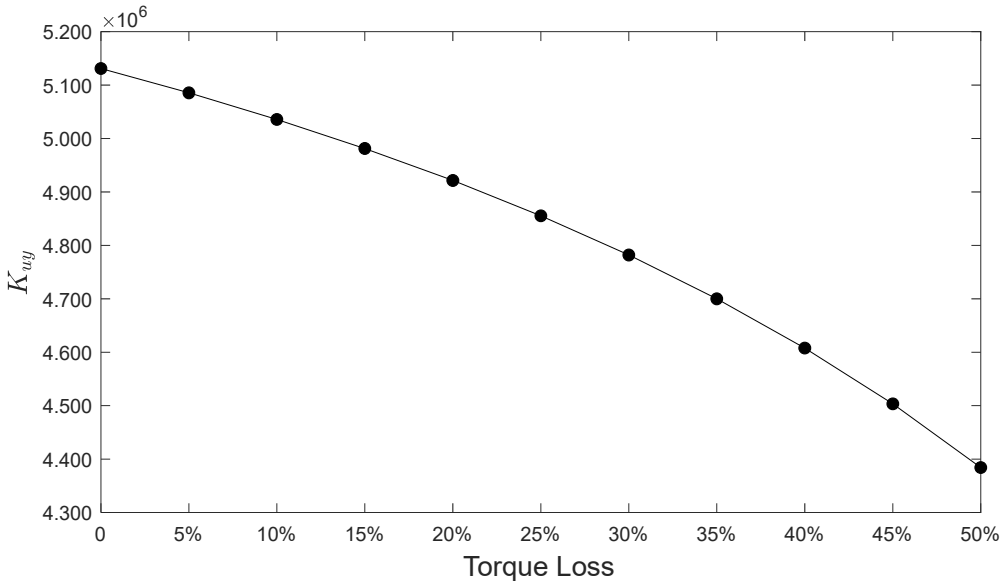

Figure 4.10. Variation of stiffness $\mathrm{K_{uy}}$ by torque reduction.

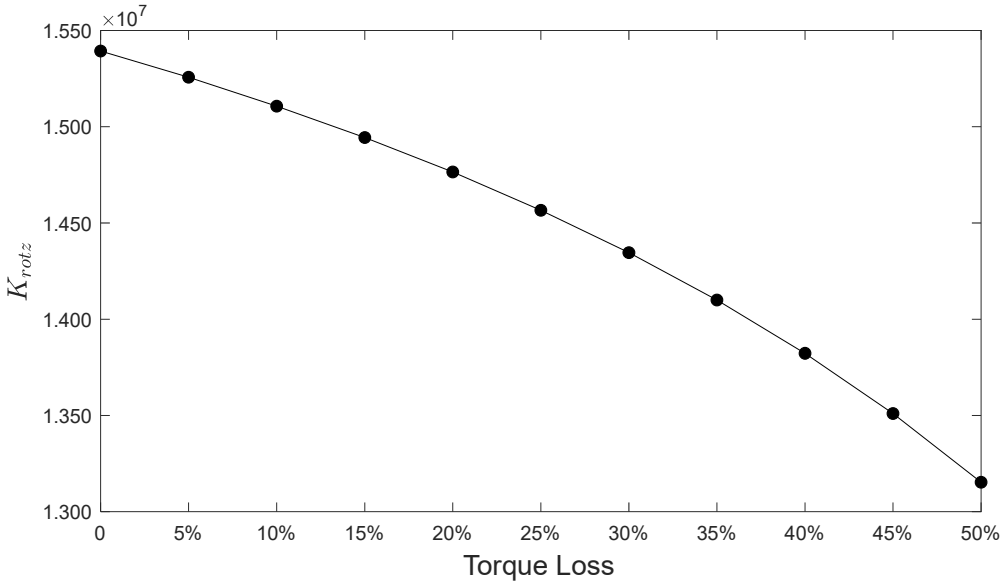

Figure 4.11. Variation of stiffness $\mathrm{K_{rotz}}$ by torque reduction.

4.4 R-INDEX

To analyze responses over time, a residual approach was introduced. Many SHM systems works by comparing the initial signal, generally damage-free, with the current signal at an unknown condition (Aliabadi and Khodaei, 2017). For the analysis, acceleration data were collected at the beam free-end to compute the residue. Standardization was introduced to ensure robust comparisons between simulated cases. Similar to Giannakeas *et al.* (2023) used, the equation reflects the normalization and quantification of the magnitude of the difference between two sets of data to a maximum reference value. The normalization of the residue is achieved by referencing the maximum damage found within the range of damage under analysis. In this way, the R-index is determined through the following equation:

$$\text{R-index} = \frac{\sqrt{\sum_{i=1}^{N_T} (H_{S_i} - D_{S_i})^2}}{D_{S_{max}}}, \tag{4.1}$$

Where H_S was the healthy signal, D_S was the damaged signal, and $D_{S_{max}}$ was the maximum damaged signal. The sum is based on the amount of damage evaluated. Thus, the R-index returns a value for each evaluated damage, where damage means a loss of torque. The evaluated damages varied between 0% and 50% in terms of tightening torque.

The R-index was evaluated for its robustness, as well as the amount and position of the beam information readings (sensors) needed. The residue contains acceleration information in the y-direction of the healthy and damaged beam tip.

4.5 ADDING GAUSSIAN WHITE NOISE TO ACCELERATION DATA

The addition of noise to the acceleration data in the vertical direction is justified to better understand the robustness and reliability of the proposed method. In practice, the collected data may contain noise and uncertainties from different sources, such sensor accuracy and calibration, environmental conditions, and material properties. Therefore, this stage of the study not only enriches the analysis but also helps ensure that the use of the R-index is robust and applicable in realistic scenarios.

A MATLAB routine was generated to introduce random noise into the acceleration data in the vertical direction, with the controlled noise intensity varying from 1% to 5%. The acceleration data were calculated based on the procedures described above, only then was the noise added to the vertical acceleration data already obtained. The data was collected at some nodes specified in the results section, where they were analyzed to obtain a better signal x noise ratio. The noise vector was created as follows:

1. **Initialize the random number generator:** Using the ”rng” command, it was seeded at the MATLAB random number generator with a seed based on the system clock. Using this command, random number generation becomes more unpredictable each time the

code is run.

2. **Create the amplitude vector:** The acceleration data from the beam's vertical direction were multiplied by a variable that controlled the noise intensity.

3. **Create the noise vector:** A noise vector was generated using the "randn" function, which creates random numbers from a Gaussian normal distribution with mean zero and standard deviation being one. The length of this noise vector is the same as the length of the acceleration data. The amplitude vector that was calculated in the previous step is multiplied by the noise vector, resulting in an amplitude-weighted noise vector.

4. **Centralize noise distribution:** The mean of the noise vector was subtracted from the noise vector to centralize the noise distribution around zero. This is done to avoid a shift in the beam data after adding noise.

5. **Adjust the noise vector:** Finally, the centered noise vector is added to the original acceleration data to obtain the noisy beam data in the vertical direction.

Summarizing the above steps into an equation, the noise vector, NV, can be described as being:

$$\mathrm{NV} = \mathrm{OAD} + \mathrm{Amp} - \mathrm{mean}(\mathrm{Amp}) \ , \tag{4.2}$$

where NV (Noise Vector) is the noisy output data in the vertical direction, OAD (Original Acceleration Data) is the original acceleration data in the vertical direction, and $\mathrm{Amp} = \frac{\mathrm{NI}}{100} \times \mathrm{OAD} \times \mathrm{randn(n)}$ is the noise amplitude weighted and centered around zero, with NI as the noise intensity and n represents the number of data points.

5 RESULTS AND DISCUSSIONS

5.1 CONVERGENCE ANALYSIS

In this section, two common methods used to achieve a fast accurate finite element solution are the p-refinements and h-refinements, are explored. P-refinement uses high-order interpolation functions, whereas the h-refinement discretizes the domain in smaller elements. The two methods formulations are based on the Euler-Lagrange equation, but when comparing both methods, the p-refinement can provide higher rates of convergence and accuracy, as affirmed by Kuo *et al.* (2006). To obtain the convergence analysis using the two mentioned methods, a modal analysis using the element BEAM188 was made.

According to Ansys documentation, the element BEAM188 can be used with linear, quadratic, or cubic shape functions to interpolate deformations within the elements. The default mode uses linear shape functions between the two end nodes, i.e. the deformations within the beam element are interpolated by a linear function using one node for integration. This option is better suitable for stiffener elements and the setup should maintain compatibility with a first-order shell element. Quadratic shape functions use the two end nodes with a third node in the middle. With two nodes for integration, a linear variation is captured along the beam. This option is suitable to represent linear varying bending moments. Alternatively, with two internal nodes, a cubic interpolation using cubic shape functions. Cubic interpolation is suitable for quadratic varying bending moments.

For the p-refinement analysis, a study considering the three interpolation options was analyzed. For the h-refinement analysis, a study was carried out considering four options: 20, 40, 80, and 160 nodes. The results of the two analyses are presented below in comparison with the highest refinement case adopted here using cubic shape functions and 160 nodes. This more refined configuration will be referred to throughout this section as *reference case*.

The results, presented in Figures 5.1-5.3, represent the evolution of natural frequencies under different refinement scenarios. Error analysis, expressed as percentage deformation (ϵ) in Equation 5.1, highlights the convergence behavior of each method. Linear, quadratic, and cubic shape functions with 20 nodes were compared, and the study identified that quadratic or cubic interpolation with 20 nodes yielded better agreement with the reference case. The chosen configuration balances computational efficiency with acceptable relative errors. The complete mode values can be seen in Appendix A. Percentage error is defined as:

$$\epsilon = \frac{|\mathrm{f} - \mathrm{f_{ref}}|}{\mathrm{f_{ref}}} \times 100 \ . \tag{5.1}$$

Figure 5.1 presents the first results of the two approaches described, where the results are introduced using linear shape functions with some modes that showed differences in the modal frequency value during the analysis. In Figure 5.1 is observed that with the increase in the number of discretizations, the observed modes tend to converge with the values obtained in the reference case. Also by using the linear shape function, it is possible to see a difference even in the lower modes. The use of the linear shape function could approximate the most refined case adopted results if used in the configuration with 160 nodes. Furthermore, in general, as the modes grew the difference concerning the reference case increased, as expected.

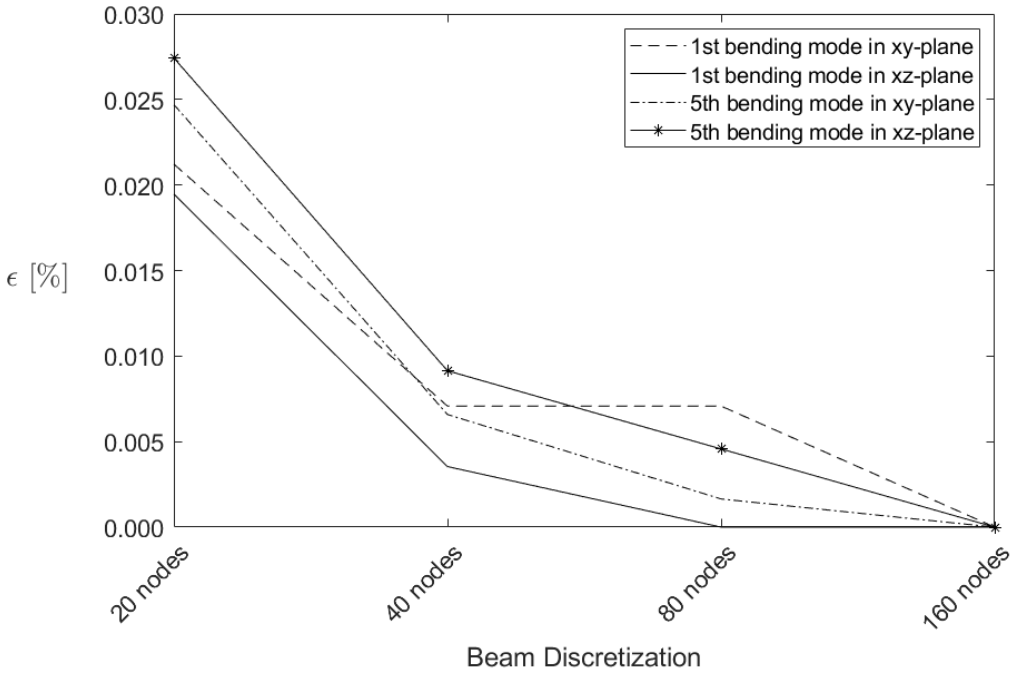

Figure 5.1. Evolution of the error in natural frequencies when using linear shape functions to interpolate.

Similarly, Figure 5.2 presents the results with a quadratic interpolation function. It is possible to see that the difference starts to appear from the 3rd bending mode in xy-plane. The first modes before, being the first and second bending modes in xy-plane and the first bending mode in xz-plane, showed agreement with the reference case even for the less refined mesh with 20 nodes. In addition, the first two torsion modes also showed a fair comparison with the reference case. Some other modes can be seen in Figure 5.2, where it is seen that, with the use of quadratic shape functions, the variation above 40 nodes was able to obtain the same frequency results as the reference case.

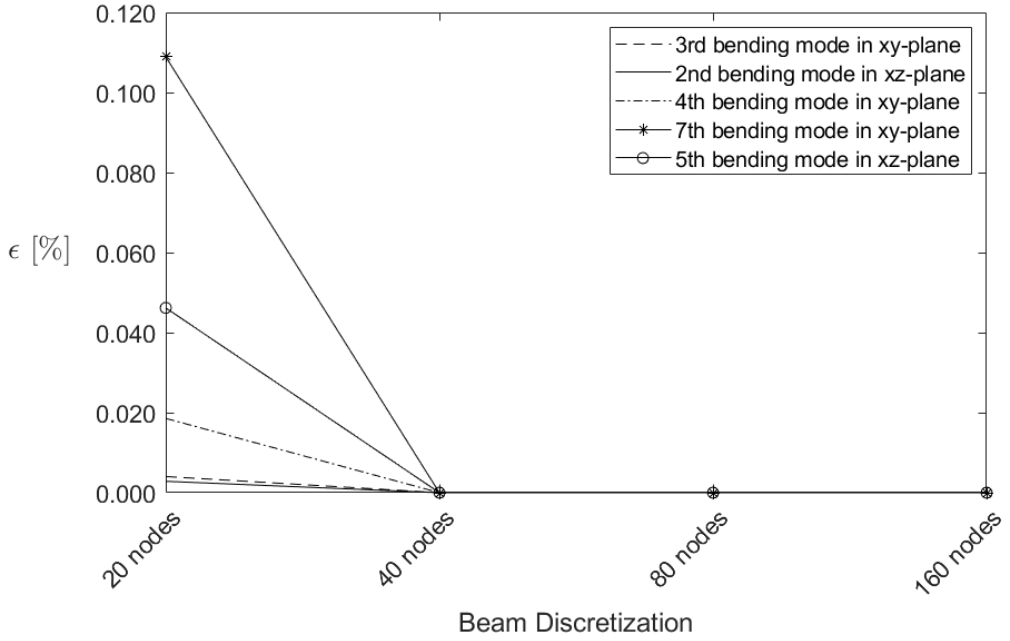

Figure 5.2. Evolution of the error in natural frequencies when using quadratic shape functions to interpolate.

The results obtained with the cubic shape functions, on the other hand, showed agreement at the lowest modes for all the numbers of nodes evaluated. The first differences started to appear outside the range of modes intended to be used in this study. However, as shown in Figure 5.3, the difference started to appear in the eighth bending mode in xy-plane but only with the less refined mesh.

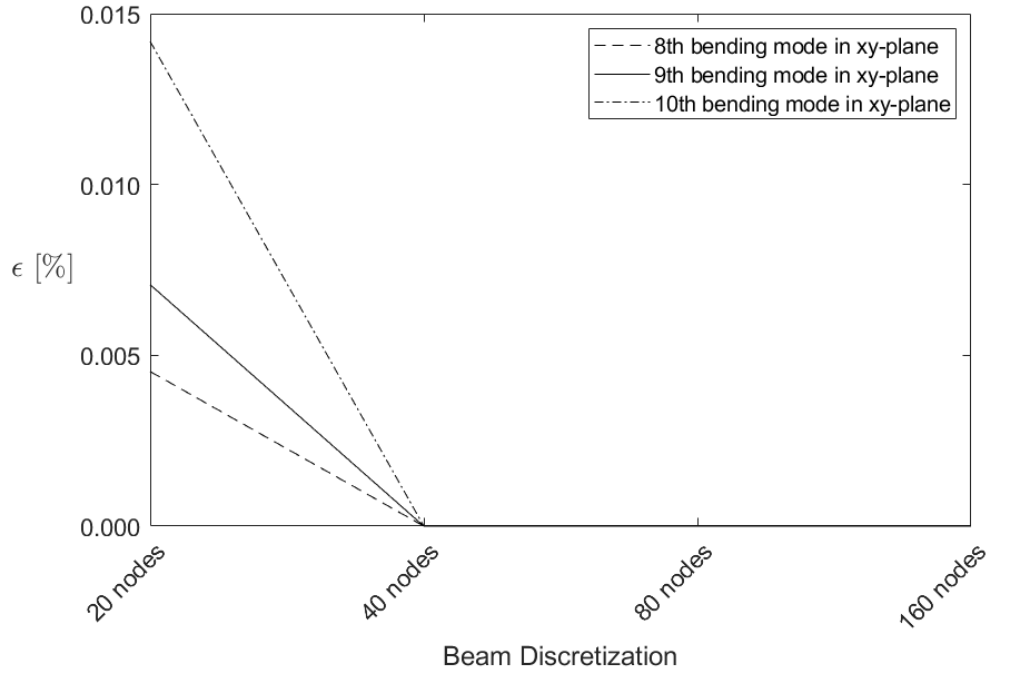

Figure 5.3. Evolution of the error in natural frequencies when using cubic shape functions to interpolate.

The main outcome was that using quadratic or cubic shape functions with the discretization of 20 nodes, the difference to the reference case fell by approximately half. In this way, the use of quadratic or cubic interpolation elements showed better agreement with the reference case than the linear interpolation. Since the objective of the work is to present a low-order fidelity modeling, it was decided to follow the studies with the configuration of 20 nodes with quadratic shape functions.

A structure with fewer elements was selected to run several analyses that needed to be done. Furthermore, a simpler model allows to save some computational costs. It is also understood that, in practice, users of the monitoring system may have a limited number of sensors due to the large increase in weight with cabling and material costs. The maximum relative error between the called reference case and the selected working model was 0.91%, however, at the lowest frequencies the error was disregarded.

Table 5.1 presents the natural frequencies and corresponding deformation descriptions resulting from the utilization of 20 elements with quadratic shape functions in a cantilever beam. The complete results can be found in Appendix A. The modes are characterized by their analytical solutions, rigid connection (ideal clamping), and elastic connection (model jointed with COMBIN14 elements, where $\mathrm{K_u} = 1 \times 10^{20}$ N/m, and $\mathrm{K_{rot}} = 1 \times 10^{20}$ Nm/rad) along with the associated percentage deformations (ϵ). The analytical solutions correspond to values computed using the equation for determining the natural frequency of a cantilevered beam, as outlined in Inman (2014).

The relative errors, ϵ, in Table 5.1 represent the relative error of the natural frenquency values obtained in the simulation of the beam with elastic connection in relation to the values obtained in the analytical solution column. These values indicate the deviation of the natural frequencies obtained in the elastic connection scenario (model jointed with COMBIN14 elements) from the analytical solutions, concerning rigid connection (ideal clamping).

Most values range from 0.00% to 5.65%, suggesting a consistent and accurate modeling of the cantilever beam with elastic boundary conditions. The higher relative errors observed in the bending mode in xz may have limited impact in this specific problem, given that the present analysis are primarily concerned with the behavior in the xy plane.

Since the focus is on modes and deformations within the xy plane, where the relative errors are generally lower, these discrepancies are not expected to significantly influence the accuracy of the results.

Then, the overall accuracy of the model can be considered satisfactory, as the majority of the relative errors are within acceptable limits for many engineering applications. In conclusion, the relative errors in the elastic connection scenario seem reasonable for finite element analysis, but further validation may be necessary, especially in cases where high precision is critical.

Table 5.1. Natural frequencies and deformation description using 20 elements with quadratic shape functions in a cantilever beam.

Mode Description	Natural Frequency [Hz]			Error
	Analytical Solution	Rigid Connection[1]	Elastic Connection[2]	ϵ [%]
1st bending mode in xy	14.14	14.14	14.14	0.00
1st bending mode in xz	56.55	56.48	56.48	0.12
2nd bending mode in xy	88.60	88.55	88.55	0.06
3rd bending mode in xy	248.08	247.76	247.76	0.13
2nd bending mode in xz	354.39	351.26	351.26	0.88
4th bending mode in xy	486.13	485.03	485.03	0.23
5th bending mode in xy	803.61	800.86	800.86	0.34
3rd bending mode in xz	992.31	971.85	971.85	2.06
6th bending mode in xy	1200.46	1194.90	1194.90	0.46
7th bending mode in xy	1676.68	1667.10	1667.10	0.57
4th bending mode in xz	1944.54	1872.80	1872.80	3.69
8th bending mode in xy	2232.26	2217.60	2217.60	0.66
9th bending mode in xy	2867.22	2847.10	2847.10	0.70
5th bending mode in xz	3214.46	3032.70	3032.70	5.65
10th bending mode in xy	3581.54	3556.70	3556.70	0.69

[1]Model jointed with ideal clamping

[2]Model jointed with COMBIN14 elements $\mathrm{K_u} = 1 \times 10^{20}$ N/m and $\mathrm{K_{rot}} = 1 \times 10^{20}$ Nm/rad

The comparative analysis of natural frequencies and modal deformations suggests that the proposed model satisfactorily meets the expected verification criteria, reinforcing confidence in its representation of the dynamic behavior of the cantilever beam, especially in the xy direction.

5.2 JOINT STIFFNESS ANALYSIS

An investigation into the behavior of the beam involved exploring extreme variations in isolated stiffness values was carried out. The primary objective was to identify the stiffness values that could allow the beam to perform as a cantilever and to understand the boundaries of the stiffness working range.

This phase of the study focused on applying incremental variations directly to individual joint stiffnesses within six COMBIN14 elements. The aim was to assess the individual behavior and influence of these variations. The natural frequencies of the system were employed for evaluating responses to stiffness alterations.

As detailed in Chapter 4, the rotational stiffness $(\mathrm{K_{rot}})$ and flexural stiffness $(\mathrm{K_u})$ were designated with subscripts x, y, and z indicating the plane of deformation. Preliminary studies on joint stiffness values were made to understand whether the variation in this stiffness would be perceived in the model. Every simulation, employing the machine configurations described in Section 4, had an average duration of 9 minutes.

To define the effects of stiffness variations around the stiffness working range, a series of modal analyses were performed considering the first 19 natural frequency modes to capture

the first 10 bending modes in the xy-plane. Understanding how natural frequencies respond to changes in rotational and flexural stiffness, $\mathrm{K_{rot}}$ and $\mathrm{K_u}$, was important to assess the behavior of the model.

Variations were applied to one stiffness while maintaining others at 1×10^{20} N/m or Nm/rad. This value was determined after confirming that natural frequencies obtained with all stiffnesses set to 1×10^{20} were identical to those without elastic connectors (as presented in Table 5.1). Results below this value indicated no change in the first natural frequencies.

The discussion in this section focuses on the results of studies in $\mathrm{K_{rotz}}$ and $\mathrm{K_{uy}}$ as these stiffness variations led to perceptible changes in natural frequencies. Findings related to other stiffnesses can be found in Appendix B. Notably, some effects observed in Tables B1-B4 align with those discussed here.

Table 5.2 presents the natural frequencies obtained with variations in rotational stiffness values around the z-axis. Notably, a shift in the position of a specific mode is observed, particularly in the 8th bending mode in the xy-plane. The 8th bending mode in xy-plane appears in different positions when changing $\mathrm{K_{rotz}}$ from 1×10^5 Nm/rad to 1×10^4 Nm/rad. This behavior is consistent across all stiffness variation studies presented in Appendix B.

In these cases, the beam assumes deformation in this plane even when the modal frequency differs from the expected one. Visual confirmation brought up a discussion of these occurrences. It is understood that the phenomenon occurs in the plane where the loss of stiffness is responsible for the deformation and that they begin to appear when the stiffness assumes values below 1×10^{10} Nm/rad. Consequently, the x-torsional mode and the longitudinal deformation mode did not suffer any change regardless of the value assumed by $\mathrm{K_{rotz}}$. Neither did any of the bending deformation modes in the xz-plane change either. This happens because this rotational stiffness is related to rotation only on the xy-plane which occurs along the z-axis.

However, the first bending mode in the xy-plane appears largely unaffected by variations in $\mathrm{K_{rotz}}$, even for a wide range of stiffness values. For higher bending modes in the xy-plane, a gradual decrease in natural frequencies is observed as $\mathrm{K_{rotz}}$ decreases. This sensitivity highlights the influence of rotational stiffness on higher-frequency deformations in the xy-plane.

Torsional modes (1st and 2nd torsional modes in x) exhibit minimal variation, reinforcing their resilience to changes in $\mathrm{K_{rotz}}$. The 1st longitudinal mode remains constant across different $\mathrm{K_{rotz}}$ values, indicating its stability and independence from variations in rotational stiffness.

The findings provide insights on limits of rotational stiffness for maintaining specific natural frequencies. This information is crucial for engineering applications where precise control over modal frequencies is essential. The results presented in this table are part of a broader study. To gain a comprehensive understanding, it is recommended to review the results for other stiffness variations (e.g., $\mathrm{K_{uy}}$) presented in subsequent sections and Appendix B.

Table 5.2. Natural frequencies obtained with $\mathrm{K_{rotz}}$ variations ($\mathrm{K_{rotx}} = \mathrm{K_{roty}} = 1 \times 10^{20}$ Nm/rad and $\mathrm{K_{ux}} = \mathrm{K_{uy}} = \mathrm{K_{uz}} = 1 \times 10^{20}$ N/m).

Mode Description	Natural Frequency [Hz]							
	$\mathrm{K_{rotz}}$ 1×10^{20} Nm/rad	$\mathrm{K_{rotz}}$ 1×10^{10} Nm/rad	$\mathrm{K_{rotz}}$ 1×10^{5} Nm/rad	$\mathrm{K_{rotz}}$ 1×10^{4} Nm/rad	$\mathrm{K_{rotz}}$ 1×10^{3} Nm/rad	$\mathrm{K_{rotz}}$ 1×10^{2} Nm/rad	$\mathrm{K_{rotz}}$ 1×10^{1} Nm/rad	$\mathrm{K_{rotz}}$ 1 Nm/rad
1st bending mode in xy	14.14	14.14	13.95	12.51	7.23	2.61	0.84	0.27
1st bending mode in xz	56.48	56.48	56.48	56.48	56.48	56.48	56.48	56.48
2nd bending mode in xy	88.55	88.55	87.38	80.09	66.58	62.52	62.03	61.98
3rd bending mode in xy	247.76	247.76	244.56	227.48	205.98	201.31	200.80	200.74
2nd bending mode in xz	351.26	351.26	351.26	351.26	351.26	351.26	351.26	351.26
4th bending mode in xy	485.03	485.03	478.91	450.59	423.87	419.05	418.53	418.48
1st torsional mode in x	607.33	607.33	607.33	607.33	607.33	607.33	607.33	607.33
5th bending mode in xy	800.86	800.86	791.00	750.86	720.38	715.47	714.95	714.90
3rd bending mode in xz	971.85	971.85	971.85	971.85	971.85	971.85	971.85	971.85
6th bending mode in xy	1194.90	1194.90	1180.60	1128.50	1095.20	1090.30	1089.80	1089.70
7th bending mode in xy	1667.10	1667.10	1647.50	1583.70	1548.30	1543.40	1542.80	1542.80
2nd torsional mode in x	1822.00	1822.00	1822.00	1822.00	1822.00	1822.00	1822.00	1822.00
4th bending mode in xz	1872.80	1872.80	1872.80	1872.80	1872.80	1872.80	1872.80	1872.80
1st longitudinal mode	2187.90	2187.90	2187.90	2187.90	2187.90	2187.90	2187.90	2187.90
8th bending mode in xy	2217.60	2217.60	2192.10	2116.90	2079.80	2074.80	2074.30	2074.20
9th bending mode in xy	2847.10	2847.10	2815.10	2728.70	2690.20	2685.20	2684.70	2684.60
5th bending mode in xz	3032.70	3032.70	3032.70	3032.70	3032.70	3032.70	3032.70	3032.70
3rd torsional mode in x	3036.70	3036.70	3036.70	3036.70	3036.70	3036.70	3036.70	3036.70
10th bending mode in xy	3556.70	3556.70	3517.60	3420.30	3380.60	3375.50	3375.00	3375.00

Next, the changes in flexural stiffness in the y-axis, $\mathrm{K_{uy}}$, are presented in Table 5.3. Analogously, no variations were observed in the bending modes in the xz-plane, in the longitudinal deformation mode in the x-axis, and the torsion modes around the x-plane. That is, only the xy bending modes were affected by variations in $\mathrm{K_{uy}}$. Indeed, it was expected since the modes that were collected and of interest in this work should not be affected by the connection loss, i.e. stiffness loss, in this direction.

Another relevant point was that, in general, when the stiffness assumes lower values, ~ 1, the beam tends to deform as if it was not connected. In some cases under these conditions, the body deflected as a rigid body around its connection due to the other degrees of freedom were high stiffness values. For example, this was seen happening with $\mathrm{K_{uy}}$ when the flexural stiffness in the y-axis was $\mathrm{K_{uy}} = 1$ N/m, as can be seen in Figure 5.4a.

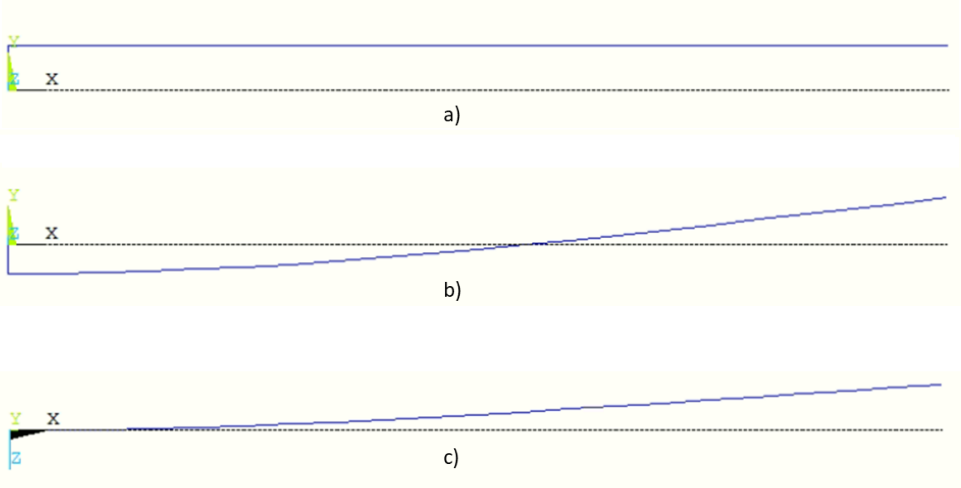

Figure 5.4. First deformation modes obtained with $\mathrm{K_{uy}}$ =1 ($\mathrm{K_{rotx}} = \mathrm{K_{roty}} = \mathrm{K_{rotz}} = 1 \times 10^{20}$ Nm/rad and $\mathrm{K_{ux}} = \mathrm{K_{uz}} = 1 \times 10^{20}$ N/m): a) first and b) second rigid body deflections, and c) first bending mode in xz-plane.

It was observed that, despite the changes in the positions of the modes, collecting the information on the first 19 modes was enough to obtain the first 10 bending modes in the xy-plane. The interest in capturing the bending modes in the xy-plane is due to the beam being bent in the y direction.

Moreover, it was observed that these variations, in general, occur below the value order that will be used in the problem. Thus, it was understood that the observed anomalies should not cause changes in the following readings. The objective of this analysis was to make an initial study of how the frequencies and the model would behave with stiffness losses to evaluate the numerical modeling.

Table 5.3. First natural frequencies obtained with $\mathrm{K_{uy}}$ variations ($\mathrm{K_{rotx}} = \mathrm{K_{roty}} = \mathrm{K_{rotz}} = 1 \times 10^{20}$ N/m and $\mathrm{K_{ux}} = \mathrm{K_{uz}} = 1 \times 10^{20}$ N/m).

Mode Description	Natural Frequency [Hz]							
	$\mathrm{K_{uy}}$ 1×10^{20} N/m	$\mathrm{K_{uy}}$ 1×10^{10} N/m	$\mathrm{K_{uy}}$ 1×10^{5} N/m	$\mathrm{K_{uy}}$ 1×10^{4} N/m	$\mathrm{K_{uy}}$ 1×10^{3} N/m	$\mathrm{K_{uy}}$ 1×10^{2} N/m	$\mathrm{K_{uy}}$ 1×10^{1} N/m	$\mathrm{K_{uy}}$ 1 N/m
1st bending mode in xy	14.14	14.14	13.77	10.99	4.67	1.53	0.48	0.15
1st bending mode in xz	56.48	56.48	56.48	56.48	56.48	56.48	56.48	56.48
2nd bending mode in xy	88.55	88.55	64.18	30.70	23.28	22.57	22.57	22.49
3rd bending mode in xy	247.76	247.76	143.56	123.47	121.67	121.49	121.48	121.47
2nd bending mode in xz	351.26	351.26	351.26	351.26	351.26	351.26	351.26	351.26
4th bending mode in xy	485.03	485.02	308.18	300.54	299.83	299.76	299.75	299.75
1st torsional mode in x	607.33	607.33	607.33	607.33	607.33	607.33	607.33	607.33
5th bending mode in xy	800.86	800.84	561.23	557.29	556.91	556.87	556.87	556.87
3rd bending mode in xz	971.85	971.85	971.85	971.85	971.85	971.85	971.85	971.85
6th bending mode in xy	1194.90	1194.90	895.20	892.78	892.55	892.52	892.52	892.52
7th bending mode in xy	1667.10	1667.00	1308.30	1306.70	1306.50	1306.50	1306.50	1306.50
2nd torsional mode in x	1822.00	1822.00	1822.00	1822.00	1822.00	1822.00	1822.00	1822.00
4th bending mode in xz	1872.80	1872.80	1872.80	1872.80	1872.80	1872.80	1872.80	1872.80
1st longitudinal mode	2187.90	2187.90	2187.90	2187.90	2187.90	2187.90	2187.90	2187.90
8th bending mode in xy	2217.60	2217.40	1800.00	1798.80	1798.70	1798.70	1798.70	1798.70
9th bending mode in xy	2847.10	2846.80	2370.50	2369.60	2369.50	2369.50	2369.50	2369.50
5th bending mode in xz	3032.70	3032.70	3032.70	3032.70	3032.70	3032.70	3032.70	3032.70
3rd torsional mode in x	3036.70	3036.70	3036.70	3036.70	3036.70	3036.70	3036.70	3036.70
10th bending mode in xy	3556.70	3556.30	3020.50	3019.80	3019.70	3019.70	3019.70	3019.70

5.3 RESIDUE ANALYSIS ON NUMBER AND POSITIONING OF DATA READINGS

In this section, the development of the analyzes of the quantity and position of the data readings will be presented. The data reading was performed at the nodes along the beam and the distribution of the number of readings was uniform, that is, equally spaced.

The objective of the study presented in this section was to simulate a real-world situation where information would be collected through sensors evenly distributed along the beam. Therefore, the value used for the stiffness was $\mathrm{K_u} = 1 \times 10^{10}$ N/m and $\mathrm{K_{rot}} = 1 \times 10^{10}$ Nm/rad to simulate a perfect connection. The R-index was studied to assess its robustness in the face of limitations with variations in the number of sensors and position.

During the analysis, the data readings were equally distributed along the beam at nodes, as seen in Figure 5.5. The distribution was made by always dividing the beam into equal parts, to facilitate the positioning of the sensors in real situations. Figure 5.5a describes the data readings with 21 sensors, Figure 5.5b describes the data readings with 11 sensors along the beam, Figure 5.5c represents 5 sensors along the beam, and Figure 5.5d represents the beam only with 3 sensors equally spaced.

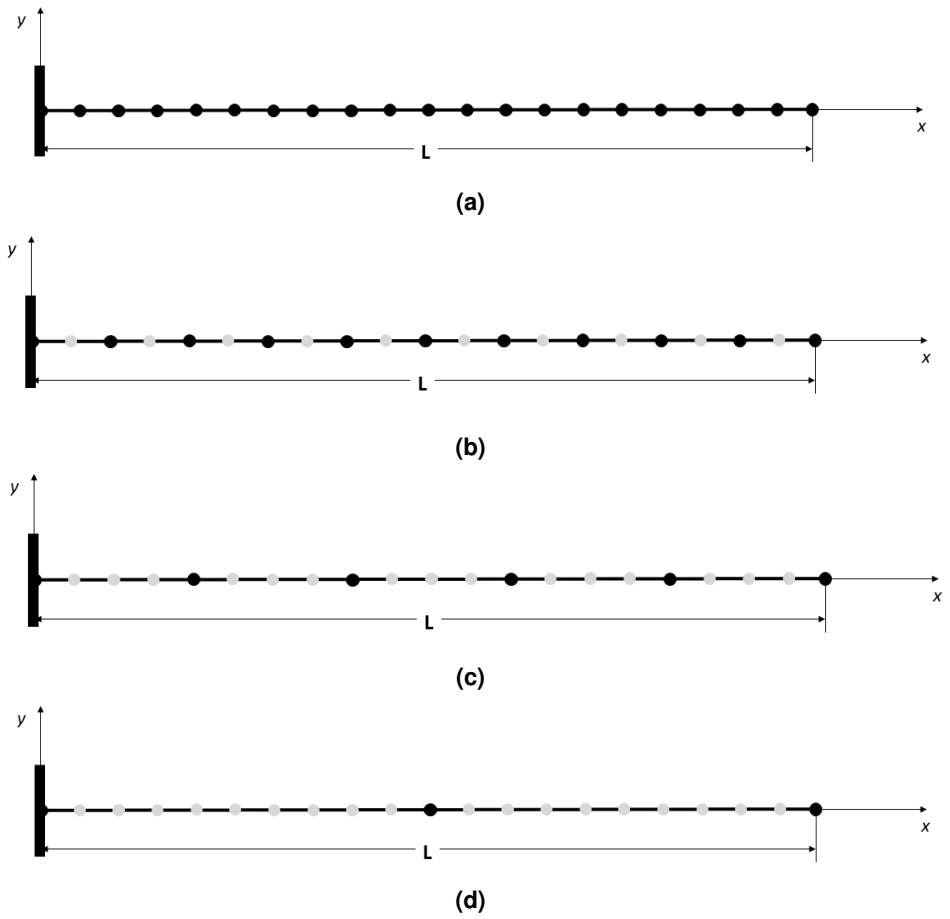

Figure 5.5. Data reading (sensors) topology with a) 21 sensors, b) 11 sensors, c) 5 sensors and d) 3 sensors.

It was observed in Section 5.2 that, for small variations in stiffness, the modes practically

did not change. For this reason, it was decided to rate variations over time through acceleration information in the y direction. Transient simulations were performed using modal superposition taking the first ten bending modes in xy-plane. The damage applied varied between 5% and 50% on the initial torque. For this analysis, a vertical force of $\mathrm{F(t)} = 100\cos(1000\pi \mathrm{t})$ N was applied at different positions, and the residue R was calculated about the healthy beam, as presented in Equation 4.1.

The position of force application was also varied to evaluate whether R was influenced by fluctuations caused, for example, by gusts of wind on an airplane wing. The applied force variations were made with spacings of L/5. Figure 5.6 presents the different schemes of the position of the force application. Figure 5.6a shows the force applied at x = L/5, Figure 5.6b shows the force applied at x = 2L/5, Figure 5.6c presents the force applied at x = 3L/5, Figure 5.6d describes the force applied at x = 4L/5 and Figure 5.6e shows the beam when the force was applied at x = L.

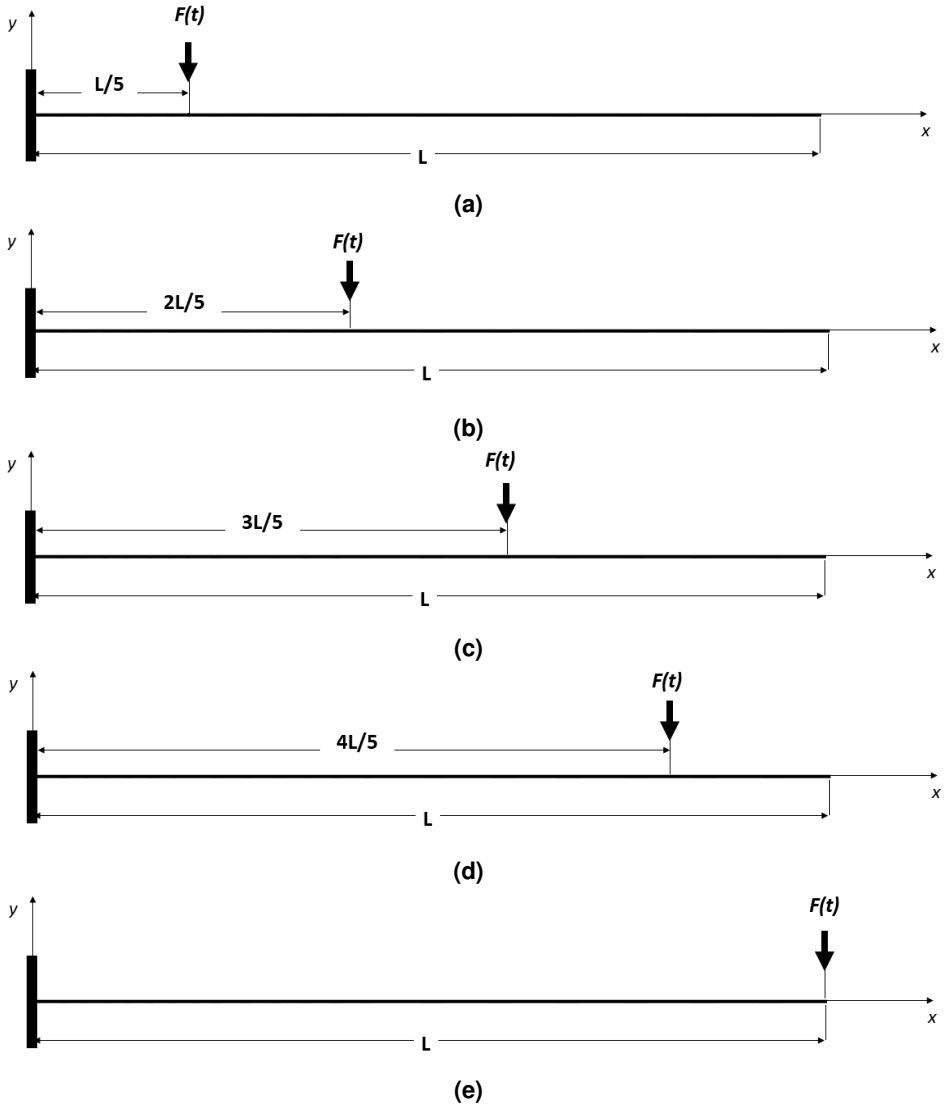

Figure 5.6. Application of force at nodes at a) x = L/5, b) x = 2L/5, c) x = 3L/5, d) x = 4L/5 and x = L/5.

In total, 4 configurations of sensor distribution combined with 5 configurations of force application were merged into 20 different combinations to this analysis. From the results of this analysis, the normalized R-index also showed that only the loss of torque related to $\mathrm{K_{uy}}$ and $\mathrm{K_{rotz}}$ stiffnesses presented variations, as seen in Section 5.2. Thus, the presented results were calculated based only on torque losses related to $\mathrm{K_{uy}} - \mathrm{K_{rotz}}$ pair.

Figure 5.7 and Figure 5.8 show the accelerations obtained at the end of the beam with the force applied at x = L. The acceleration data was normalized by the respective maximums observed in the signal. Figure 5.7a and Figure 5.7b show the signal of the healthy beam and the beam with 35% loss of torque, respectively, between the interval of 1.05 s and 1.10 s. It was possible to observe that despite the presence of damage, the acceleration signal from a damaged beam in Figure 5.7b was quite similar to the healthy beam in Figure 5.7a. However, there is a small discrepancy between the two signals captured by the R-index, as will be shown.

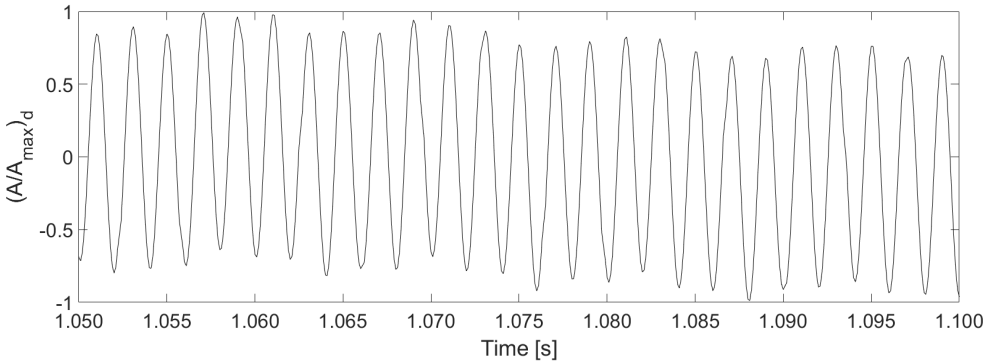

(a)

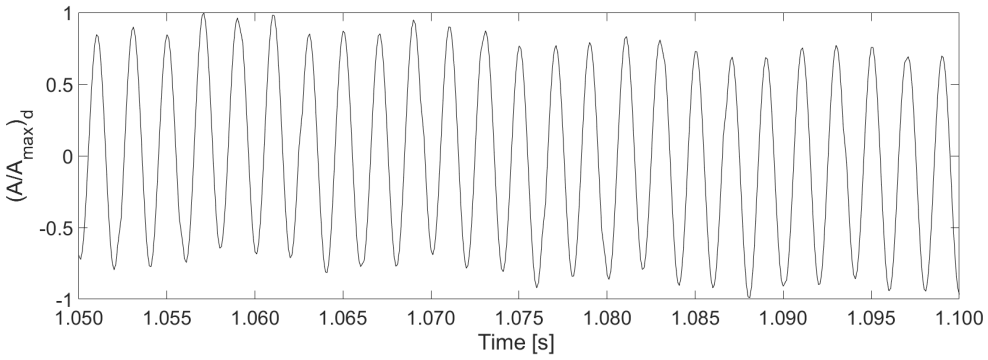

(b)

Figure 5.7. Acceleration signal collected during 0.05 s at the beam tip for a) the healthy beam, h, normalized by the highest acceleration value of the healthy beam signal and b) the damaged beam, d, normalized by the largest acceleration value of the beam signal with 35% loss of torque.

In Figure 5.8a, the difference between the two signals (healthy and damaged) was normalized by the maximum acceleration of the healthy beam in the first 0.05 s. The signals of the healthy and damaged beam are shown in Figure 5.7. As mentioned, although small, the discrepancies could be measured. In the first seconds, in the transition phase of the model, the normalized differences were of the order of 1×10^{-3}, as shown in Figure 5.8a. In another

moment, after the model reached its stability, the normalized variations occurred between $\pm$ 1×10^{-2}, as can be seen in Figure 5.8b. Figure 5.8b shows the same signal calculated for Figure 5.8a only for the interval 1.05 s and 1.10 s.

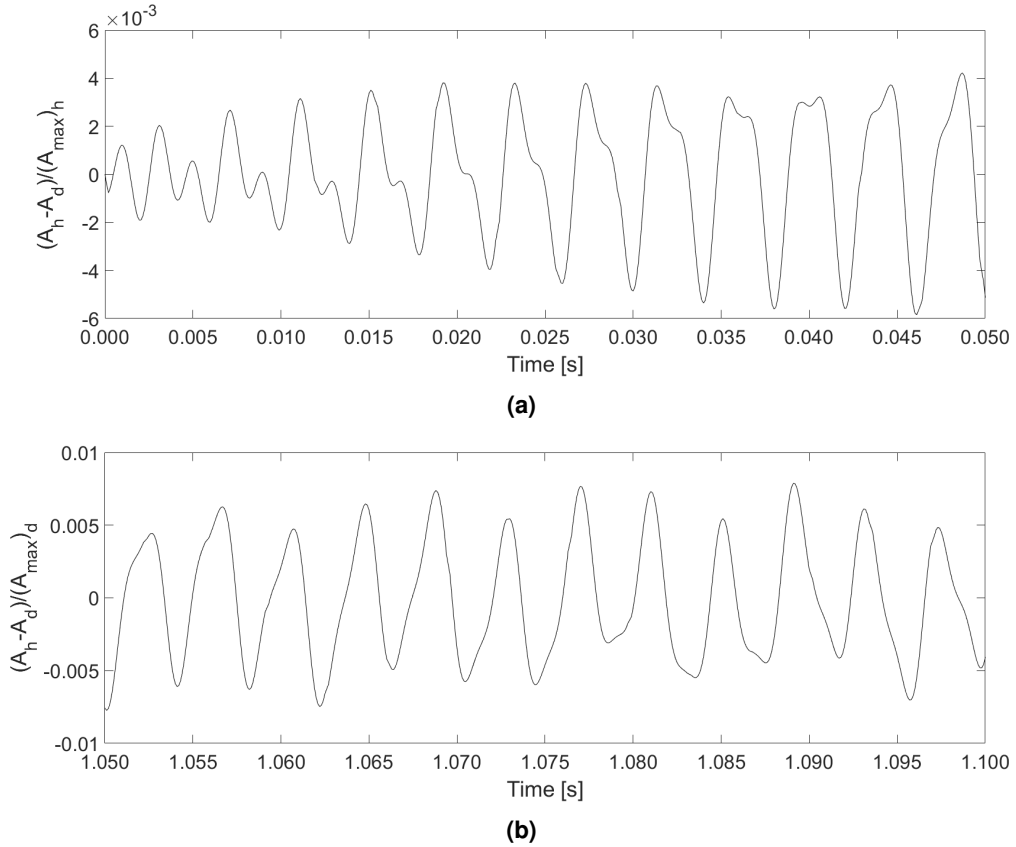

Figure 5.8. Difference between acceleration signals of healthy beam, h, and damaged beam, d, normalized by maximum acceleration of healthy beam in the interval of a) 0 s to 0.05 s, and b) 1.05 s to 1.10 s.

From this discrepancy captured between the signs of the healthy and damaged beam, it was possible to calculate the R-index and compare the results based on the level of torque loss. During the process of comparing the results, a unique pattern was observed at curves R-index $\times$ Torque Loss. Furthermore, the normalized results showed that the number and position of the sensors did not have a noticeable influence on the R-index. For this reason, the following results will be presented as a discussion of the results that are completely presented in Appendix C. In Figure 5.9 the results of analysis on the number and positioning of data readings were summarized and presented grouped by force application position. The average presented was made with the results of all 21 sensors since the amount and position of data readings seemed to be irrelevant to the R-index. In Figure 5.9a, the residue is shown before normalization, that is, only the numerator was calculated and presented. Even without normalization, it is already possible to identify a similar behavior between the analyzed cases as the loss of torque was increased.

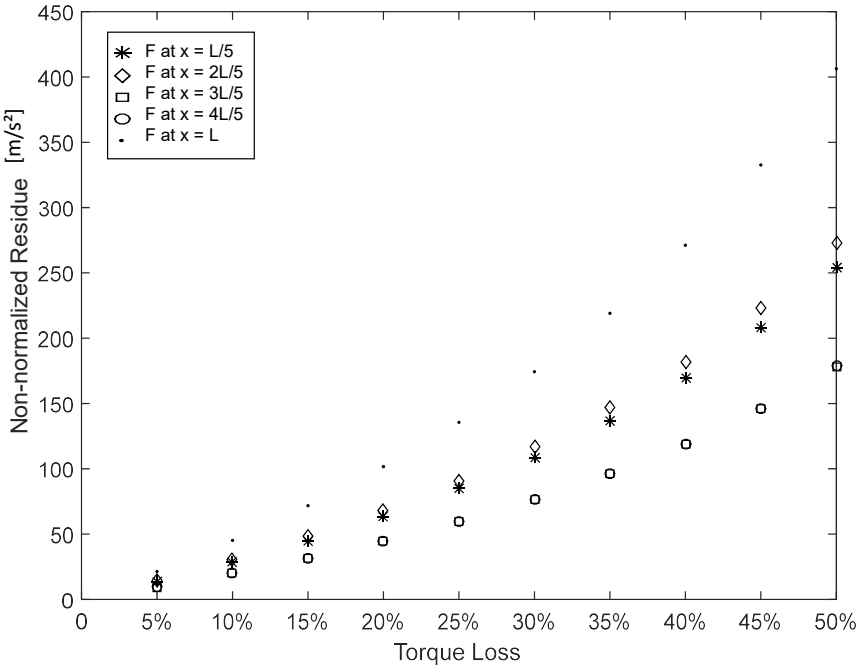

(a)

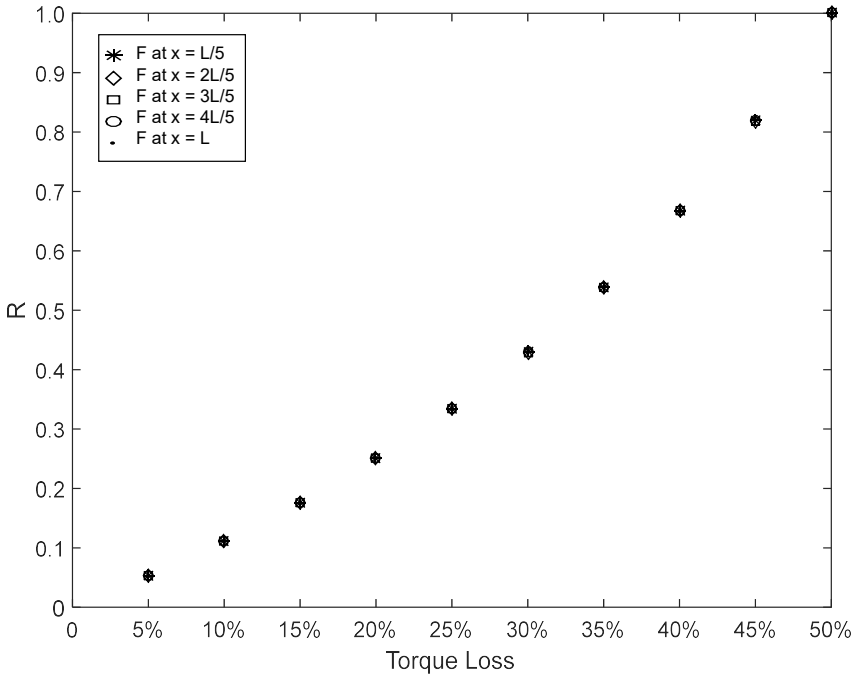

(b)

Figure 5.9. Residual obtained with the average of results of 21 sensors with different position of application of force: a) Non-normalized residue and b) R-index.

The results obtained with the force at x = 3L/5 and x = 4L/5 were very close, unlike the others that could be distinguished when presented in the same graph. Figure 5.9b presents the same separation by the position of force application but with the results normalized ac-

cording to what is presented in the residue Equation 4.1. It was noted that by normalizing the results, it would be possible to observe the same behavior where all results would fall on an approximately quadratic curve and this could be used to solve the inverse problem.

Normalization on the R-index uses the highest value among the damages, which normally should correspond to the sign of the 50% torque loss. From the curves in Figure 5.9a it was also noticed that the curve with greater damage occurred when the force was applied at x = L, as it should be.

After taking the average of the R-index between the 21 nodes and grouping by the position of force application presented in Figure 5.9b, now the average between the position of force application. Thus, an average on the full study with torque losses related to $\mathrm{K_{uy}} - \mathrm{K_{rotz}}$ pair (Appendix C) was calculated and a single mean could be extracted as shown in Figure 5.10. In this curve, each node represents the average of the R-index obtained with the 20 variations for each toque loss.

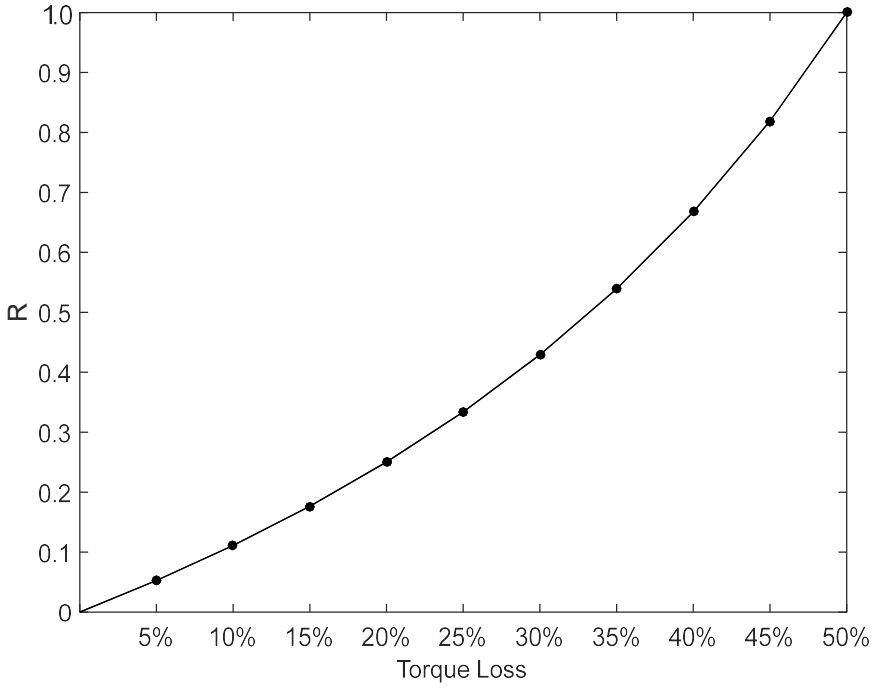

Figure 5.10. Average curve of the average R-index values related to $\mathrm{K_{uy}} - \mathrm{K_{rotz}}$ obtained during analysis of number of data readings (sensors) and position.

As seen in Figure 5.10, the pattern could be approximated by a quadratic curve allowing the curve to be reversible in a practical way. Even if the curve were more complex than a quadratic or cubic one, it would still be easier to invert this problem rather than running a finite element problem through its entirety or solving the inverse problem using a genetic algorithm, for example.

With this, it was seen that the R-index proved to be robust to changes in the modeling of the problem. The position and number of sensors, as well as the position of force application,

did not seem to affect the ability to provide information on torque loss. This result should be reassessed with the application of noise on top of the collected accelerations. In addition to validating the conclusions about the proposed residue, by doing so the model would approach a collection in sensors where there are intrinsic measurement errors.

From the average values, a quadratic fitting curve was generated, as shown in Figure 5.11. With this, the R-index could be predicted through the curve:

$$\mathrm{R} = 2.4949\mathrm{T}^2 + 0.7112\mathrm{T}\ ,\ , \tag{5.2}$$

where T would be the torque loss. The coefficient of determination of the quadratic fitting curve was 0.9821, which represents the variation of the fitting values to average values shown in Figure 5.10. In Figure 5.11, both the average and fitting curves are presented where it is possible to observe that some values may be outside the fitting curve since the coefficient of determination is different from 1. Despite that, from the fitting curve, it already would be possible to provide a solution to the inverse problem.

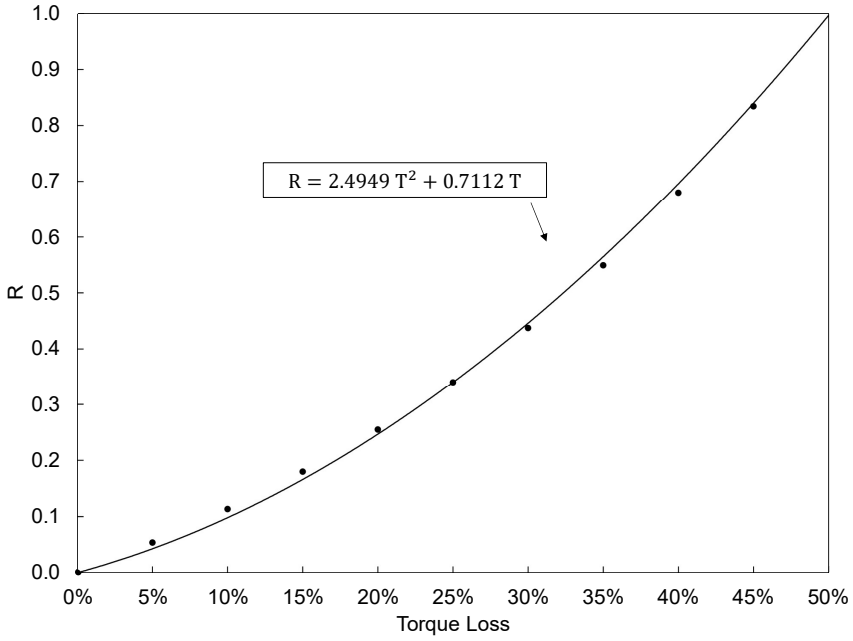

Figure 5.11. Quadratic fitting curve was obtained to approximate the results of the 20 combinations of force application position variation, sensor quantity, and sensor position.

Therefore, from the results of this study, it was possible to infer that the residue provided similar results regardless of the distribution of nodes with data readings, or sensors, and the position of application of the sinusoidal force. When talking about sensor topology, the hierarchical levels are quantity, location, and type of sensor that captures different information. Sometimes, when performing topological optimization for sensor position to maximize detection probability, it is possible to work out the number of sensors and their location to minimize

the error of capturing noise. Fewer sensors on the beam, less expensive the project, and less processing is required. On the other hand, a small amount of sensors could lead to errors if any sensor fails and the set is insufficient to provide the necessary information for the correct prediction of the damage.

Also, when the normalized residue R was compared due to loss of torque, a quadratic curve was obtained for damage variations. This behavior was only identified after normalization by the maximum damage signal for each damage case. Observing the fitting curve proposed in all graphs presented in Appendix C is possible to note that the curve was able to represent the average growth curve of the residues as a function of the loss of torque.

5.4 CONFIDENCE BOUNDS

Throughout the development of this work, a low-order finite element model was developed to identify the presence of loss of connection. From the R-index, a quadratic pattern of R-index was observed when plotted with loss of torque. Thus, a quadratic curve was able to approximate the mean values obtained in the analyses so far.

From the fitting curve proposed to the R-index, a confidence interval with 95% of confidence could be calculated. After having seen that the residue was robust in terms of position and number of sensors, the acceleration was collected only at the beam tip at x = L. The force used was $\mathrm{F(t)} = 100\cos(1000\pi \mathrm{t})$ N, applied at x = L/5, x = 2L/5, x = 3L/5, x = 4L/5, and x = L.

For data normally distributed, the confidence interval (CI) commonly used in inferential statistics can be obtained using the standard deviation of the data s through (Altman and Machin, 2000):

$$\mathrm{CI} = \overline{\mathrm{X}} \pm \mathrm{Z}\frac{\mathrm{s}}{\sqrt{\mathrm{N}}}\ , \tag{5.3}$$

where $\overline{\mathrm{X}}$ is the population mean, Z is the chosen Z-value for the confidence interval and N is the number of samples. For a 95% confidence level, Z = 1.96. Lower and upper limits of the confidence bound curves estimate a range from a standard or typical behavior based on the collected data. With the curves, it would be possible to estimate a confidence interval within it may contain an R-index value. Then, the knowledge of the geometrical features of the beam would no longer be necessary and only the measurements would be relevant.

For the solution of the inverse problem, with acceleration readings in the y direction at the beam tip, it could be estimated that the value corresponds to a certain value of torque loss. With the confidence interval, it would be possible to estimate a torque loss even if the R-index presents some variations. Therefore, calculating the confidence interval is used as a strategy assuming a sampling error. The lower and upper sizes of the confidence interval indicate the possible values that could occur. Therefore, the closer the curves are to the confidence interval, the better the estimate.

As shown in Figure 5.11, different simulated cases could be approximated by a single

quadratic curve:

$$\mathrm{R} = 2.4949\mathrm{T}^2 + 0.7112\mathrm{T}\ , \tag{5.4}$$

where T was the torque loss. Using the fitting curve to normalize the residue, it was possible to obtain the highest signal value through the proposed equation for R-index. With this, a confidence bound was calculated for this new mean curve, as shown in Figure 5.12. It was possible to notice that, as expected, the curves were very close with lower damages and were opening up as the loss of torque was increased. This behavior was also seen in Figure 5.9a with the non-normalized residue.

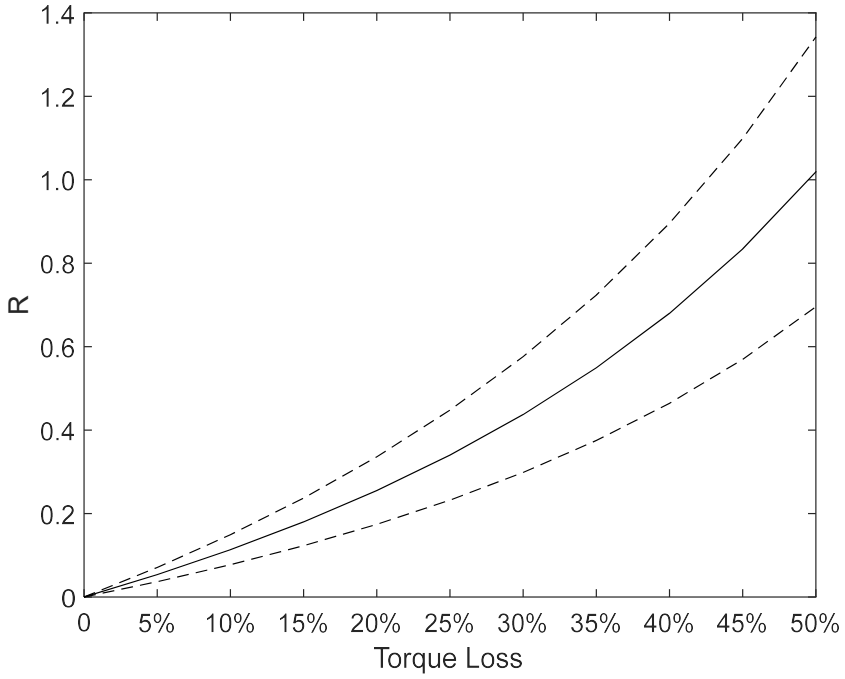

Figure 5.12. Confidence interval (- -) with 95% confidence and the R fitting curve (-).

Eventually, a first attempt to calculate the inverse solution was performed by estimating the torque loss in the bolts through the residue obtained in relation to the healthy beam. Taking as an example $\mathrm{R-index} = 0.1$, the corresponding damage would be between 1.8% and 3.5%. On average, it would be possible to estimate that the torque loss value would be approximately 2.7%. From the average curve normalized by the maximum value found from the equation of R-index, the torque loss found would be 2.4%. But, approaching through the quadratic fitting proposed for the R-index, the torque loss found would be 3.2%. In this case, the value 3.2% would also be within the confidence interval that was plotted between 1.8% and 3.5%. In any case, the approximation using the mean confidence interval and the R-index equation resulted in approximate values with a difference of 0.5% in torque loss. In Figure 5.13 it is possible to observe the values described within the confidence interval shown in Figure 5.12.

The confidence interval calculated presented a range of possible mean values related to the loss of torque. If a given calculated R-index does not fall within this range, then it would

be possible to infer that this value is probably not the true mean value related to that torque loss. However, even if this calculated residual value were within the range, it would still not be possible to infer that the average value related to this loss of torque would be this specific value, which was seen with the value of 2.7%.

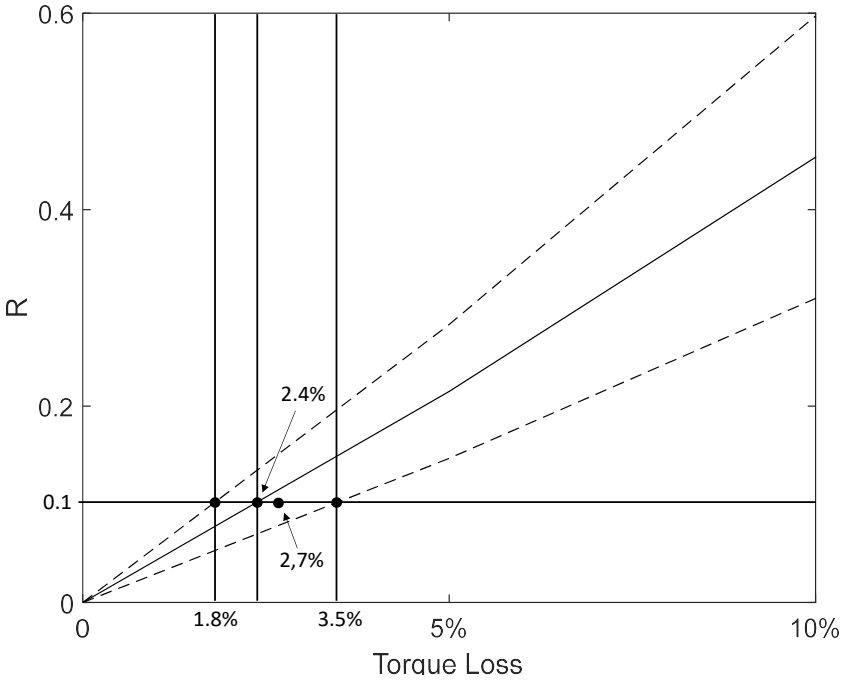

Figure 5.13. R-index values found on the confidence interval (- -) with 95% confidence and fitting curve R (-).

A more noteworthy study on the confidence interval can be done with noise applied to the signals, as will be presented in next section. It is important to consider that until now, uncertainties in the collected measurements have not been considered, an intrinsic characteristic of measurements using sensors.

5.5 TESTING R-INDEX WITH WHITE NOISE

From a new section, presented in Figure 4.9, some numerical simulations were carried out regarding the transient behavior of the beam with elastic boundary conditions. After observing the same behavior found in the beam previously analyzed when looking at R-index results, as shown in Figure 5.14, the acceleration signals were exposed to noise at controlled levels to infer the robustness of the damage detection methods presented in this study. At this stage, the force was applied only at x = L/2, after having seen that the R-index was robust in relation to the position of application of the force.

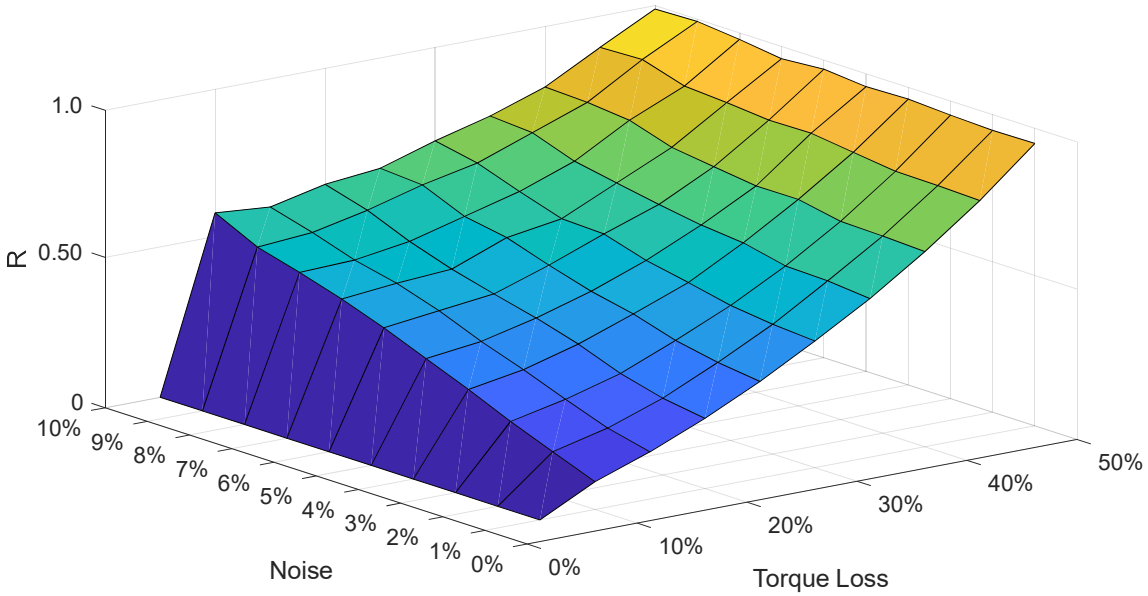

Figure 5.14. R-index behavior on different noise levels for the new section.

As seen by Barros *et al.* (2023), Sangiorgio *et al.* (2022), Chou and Nguyen (2022), and Fan *et al.* (2020) most studies using Gaussian noise on SHM validations range from 1.0% to 2.5% of noise level. Fan *et al.* (2020) reported that the noise level above 10% is considered too high, only found in some in-field tests with a poor setup for instance.

In this study, the acceleration signal in the vertical direction was contaminated with Gaussian noise, whose levels ranged from 1% to 5%, with variations of 1%, according to Equation 4.2. The noise was generated from the amplitudes of the acceleration signal and the R-index was recalculated.

At that moment, the results were calculated by taking the data at all beam sensors, i.e., all the 21 equally spaced sensors recorded their results of acceleration for 4 s. Figure 5.15 presents the results obtained for R-index as a function of the torque reductions for different levels of noise adding. It is possible to observe that as the noise level increases the R-index value also increases, for the lowest levels of noise R-index values are similar to those previously computed. This could interfere with the damage detection process by solving the inverse problem.

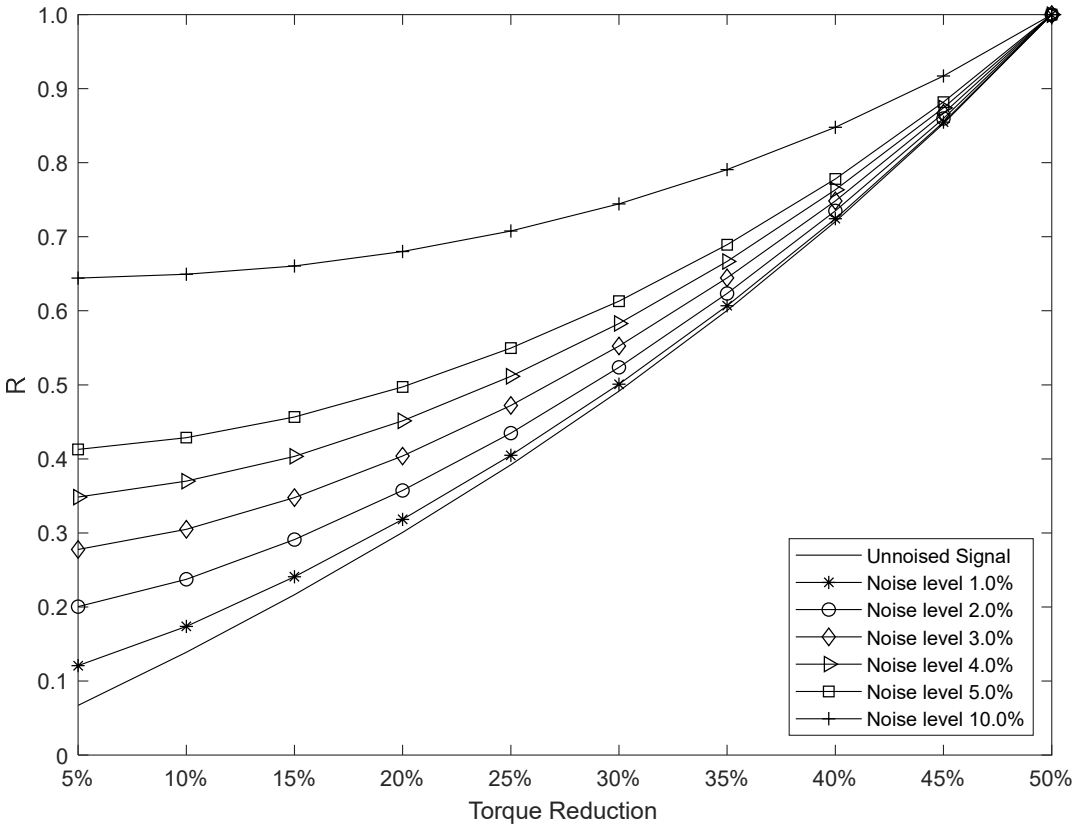

Figure 5.15. R-index behavior on different noise levels taken during 4s with 21 sensors.

Furthermore, in Figure 5.15 is possible to observe a high level of noise with 10%, where variations only begin to become significant above 30%. Furthermore, it is possible to observe that the slope of the less accentuated curve makes it difficult to solve the inverse problem, since low R-index can correspond to either low or medium values of torque loss.

It was expected that the R-index value is deeply interfered by the considered period of the noise observation and the quantity of the sensors considered to compute the value of R-index. To evaluate the interference of noise accumulation in the calculation of the R-index, different time frames were compared with noise-contaminated acceleration signals.

In this regard, it was first windowed the signals at different time observation. The acceleration signals were contaminated with noise level of 3% and different time frames were evaluated, ranging from 1 s up to 8 s, as shown in Figure 5.16. With the different noise time, it was possible to observe that: 1) due to the structure of the calculation of R-index, the noise was accumulated over time, 2) such accumulation makes the R-index to move away from the unnoised signal, much more than expected, as presented in Figure 5.16.

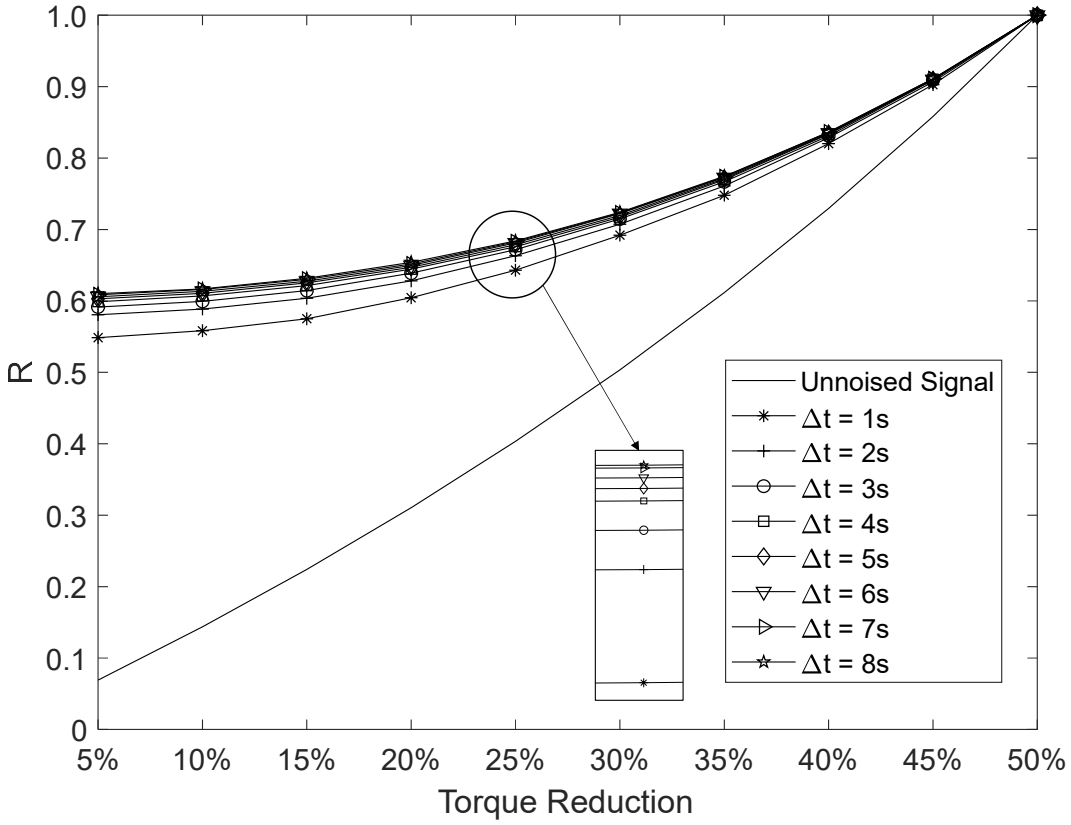

Figure 5.16. R-index behavior for different time frames with noise level of 3% with 21 sensors.

In Figure 5.17, the R-index results are presented before normalizing, Figure 5.17a, and normalized, Figure 5.17b, with 1% noise applied to the data for three time intervals. It is possible to observe that before normalization, there is an evident accumulation with increasing time interval. However, with normalization, Figure 5.17, the results are very close to each other. It was decided to continue the evaluations with the shortest time interval once to reduce the computational time of the analyses.

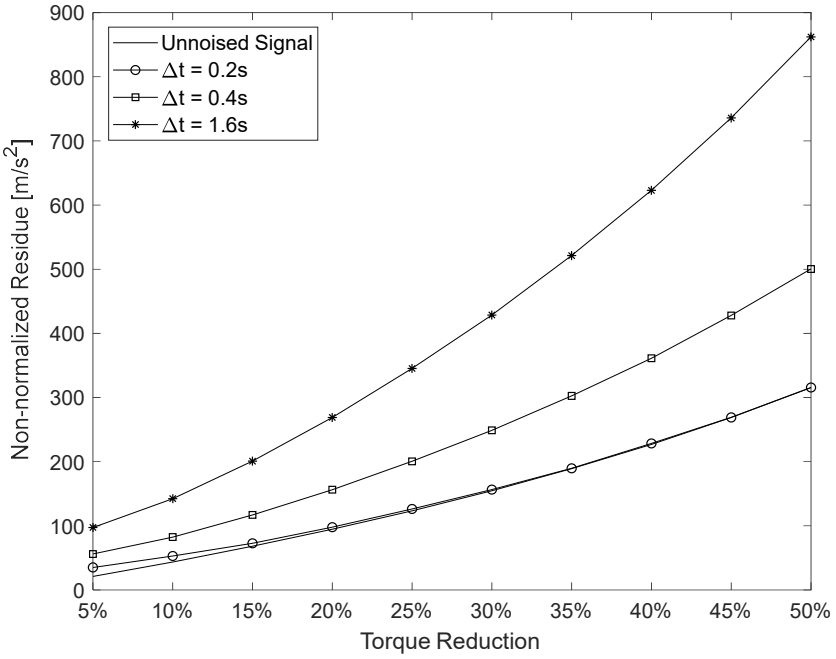

(a) Non-normalized R-index with 1% noise with different time interval.

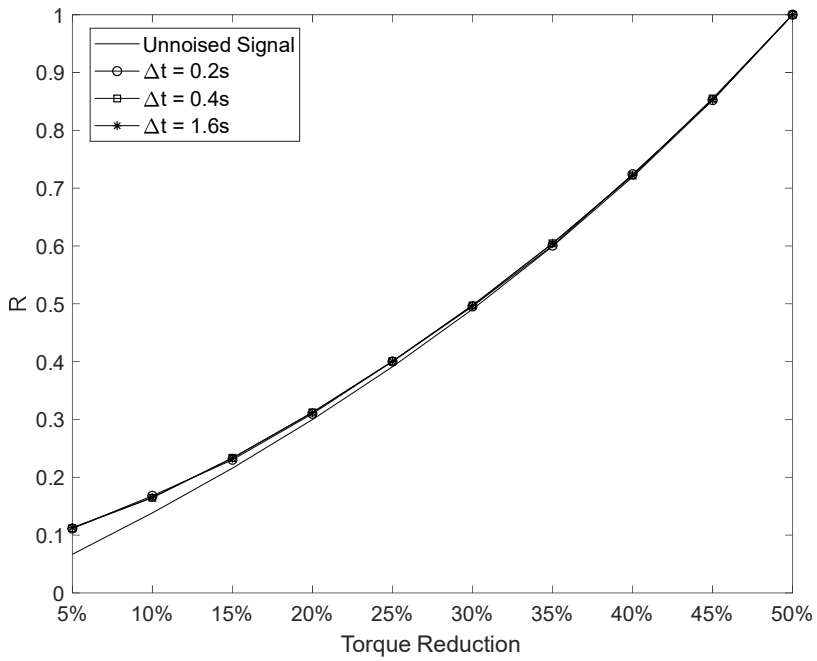

(b) R-index with 1% noise with different time interval.

Figure 5.17. Comparison of R-index results for different time interval with 1% noise in acceleration data, Δt = 0.2 s, 0.4 s and 1.6 s.

Next, in order to reduce the influence of noise on the residue, an evaluation was made with some sensors selected in order to calculate R based on data from just one sensor and compare to with R based on the average acceleration of them. Now using the time spacing of 0.2 s and 3% of noise level, the sensor results were evaluated at x = L and x = 4L/5. Once this was done, the average of the accelerations resulted in an R-index $\times$ Torque Loss ratio as robust as that observed with the signal without noise contamination, as shown in Figure 5.18. Indeed, from the results in Figure 5.18 it is possible to infer that: 1) The results of the R-index calculated at the beam tip present a noisier relation probably due to the higher acceleration peaks. 2) Using only one acceleration sensor gives better results than averaging the R-index, however, 3) taking the average of the acceleration signal of the 21 sensors before calculating R-index appears to be the procedure that most closely approximates the result contaminated with noise from the result unnoised.

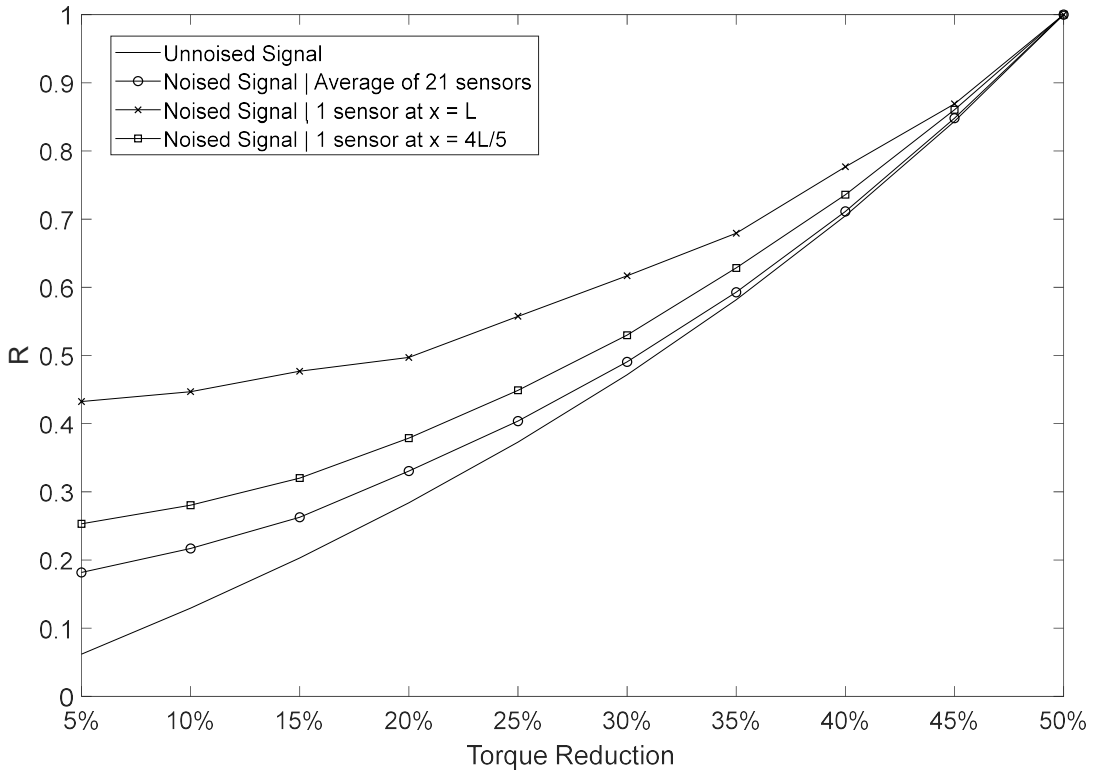

Figure 5.18. R-index behavior contaminated with 3% noise with average on 21 sensors, one sensor at x = L and one sensor at x = 4L/5.

As such, it was deduced that the best signal-to-noise ratio is obtained using a frame time of 0.2 s and averaging the sensors before calculating the R-index instead of the average R-index. Figure 5.19 shows the results obtained for the acceleration signal contaminated by different noise levels varying between 1% and 5% during 0.2 s. These findings will be utilized to derive a confidence interval and develop the confidence bounds curves to compare the outcomes of the noise-free study step.

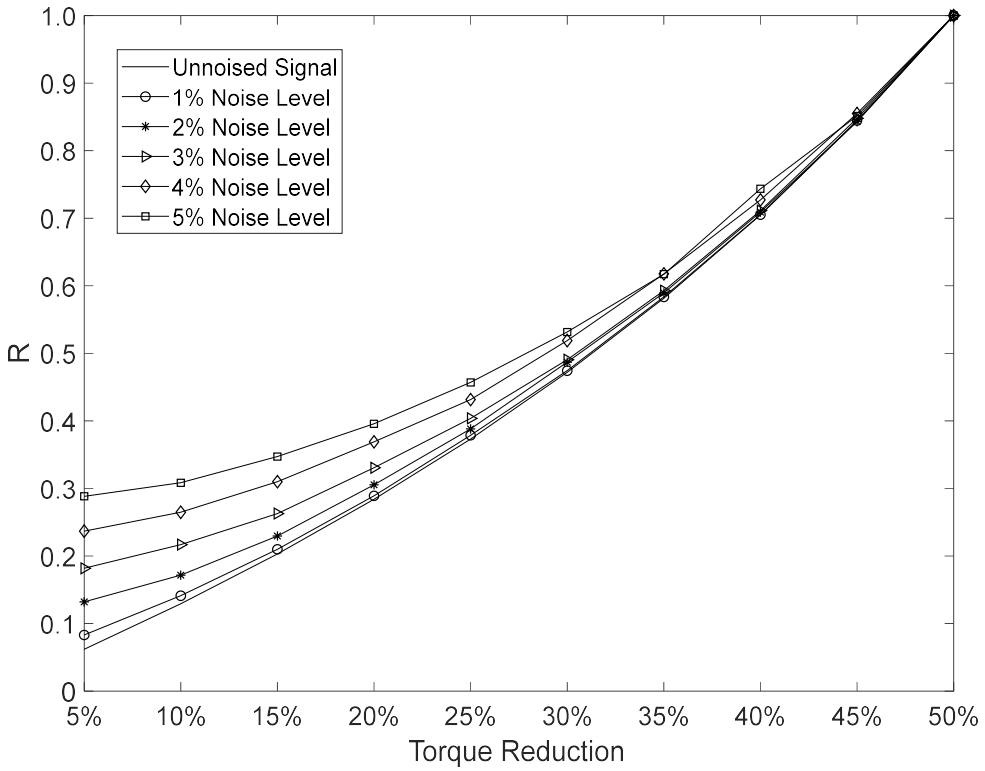

Figure 5.19. R-index of the unnoised and noised signal with noise level from 1% to 5% with average data.

In this sense, the confidence interval is calculated based on the results of noise variations found between 1% and 5% for a more comprehensive case of level noise. In Figure 5.20 it is possible to observe the confidence interval curves obtained for the curves contaminated with noise levels between 1% and 5%. The fitting curve found is now $\mathrm{R} = 19.409\mathrm{T}^2 + 41.586\mathrm{T}$, where T corresponds to the torque loss. Unlike what was observed in the curves obtained previously in the study without noise, the curves approach as the torque loss increases. In this sense, the utilization of confidence intervals proved to be a valuable statistical tool for estimating torque losses only above at least 25% with noised signals.

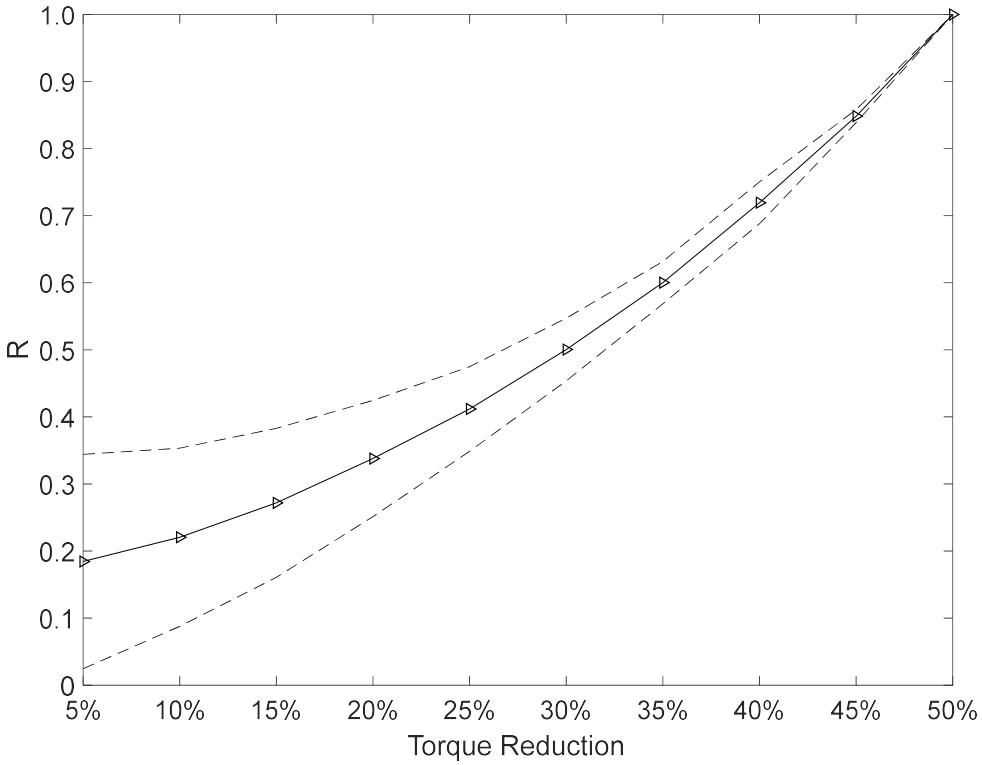

Figure 5.20. Confidence interval (- -) with 95% confidence and the R-index curve (-) found for for noise levels between 1% and 5%.

This behavior reflects a difficulty seen in the identification of low torque losses, seen in several stages of this study. When noise was introduced, it became apparent that the variations of the R-index remained relatively low for minor torque losses. This behavior occurred regardless of the noise level added to the acceleration signal, although it became more pronounced as the noise levels increased.

6 CONCLUSION

Within the converge analyses, quadratic and cubic shape functions, even with a discretization of 20 nodes, exhibited better agreement with the reference case than linear interpolation. As the objective was to present a low-order fidelity model, the configuration of 20 nodes using quadratic shape functions was chosen. The simpler model with fewer elements was selected for practicality and cost savings, as real-world applications often involve limitations on the number of sensors. The maximum relative error between the reference case and the selected working model was found to be 0.91%. The error, especially at lower frequencies, was assumed negligible. During the convergence analysis, it was also shown that the numerical model with an elastic connection could be used as the representation of a perfectly fixed beam with high stiffness values.

The initial study of how frequencies and the model behaved with low stiffness values was made to evaluate the behavior of the model and modes as there was a decrease in the rigidity of the problem. During this analysis, it was observed that rotational stiffness ($\mathrm{K_{rot}}$) variations around the z-axis had significant effects on the natural frequencies. Also, the flexural stiffness in the y-axis ($\mathrm{K_{uy}}$) variations mainly affected the xy bending modes. Variations in stiffness in other directions did not affect the behavior of the beam significantly in the plane relevant to the problem.

Utilizing torque losses associated with $\mathrm{K_{uy}}$ and $\mathrm{K_{rotz}}$, the proposed R-index was used to identify variations in data readings and their influence on damage detection. Analyzes showed that the R-index remained unchanged regardless of force positioning and sensor positioning, proving its robustness to these variations. This robustness of the R-index, regardless of sensor distribution and force application position, indicates its potential for real-world structural health monitoring applications.

The damage applied to the elastic connection was controlled through loss of torque. When the results of R-index and torque loss were summarized, a distinct and repeated relationship was seen. Through the average results, a quadratic fitting curve was proposed so the solution to the inverse problem could be carried out by associating an R-index value with a loss of torque. Even if the curve were more complex it would still be a simpler method than solving the inverse problem through a genetic algorithm or other similar method.

Using the R-index fitting curve, a confidence interval was calculated with 95% confidence with upper and lower intervals providing a range of typical behavior based on results. When solving the inverse problem using the confidence interval, it was possible to detect even the

lowest levels of damage. The estimation of confidence intervals enabled the forecast of torque loss even without precise knowledge of the structure geometry. By combining the R-index and confidence bounds, a robust method could be presented to find torque losses on bolted joints.

A hollow section geometry was used to evaluate the noisy data. As expected, without the applied noise, the same conclusions seen for the continuous beam remained. When White Gaussian noise ranging between 1% and 5% was applied to the collected acceleration, the damage detection accuracy was compromised, particularly for torque losses below 25%.

An analysis was carried out on the data acquisition time and concluded that 0.2 s of observation resulted in a smaller dispersion of the noise-free signal. Regarding the number of sensors, it was observed that using the average of the 21 sensors to calculate the R-index presented results closer to the noise-free signal. Therefore, a new fitting curve was calculated to predict damage to the beam connections with the presence of noise between 1% and 5% in the collected data. As expected, it was observed that the R curve is problem-dependent. Also, the confidence interval proved to be more efficient as the torque loss increased, especially above 25%.

The results and discussions demonstrated that the proposed objectives were successfully achieved. The quadratic fitting curve employed to correlate the R-index with torque losses simplified the process of solving the inverse problem while demonstrating substantial robustness. The confidence interval improved damage detection accuracy, emphasizing the practicality and effectiveness of this method. Also, the examination of noisy data scenarios highlighted the adaptability of this approach in predicting beam connection damage, offering potential for future research and practical applications in structural health monitoring. In this sense, there are several opportunities for this issue to develop further research, as presented in the next section.

6.1 SUGGESTIONS FOR FUTURE RESEARCHES

Over the development of this work, some topics were identified as relevant to the evolution of the research presented:

- Study other residual options for the same analyses developed during the research, such as using the modal energy of deformation or another response difference in the time domain;
- Analyze the problem with other types of force distribution along the beam;
- Apply uncertainty to other properties of the problem, such as loading, structure, and material properties;
- Compare different techniques for diagnosing damage, comparing optimization methods, and identifying and qualifying methods.

REFERENCE LIST

Adeppa, A., Patil, M., e Girish, K. (2012). Stress analysis and fatigue life prediction for splice joint in an aircraft fuselage through an fem approach. *International Journal of Engineering and Innovative Technology (IJEIT)*, 1(4):142–144.

Aliabadi, M. F. e Khodaei, Z. S. (2017). *Structural health monitoring for advanced composite structures*, volume 8. World Scientific.

Altman, D. e Machin, D. (2000). *Statistics with Confidence: Confidence Intervals and Statistical Guidelines*. BMJ Books.

Barros, B., Conde, B., Cabaleiro, M., e Riveiro, B. (2023). Design and testing of a decision tree algorithm for early failure detection in steel truss bridges. *Engineering Structures*, 289:116243.

Baskaran, P., Pasadas, D. J., Ramos, H. G., e Ribeiro, A. L. (2021). Integration of multiple response signals into the probability of detection modelling in eddy current nde of flaws. *NDT and E International*, 118.

Bender, A. (2023). Model-based condition monitoring of piezoelectric bending actuators. *Sensors and Actuators A: Physical*, 357:114399.

Bickford, J. H. (2007). *Introduction to the design and behavior of bolted joints: non-gasketed joints*. CRC press.

Bretanha, A. J. (2020). Plataforma demonstradora tecnológica para métodos inversos e modelagem de incertezas em integridade de estruturas e componentes. `https://repositorio.unb.br/handle/10482/39570`.

Callister Jr, W. D. (2007). *Materials science and engineering an introduction*.

Cao, P., Zhang, S., Wang, Z., e Zhou, K. (2023). Damage identification using piezoelectric electromechanical impedance: a brief review from a numerical framework perspective. In *Structures*, volume 50, páginas 1906–1921. Elsevier.

Chaupal, P. e Rajendran, P. (2023). A review on recent developments in vibration-based damage identification methods for laminated composite structures: 2010–2022. *Composite Structures*, página 116809.

Chen, G., Guo, Y., Katagiri, T., Song, H., Tomizawa, T., Yusa, N., e Hashizume, H. (2021). Multivariate probability of detection (pod) analysis considering the defect location for long-range, non-destructive pipe inspection using electromagnetic guided wave testing. *NDT and E International*, 124.

Chou, J.-S. e Nguyen, N.-M. (2022). Scour depth prediction at bridge piers using metaheuristics-optimized stacking system. *Automation in Construction*, 140:104297.

Concli, F., Pierri, L., e Sbarufatti, C. (2021). A model-based shm strategy for gears—development of a hybrid fem-analytical approach to investigate the effects of surface fatigue on the vibrational spectra of a back-to-back test rig. *Applied Sciences*, 11(5):2026.

Cunha, B. Z., Droz, C., Zine, A.-M., Foulard, S., e Ichchou, M. (2023). A review of machine learning methods applied to structural dynamics and vibroacoustic. *Mechanical Systems and Signal Processing*, 200:110535.

Fan, G., Li, J., e Hao, H. (2020). Vibration signal denoising for structural health monitoring by residual convolutional neural networks. *Measurement*, 157:107651.

Fernandez-Navamuel, A., Zamora-Sánchez, D., Omella, Á. J., Pardo, D., Garcia-Sanchez, D., e Magalhães, F. (2022). Supervised deep learning with finite element simulations for damage identification in bridges. *Engineering Structures*, 257:114016.

Gao, C., Fang, Z., Lin, J., Guan, X., e He, J. (2022). Model averaging and probability of detection estimation under hierarchical uncertainties for lamb wave detection. *Mechanical Systems and Signal Processing*, 165.

García-Macías, E., Ierimonti, L., Venanzi, I., e Ubertini, F. (2020). Comparison of surrogate models for handling uncertainties in shm of historic buildings. In *Proceedings of XXIV AIMETA Conference 2019 24*, páginas 1645–1657. Springer.

Gaul, L. e Nitsche, R. (2001). The role of friction in mechanical joints.

Giannakeas, I. N., Mazaheri, F., Bacarreza, O., Khodaei, Z. S., e Aliabadi, F. M. (2023). Probabilistic residual strength assessment of smart composite aircraft panels using guided waves. *Reliability Engineering & System Safety*, 237:109338.

Hou, R. e Xia, Y. (2021). Review on the new development of vibration-based damage identification for civil engineering structures: 2010–2019. *Journal of Sound and Vibration*, 491:115741.

Inman, D. J. (2014). *Engineering Vibration*, volume 4th Edition. Pearson.

Jalali, H., Khodaparast, H. H., e Friswell, M. I. (2019). The effect of preload and surface roughness quality on linear joint model parameters. *Journal of Sound and Vibration*, 447:186–204.

Jorge, A. B., Anflor, C. T. M., Gomes, G. F., e Carneiro, S. H. d. S. (2022). Uncertainty modeling: fundamental concepts and models.

Kim, F. H., Pintar, A., Obaton, A. F., Fox, J., Tarr, J., e Donmez, A. (2021). Merging experiments and computer simulations in x-ray computed tomography probability of detection analysis of additive manufacturing flaws. *NDT and E International*, 119.

Kuo, Y., Cleghorn, W., Behdinan, K., e Fenton, R. (2006). The h–p–r-refinement finite element analysis of a planar high-speed four-bar mechanism. *Mechanism and machine theory*, 41(5):505–524.

Li, M., Wu, Z., Yang, H., e Huang, H. (2021). Direct damage index based on inverse finite element method for structural damage identification. *Ocean Engineering*, 221:108545.

Liao, X., Zhang, J., e Xu, X. (2016). Analytical model of bolted joint structure and its nonlinear dynamic characteristics in transient excitation. *shock and vibration*.

Liu, H., Jia, L., Wen, S., Liu, Q., Wang, G., e Chen, Z. (2016). Experimental and theoretical studies on the stability of steel tube–coupler scaffolds with different connection joints. *Engineering Structures*, 106:80–95.

Liu, Y., Xin, H., He, J., Xue, D., e Ma, B. (2013). Experimental and analytical study on fatigue behavior of composite truss joints. *Journal of Constructional Steel Research*, 83:21–36.

Lourenço, P. H. (2004). O método dos elementos finitos aplicado ao estudo de juntas rigidamente fixadas por parafusos.

Moradi, M., Broer, A., Chiachío, J., Benedictus, R., Loutas, T. H., e Zarouchas, D. (2023). Intelligent health indicator construction for prognostics of composite structures utilizing a semi-supervised deep neural network and shm data. *Engineering Applications of Artificial Intelligence*, 117:105502.

Nguyen, P.-C. e Kim, S.-E. (2014). An advanced analysis method for three-dimensional steel frames with semi-rigid connections. *Finite Elements in Analysis and Design*, 80:23–32.

Nikravesh, S. M. Y. e Goudarzi, M. (2017). A review paper on looseness detection methods in bolted structures. *Latin American Journal of Solids and Structures*, 14:2153–2176.

Norton, J., Arraez, C., *et al.* (2000). *Machine design*. Citeseer.

Oppenheim, A. V., Willsky, A. S., Nawab, S. H., e Ding, J.-J. (1997). *Signals and systems*, volume 2. Prentice hall Upper Saddle River, NJ.

Popp, K. (1998). Non-smooth mechanical systems—an overview. *Forschung im ingenieurwesen*, 64(9):223–229.

Qiu, Q., Wu, J., Chen, X., Xia, H., Zhang, M., e Zhu, J. (2021). Tensile stress effect on crack depth quantification in ferromagnetic materials using ecpt. *Measurement: Journal of the International Measurement Confederation*, 182.

Razavi, M. e Hadidi, A. (2021). Structural damage identification through sensitivity-based finite element model updating and wavelet packet transform component energy. In *Structures*, volume 33, páginas 4857–4870. Elsevier.

Ross, R. (2016). Integrated vehicle health management in aerospace structures. In *Structural Health Monitoring (SHM) in Aerospace Structures*, páginas 3–31. Elsevier.

Rulli, R. P., Bueno, C. G. G., Dotta, F., e Silva, P. A. d. (2016). Damage detection systems for commercial aviation. In *Dynamics of Smart Systems and Structures*, páginas 329–342. Springer.

Sangiorgio, V., Nettis, A., Uva, G., Pellegrino, F., Varum, H., e Adam, J. M. (2022). Analytical fault tree and diagnostic aids for the preservation of historical steel truss bridges. *Engineering Failure Analysis*, 133:105996.

Shigley, J. E. (2011). *Shigley's mechanical engineering design*. Tata McGraw-Hill Education.

Sivasuriyan, A., Vijayan, D., LeemaRose, A., Revathy, J., Gayathri Monicka, S., Adithya, U., e Jebasingh Daniel, J. (2021). Development of smart sensing technology approaches in structural health monitoring of bridge structures. *Advances in Materials Science and Engineering*, 2021.

Speckmann, H. e Henrich, R. (2004). Structural health monitoring (shm)–overview on technologies under development. In *Proceedings of the 16th World Conference on NDT*, volume 1.

Spinelli, H. d. A. (2004). Análise estrutural de juntas rebitadas de uso aeronaútico.

Wang, F., Han, Y., e Yang, J. (2021). Nonlinear fe analysis on stiffness and resistance of bolted cold-formed steel built-up joints. In *Structures*, volume 33, páginas 2520–2533. Elsevier.

Xue, D., Liu, Y., He, J., e Ma, B. (2011). Experimental study and numerical analysis of a composite truss joint. *Journal of Constructional Steel Research*, 67(6):957–964.

Zadanfarrokh, F. e Bryan, E. (1992). Testing and design of bolted connections in cold formed steel sections.

Zhan, Y., Lu, S., Xiang, T., e Wei, T. (2021). Application of convolutional neural network in random structural damage identification. In *Structures*, volume 29, páginas 570–576. Elsevier.

APPENDIX A

MODAL ANALYSIS WITH DIFFERENT INTERPOLATION FUNCTIONS

Table A1. Natural frequencies and deformation descriptions using 20 elements with different shape functions in a cantilever beam.

Mode Description	Natural Frequency [Hz]			
	Analytical Solution	Linear Interpolation	Quadratic Interpolation	Cubic Interpolation
1st bending mode in xy	14.14	14.14	14.14	14.14
1st bending mode in xz	56.55	56.49	56.48	56.48
2nd bending mode in xy	88.60	89.04	88.55	88.55
3rd bending mode in xy	248.08	251.74	247.76	247.75
2nd bending mode in xz	354.39	353.16	351.26	351.25
4th bending mode in xy	486.13	500.98	485.03	484.94
1st torsional mode in x		607.48	607.33	607.33
5th bending mode in xy	803.61	845.64	800.86	800.46
3rd bending mode in xz	992.31	987.07	971.85	971.80
6th bending mode in xy	1200.46	1297.10	1194.90	1193.60
7th bending mode in xy	1676.68	1826.20	1667.10	1663.60
2nd torsional mode in x		1870.90	1822.00	1822.00
4th bending mode in xz	1944.54	1931.50	1872.80	1872.40
1st longitudinal mode		2188.50	2187.90	2187.90
8th bending mode in xy	2232.26	2587.10	2217.60	2209.50
9th bending mode in xy	2867.22	3056.20	2847.10	2830.20
5th bending mode in xz	3214.46	3190.20	3032.70	3031.30
3rd torsional mode in x		3471.50	3036.70	3036.60
10th bending mode in xy	3581.54	4305.00	3556.70	3524.80

Table A2. Natural frequencies and deformation descriptions using 40 elements with different shape functions in a cantilever beam.

Mode Description	Natural Frequency [Hz]			
	Analytical Solution	Linear Interpolation	Quadratic Interpolation	Cubic Interpolation
1st bending mode in xy	14.14	14.14	14.14	14.14
1st bending mode in xz	56.55	56.48	56.48	56.48
2nd bending mode in xy	88.60	88.67	88.55	88.55
3rd bending mode in xy	248.08	248.74	247.75	247.75
2nd bending mode in xz	354.39	351.73	351.25	351.25
4th bending mode in xy	486.13	488.89	484.94	484.94
1st torsional mode in x		607.37	607.33	607.33
5th bending mode in xy	803.61	811.47	800.49	800.46
3rd bending mode in xz	992.31	975.59	971.80	971.80
6th bending mode in xy	1200.46	1218.50	1193.70	1193.60
7th bending mode in xy	1676.68	1712.50	1663.80	1663.60
2nd torsional mode in x		1823.00	1822.00	1822.00
4th bending mode in xz	1944.54	1887.00	1872.50	1872.40
1st longitudinal mode		2188.10	2187.90	2187.90
8th bending mode in xy	2232.26	2296.80	2209.90	2209.40
9th bending mode in xy	2867.22	2975.00	2831.20	2830.00
5th bending mode in xz	3214.46	3041.50	3031.40	3031.30
3rd torsional mode in x		3070.10	3036.60	3036.60
10th bending mode in xy	3581.54	3751.70	3526.40	3524.30

Table A3. Natural frequencies and deformation descriptions using 80 elements with different shape functions in a cantilever beam.

Mode Description	Natural Frequency [Hz]			
	Analytical Solution	Linear Interpolation	Quadratic Interpolation	Cubic Interpolation
1st bending mode in xy	14.14	14.14	14.14	14.14
1st bending mode in xz	56.55	56.48	56.48	56.48
2nd bending mode in xy	88.60	88.58	88.55	88.55
3rd bending mode in xy	248.08	247.99	247.75	247.75
2nd bending mode in xz	354.39	351.37	351.25	351.25
4th bending mode in xy	486.13	485.92	484.94	484.94
1st torsional mode in x		607.34	607.33	607.33
5th bending mode in xy	803.61	803.19	800.46	800.46
3rd bending mode in xz	992.31	972.75	971.80	971.80
6th bending mode in xy	1200.46	1199.80	1193.60	1193.60
7th bending mode in xy	1676.68	1675.60	1663.60	1663.60
2nd torsional mode in x		1822.20	1822.00	1822.00
4th bending mode in xz	1944.54	1876.10	1872.40	1872.40
1st longitudinal mode		2188.00	2187.90	2187.90
8th bending mode in xy	2232.26	2230.80	2209.40	2209.40
9th bending mode in xy	2867.22	2865.40	2830.10	2830.00
5th bending mode in xz	3214.46	3037.90	3031.30	3031.30
3rd torsional mode in x		3040.90	3036.60	3036.60
10th bending mode in xy	3581.54	3579.30	3524.40	3524.30

Table A4. Natural frequencies and deformation descriptions using 160 elements with different shape functions in a cantilever beam.

Mode Description	Natural Frequency [Hz]			
	Analytical Solution	Linear Interpolation	Quadratic Interpolation	Cubic Interpolation
1st bending mode in xy	14.14	14.14	14.14	14.14
1st bending mode in xz	56.55	56.48	56.48	56.48
2nd bending mode in xy	88.60	88.56	88.55	88.55
3rd bending mode in xy	248.08	247.81	247.75	247.75
2nd bending mode in xz	354.39	351.28	351.25	351.25
4th bending mode in xy	486.13	485.18	484.94	484.94
1st torsional mode in x		607.33	607.33	607.33
5th bending mode in xy	803.61	801.14	800.46	800.46
3rd bending mode in xz	992.31	972.04	971.80	971.80
6th bending mode in xy	1200.46	1195.10	1193.60	1193.60
7th bending mode in xy	1676.68	1666.60	1663.60	1663.60
2nd torsional mode in x		1822.00	1822.00	1822.00
4th bending mode in xz	1944.54	1873.30	1872.40	1872.40
1st longitudinal mode		2187.90	2187.90	2187.90
8th bending mode in xy	2252.26	2214.70	2209.40	2209.40
9th bending mode in xy	2867.22	2838.80	2830.00	2830.00
5th bending mode in xz	3214.46	3033.70	3031.30	3031.30
3rd torsional mode in x		3036.90	3036.60	3036.60
10th bending mode in xy	3581.54	3537.90	3524.30	3524.30

APPENDIX B

NATURAL FREQUENCIES WITH STIFFNESS VARIATIONS

Table B1. Natural frequencies obtained with $\mathrm{K_{ux}}$ variations ($\mathrm{K_{rotx}} = \mathrm{K_{roty}} = \mathrm{K_{rotz}} = 1 \times 10^{20}$ Nm/rad and $\mathrm{K_{uy}} = \mathrm{K_{uz}} = 1 \times 10^{20}$ N/m).

Mode Description	Natural Frequency [Hz]							
	$\mathrm{K_{ux}}$ 1×10^{20} N/m	$\mathrm{K_{ux}}$ 1×10^{10} N/m	$\mathrm{K_{ux}}$ 1×10^{5} N/m	$\mathrm{K_{ux}}$ 1×10^{4} N/m	$\mathrm{K_{ux}}$ 1×10^{3} N/m	$\mathrm{K_{ux}}$ 1×10^{2} N/m	$\mathrm{K_{ux}}$ 1×10^{1} N/m	$\mathrm{K_{ux}}$ 1 N/m
1st bending mode in xy	14.14	14.14	14.14	14.14	14.14	14.14	14.14	14.14
1st bending mode in xz	56.48	56.48	56.48	56.48	56.48	56.48	56.48	56.48
2nd bending mode in xy	88.55	88.55	88.55	88.55	88.55	88.55	88.55	88.55
3rd bending mode in xy	247.76	247.76	247.76	247.76	247.76	247.76	247.76	247.76
2nd bending mode in xz	351.26	351.26	351.26	351.26	351.26	351.26	351.26	351.26
4th bending mode in xy	485.03	485.03	485.03	485.03	485.03	485.03	485.03	485.03
1st torsional mode in x	607.33	607.33	607.33	607.33	607.33	607.33	607.33	607.33
5th bending mode in xy	800.86	800.86	800.86	800.86	800.86	800.86	800.86	800.86
3rd bending mode in xz	971.85	971.85	971.85	971.85	971.85	971.85	971.85	971.85
6th bending mode in xy	1194.90	1194.90	1194.90	1194.90	1194.90	1194.90	1194.90	1194.90
7th bending mode in xy	1667.10	1667.10	1667.10	1667.10	1667.10	1667.10	1667.10	1667.10
2nd torsional mode in x	1822.00	1822.00	1822.00	1822.00	1822.00	1822.00	1822.00	1822.00
4th bending mode in xz	1872.80	1872.80	1872.80	1872.80	1872.80	1872.80	1872.80	1872.80
1st longitudinal mode	2187.90	2170.00	48.42	15.31	4.84	1.53	0.48	0.15
8th bending mode in xy	2217.60	2217.60	2217.60	2217.60	2217.60	2217.60	2217.60	2217.60
9th bending mode in xy	2847.10	2847.10	2847.10	2847.10	2847.10	2847.10	2847.10	2847.10
5th bending mode in xz	3032.70	3032.70	3032.70	3032.70	3032.70	3032.70	3032.70	3032.70
3rd torsional mode in x	3036.70	3036.70	3036.70	3036.70	3036.70	3036.70	3036.70	3036.70
10th bending mode in xy	3556.70	3556.70	3556.70	3556.70	3556.70	3556.70	3556.70	3556.70

Table B2. Natural frequencies obtained with $\mathrm{K_{uz}}$ variations ($\mathrm{K_{rotx}} = \mathrm{K_{roty}} = \mathrm{K_{rotz}} = 1 \times 10^{20}$ Nm/rad and $\mathrm{K_{ux}} = \mathrm{K_{uy}} = 1 \times 10^{20}$ N/m).

Mode Description	Natural Frequency [Hz]							
	$\mathrm{K_{uz}}$ 1×10^{20} N/m	$\mathrm{K_{uz}}$ 1×10^{10} N/m	$\mathrm{K_{uz}}$ 1×10^{5} N/m	$\mathrm{K_{uz}}$ 1×10^{4} N/m	$\mathrm{K_{uz}}$ 1×10^{3} N/m	$\mathrm{K_{uz}}$ 1×10^{2} N/m	$\mathrm{K_{uz}}$ 1×10^{1} N/m	$\mathrm{K_{uz}}$ 1 N/m
1st bending mode in xy	14.14	14.14	14.14	14.14	14.14	14.14	14.14	14.14
1st bending mode in xz	56.48	56.48	38.86	14.97	4.83	1.53	0.48	0.15
2nd bending mode in xy	88.55	88.55	88.55	88.55	88.55	88.55	88.55	88.55
3rd bending mode in xy	247.76	247.76	247.76	247.76	247.76	247.76	247.76	247.76
2nd bending mode in xz	351.26	351.24	110.52	91.78	90.02	89.85	89.83	89.83
4th bending mode in xy	485.03	485.03	485.03	485.03	485.03	485.03	485.03	485.03
1st torsional mode in x	607.33	607.33	607.33	607.33	607.33	607.33	607.33	607.33
5th bending mode in xy	800.86	800.86	800.86	800.86	800.86	800.86	800.86	800.86
3rd bending mode in xz	971.85	971.72	487.13	482.65	482.21	482.17	482.16	482.16
6th bending mode in xy	1194.90	1194.90	1194.90	1194.90	1194.90	1194.90	1194.90	1194.90
7th bending mode in xy	1667.10	1667.10	1667.10	1667.10	1667.10	1667.10	1667.10	1667.10
2nd torsional mode in x	1822.00	1822.00	1822.00	1822.00	1822.00	1822.00	1822.00	1822.00
4th bending mode in xz	1872.80	1872.30	1178.70	1176.90	1176.70	1176.70	1176.70	1176.70
1st longitudinal mode	2187.90	2187.90	2187.90	2187.90	2187.90	2187.90	2187.90	2187.90
8th bending mode in xy	2217.60	2217.60	2217.60	2217.60	2217.60	2217.60	2217.60	2217.60
9th bending mode in xy	2847.10	2847.10	2847.10	2847.10	2847.10	2847.10	2847.10	2847.10
5th bending mode in xz	3032.70	3031.50	2153.90	2152.90	2152.80	2152.80	2152.80	2152.80
3rd torsional mode in x	3036.70	3036.70	3036.70	3036.70	3036.70	3036.70	3036.70	3036.70
10th bending mode in xy	3556.70	3556.70	3385.90	3385.30	3385.20	3385.20	3385.20	3385.20

Table B3. Natural frequencies obtained with $\mathrm{K_{rotx}}$ variations ($\mathrm{K_{rotz}} = \mathrm{K_{roty}} = 1 \times 10^{20}$ Nm/rad and $\mathrm{K_{ux}} = \mathrm{K_{uy}} = \mathrm{K_{uz}} = 1 \times 10^{20}$ N/m).

Mode Description	Natural Frequency [Hz]							
	$\mathrm{K_{rotx}}$ 1×10^{20} Nm/rad	$\mathrm{K_{rotx}}$ 1×10^{10} Nm/rad	$\mathrm{K_{rotx}}$ 1×10^{5} Nm/rad	$\mathrm{K_{rotx}}$ 1×10^{4} Nm/rad	$\mathrm{K_{rotx}}$ 1×10^{3} Nm/rad	$\mathrm{K_{rotx}}$ 1×10^{2} Nm/rad	$\mathrm{K_{rotx}}$ 1×10^{1} Nm/rad	$\mathrm{K_{rotx}}$ 1 Nm/rad
1st bending mode in xy	14.14	14.14	14.14	14.14	14.14	14.14	14.14	14.14
1st bending mode in xz	56.48	56.48	56.48	56.48	56.48	56.48	56.48	56.48
2nd bending mode in xy	88.55	88.55	88.55	88.55	88.55	88.55	88.55	88.55
3rd bending mode in xy	247.76	247.76	247.76	247.76	247.76	247.76	247.76	247.76
2nd bending mode in xz	351.26	351.26	351.26	351.26	351.26	351.26	351.26	351.26
4th bending mode in xy	485.03	485.03	485.03	485.03	485.03	485.03	485.03	485.03
1st torsional mode in x	607.33	607.33	601.89	557.29	345.07	126.34	40.61	12.87
5th bending mode in xy	800.86	800.86	800.86	800.86	800.86	800.86	800.86	800.86
3rd bending mode in xz	971.85	971.85	971.85	971.85	971.85	971.85	971.85	971.85
6th bending mode in xy	1194.90	1194.90	1194.90	1194.90	1194.90	1194.90	1194.90	1194.90
7th bending mode in xy	1667.10	1667.10	1667.10	1667.10	1667.10	1667.10	1667.10	1667.10
2nd torsional mode in x	1822.00	1822.00	1805.70	1677.60	1334.70	1228.10	1216.00	1214.80
4th bending mode in xz	1872.80	1872.80	1872.80	1872.80	1872.80	1872.80	1872.80	1872.80
1st longitudinal mode	2187.90	2187.90	2187.90	2187.90	2187.90	2187.90	2187.90	2187.90
8th bending mode in xy	2217.60	2217.60	2217.60	2217.60	2217.60	2217.60	2217.60	2217.60
9th bending mode in xy	2847.10	2847.10	2847.10	2847.10	2847.10	2847.10	2847.10	2847.10
5th bending mode in xz	3032.70	3032.70	3032.70	3032.70	3032.70	3032.70	3032.70	3032.70
3rd torsional mode in x	3036.70	3036.70	3009.60	2812.00	2495.00	2436.10	2430.00	2429.40
10th bending mode in xy	3556.70	3556.70	3556.70	3556.70	3556.70	3556.70	3556.70	3556.70

Table B4. Natural frequencies obtained with $\mathrm{K_{roty}}$ variations ($\mathrm{K_{rotx}} = \mathrm{K_{rotz}} = 1 \times 10^{20}$ Nm/rad and $\mathrm{K_{ux}} = \mathrm{K_{uy}} = \mathrm{K_{uz}} = 1 \times 10^{20}$ N/m).

Mode Description	Natural Frequency [Hz]							
	$\mathrm{K_{roty}}$ 1×10^{20} Nm/rad	$\mathrm{K_{roty}}$ 1×10^{10} Nm/rad	$\mathrm{K_{roty}}$ 1×10^{5} Nm/rad	$\mathrm{K_{roty}}$ 1×10^{4} Nm/rad	$\mathrm{K_{roty}}$ 1×10^{3} Nm/rad	$\mathrm{K_{roty}}$ 1×10^{2} Nm/rad	$\mathrm{K_{roty}}$ 1×10^{1} Nm/rad	$\mathrm{K_{roty}}$ 1 Nm/rad
1st bending mode in xy	14.14	14.14	14.14	14.14	14.14	14.14	14.14	14.14
1st bending mode in xz	56.48	56.48	46.99	24.06	8.30	2.65	0.84	0.27
2nd bending mode in xy	88.55	88.55	88.55	88.55	88.55	88.55	88.55	88.55
3rd bending mode in xy	247.76	247.76	247.76	247.76	247.76	247.76	247.76	247.76
2nd bending mode in xz	351.26	351.25	306.71	259.05	248.28	247.07	246.95	246.94
4th bending mode in xy	485.03	485.03	485.03	485.03	485.03	485.03	485.03	485.03
1st torsional mode in x	607.33	607.33	607.33	607.33	607.33	607.33	607.33	607.33
5th bending mode in xy	800.86	800.86	800.86	800.86	800.86	800.86	800.86	800.86
3rd bending mode in xz	971.85	971.84	873.88	806.04	794.25	792.98	792.86	792.84
6th bending mode in xy	1194.90	1194.90	1194.90	1194.90	1194.90	1194.90	1194.90	1194.90
7th bending mode in xy	1667.10	1667.10	1667.10	1667.10	1667.10	1667.10	1667.10	1667.10
2nd torsional mode in x	1822.00	1822.00	1822.00	1822.00	1822.00	1822.00	1822.00	1822.00
4th bending mode in xz	1872.80	1872.80	1720.80	1644.00	1632.40	1631.20	1631.10	1631.10
1st longitudinal mode	2187.90	2187.90	2187.90	2187.90	2187.90	2187.90	2187.90	2187.90
8th bending mode in xy	2217.60	2217.60	2217.60	2217.60	2217.60	2217.60	2217.60	2217.60
9th bending mode in xy	2847.10	2847.10	2847.10	2847.10	2847.10	2847.10	2847.10	2847.10
5th bending mode in xz	3032.70	3032.70	2831.50	2751.20	2739.90	2738.80	2738.60	2738.60
3rd torsional mode in x	3036.70	3036.70	3036.70	3036.70	3036.70	3036.70	3036.70	3036.70
10th bending mode in xy	3556.70	3556.70	3556.70	3556.70	3556.70	3556.70	3556.70	3556.70

APPENDIX C

R-INDEX OF ANALYSIS OF SENSOR NUMBER AND POSITION

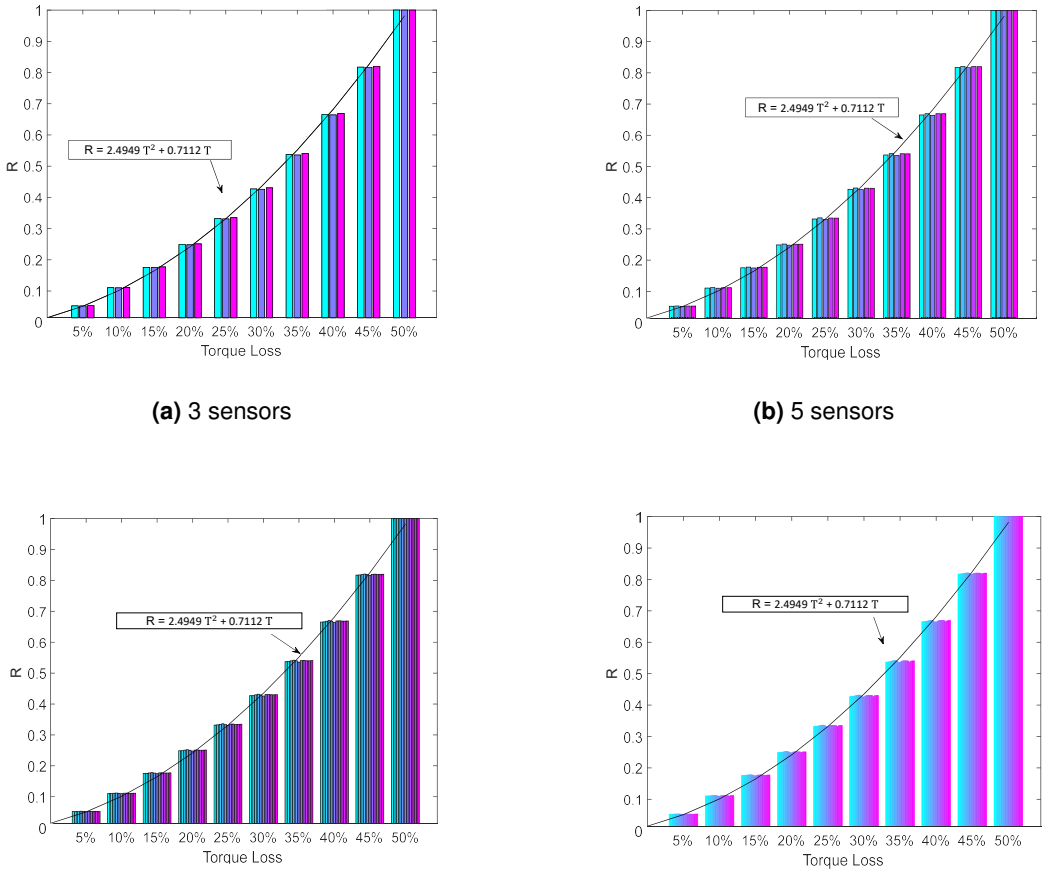

(a) 3 sensors

(b) 5 sensors

(c) 11 sensors

(d) 21 sensors

Figure C1. R-index for K_{uy} loss with sensors equally distributed and force applied at x = L/5.

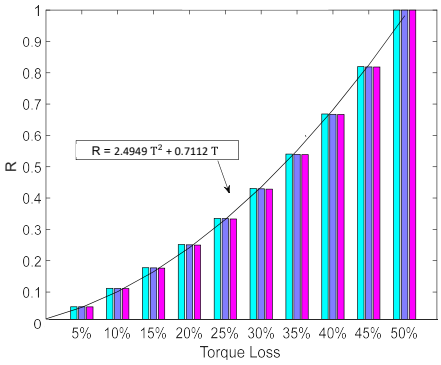

(a) 3 sensors

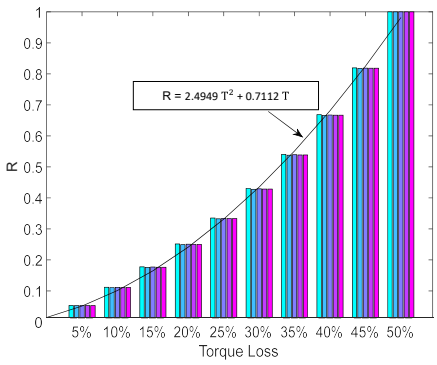

(b) 5 sensors

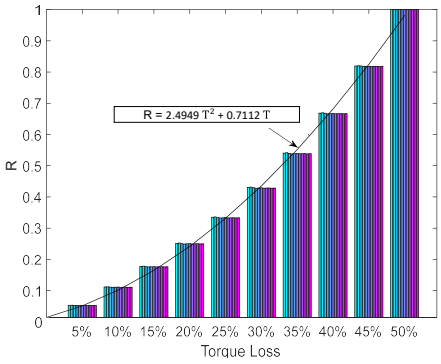

(c) 11 sensors

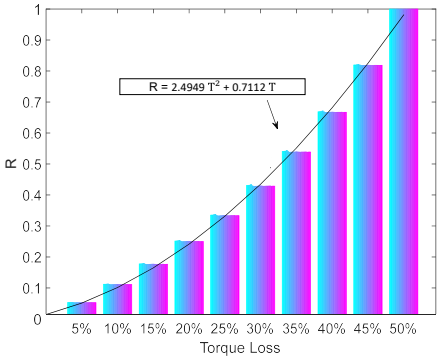

(d) 21 sensors

Figure C2. R-index for $\mathrm{K_{uy}}$ loss with sensors equally distributed and force applied at x = 2L/5.

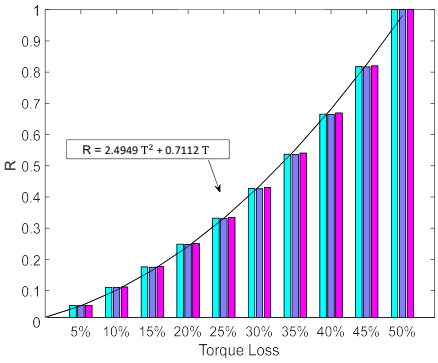

(a) 3 sensors

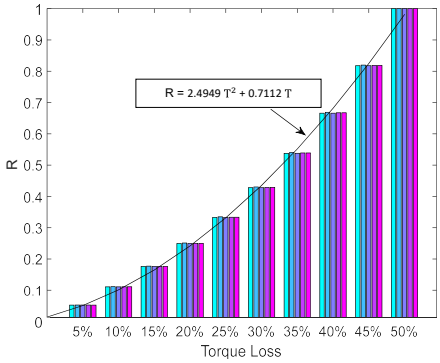

(b) 5 sensors

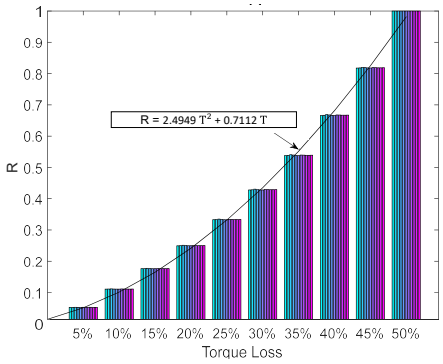

(c) 11 sensors

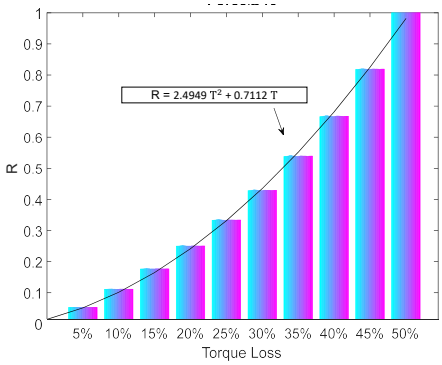

(d) 21 sensors

Figure C3. R-index for $\mathrm{K_{uy}}$ loss with sensors equally distributed and force applied at x = 3L/5.

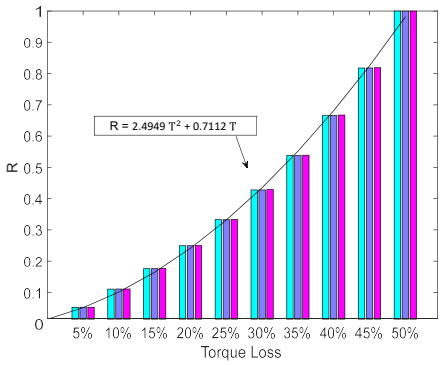

(a) 3 sensors

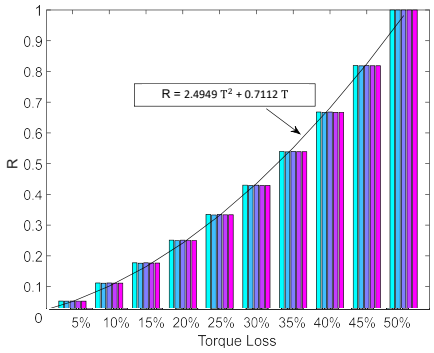

(b) 5 sensors

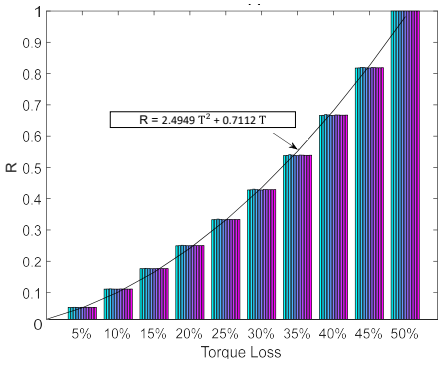

(c) 11 sensors

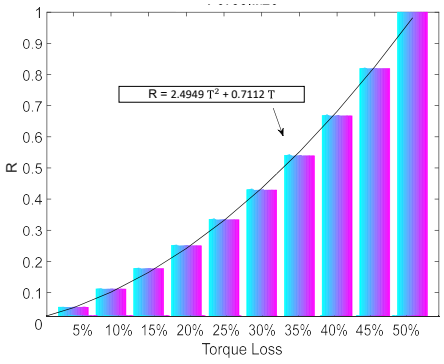

(d) 21 sensors

Figure C4. R-index for $\mathrm{K_{uy}}$ loss with sensors equally distributed and force applied at x = 4L/5.

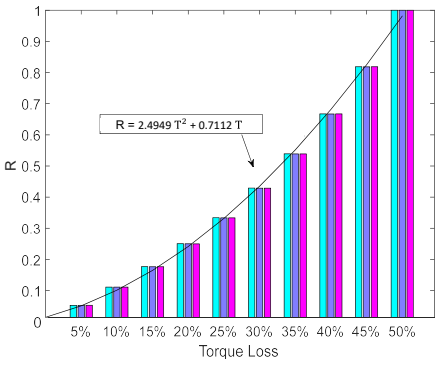

(a) 3 sensors

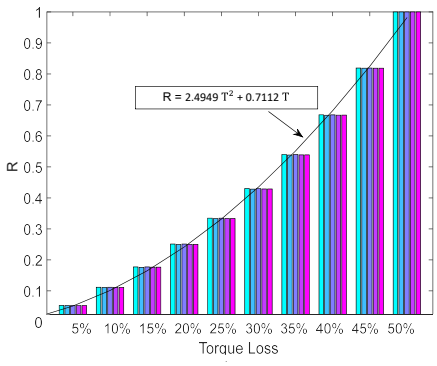

(b) 5 sensors

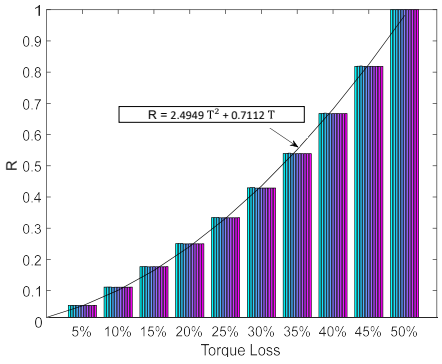

(c) 11 sensors

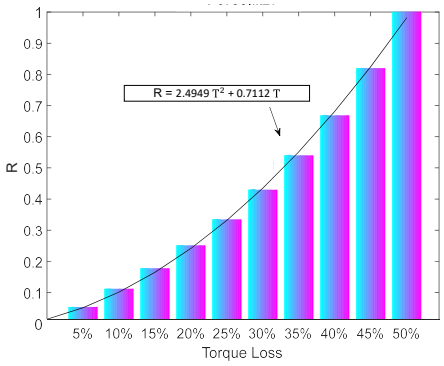

(d) 21 sensors

Figure C5. R-index for $\mathrm{K_{uy}}$ loss with sensors equally distributed and force applied at x = L.

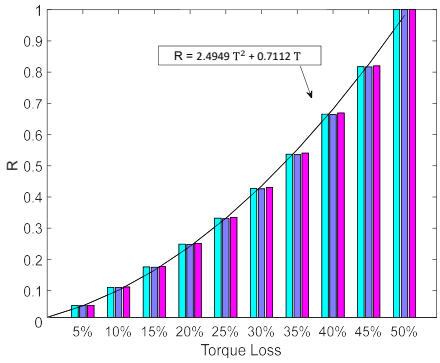

(a) 3 sensors

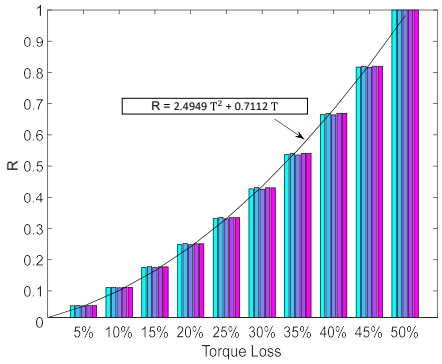

(b) 5 sensors

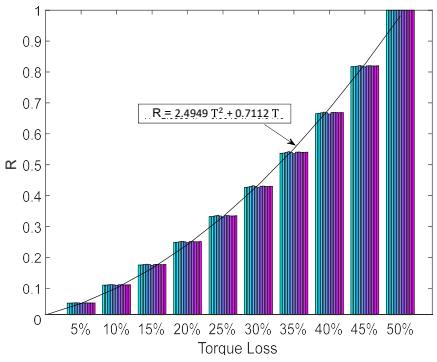

(c) 11 sensors

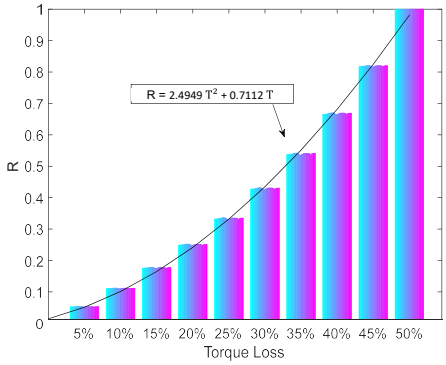

(d) 21 sensors

Figure C6. R-index for $\mathrm{K_{rotz}}$ loss with sensors equally distributed and force applied at x = L/5.

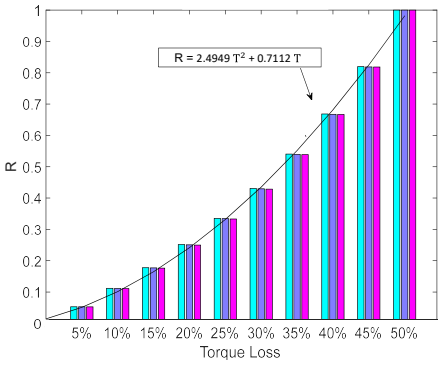

(a) 3 sensors

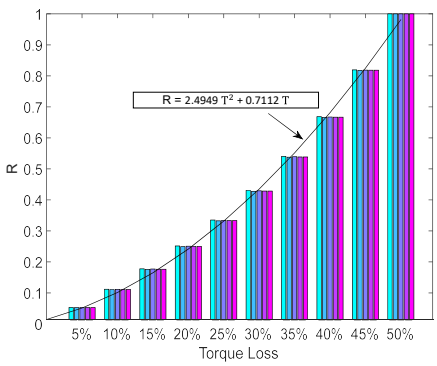

(b) 5 sensors

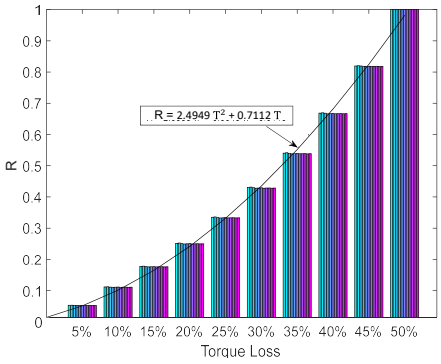

(c) 11 sensors

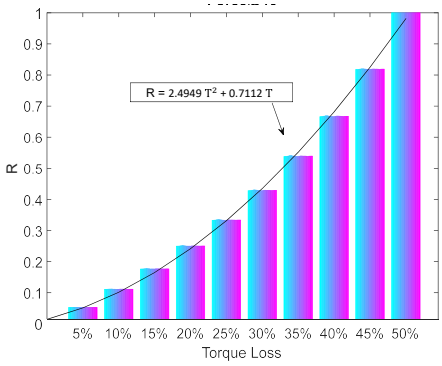

(d) 21 sensors

Figure C7. R-index for $\mathrm{K_{rotz}}$ loss with sensors equally distributed and force applied at x = 2L/5.

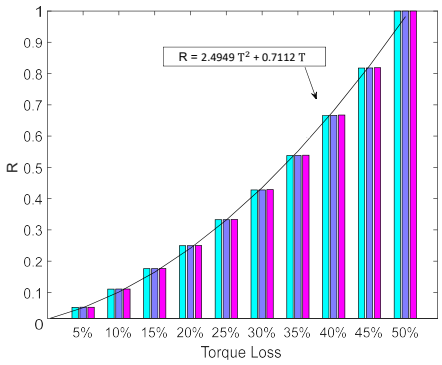

(a) 3 sensors

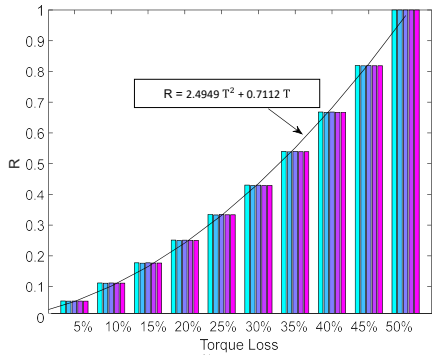

(b) 5 sensors

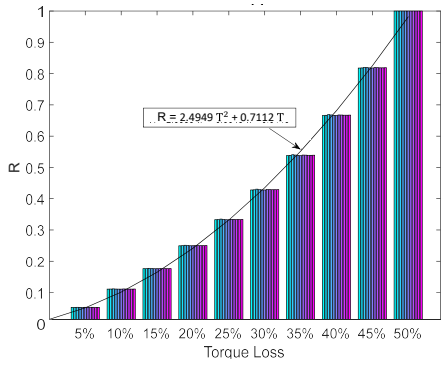

(c) 11 sensors

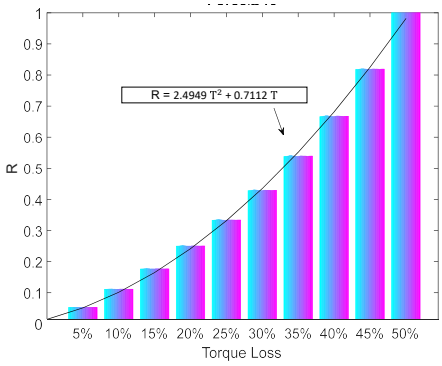

(d) 21 sensors

Figure C8. R-index for $\mathrm{K_{rotz}}$ loss with sensors equally distributed and force applied at x = 3L/5.

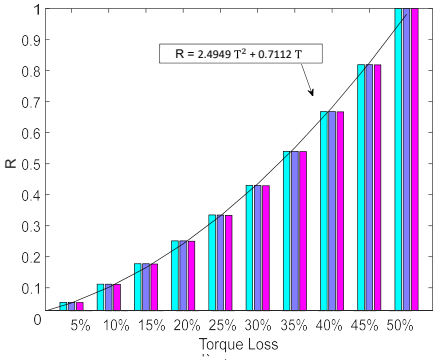

(a) 3 sensors

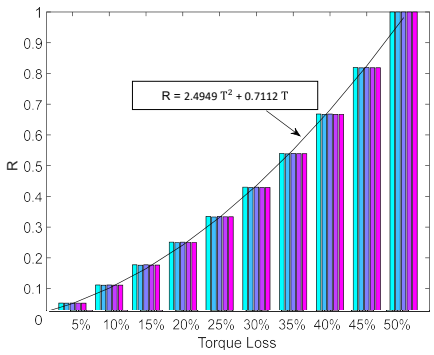

(b) 5 sensors

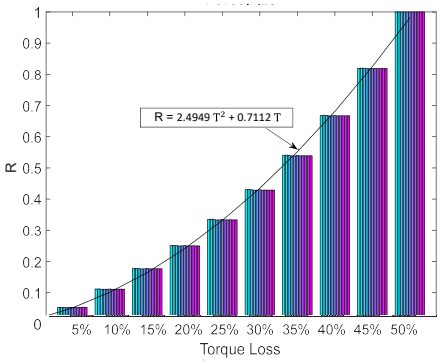

(c) 11 sensors

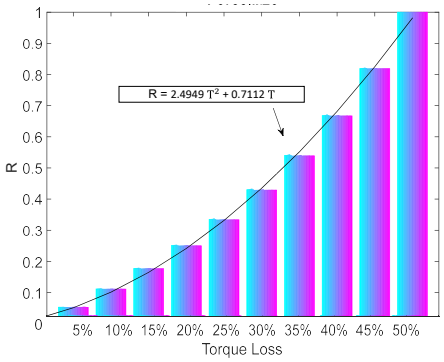

(d) 21 sensors

Figure C9. R-index for $\mathrm{K_{rotz}}$ loss with sensors equally distributed and force applied at x = 4L/5.

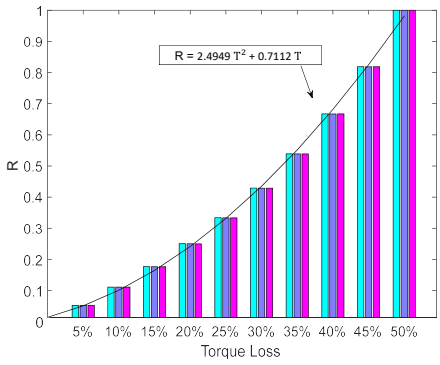

(a) 3 sensors

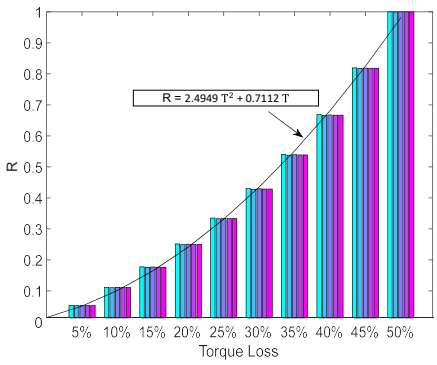

(b) 5 sensors

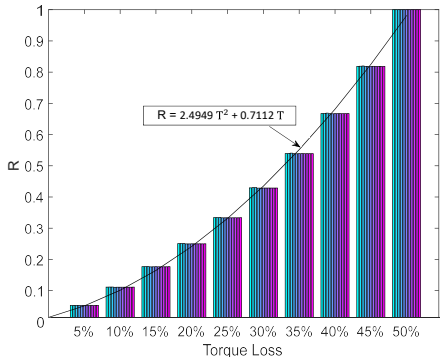

(c) 11 sensors

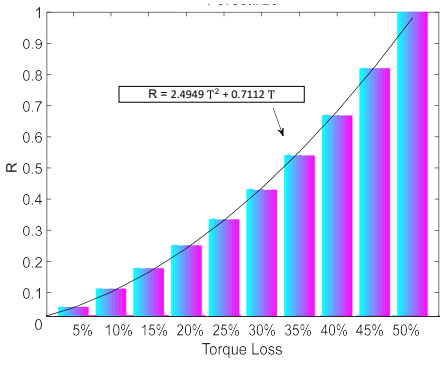

(d) 21 sensors

Figure C10. R-index for $\mathrm{K_{rotz}}$ loss with sensors equally distributed and force applied at x = L.

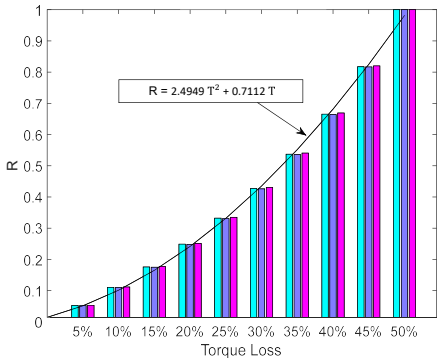

(a) 3 sensors

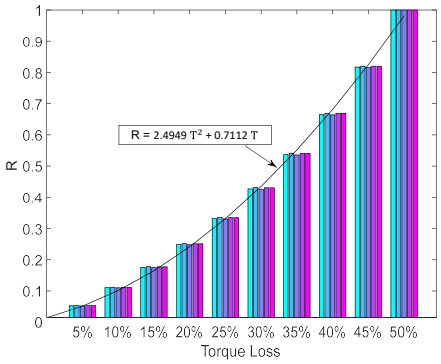

(b) 5 sensors

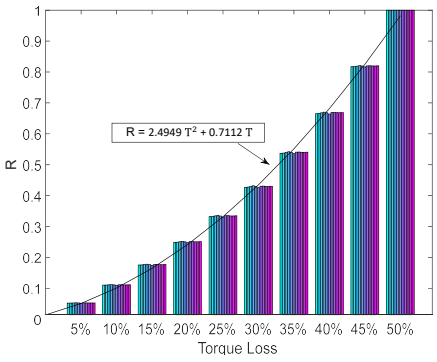

(c) 11 sensors

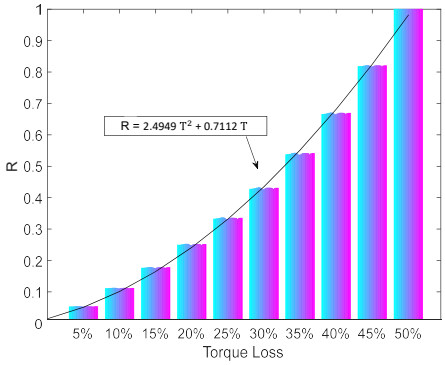

(d) 21 sensors

Figure C11. R-index for $\mathrm{K_{rotz}} - \mathrm{K_{uy}}$ loss with sensors equally distributed and force applied at x = L/5.

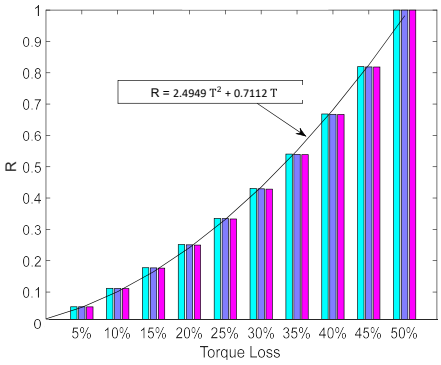

(a) 3 sensors

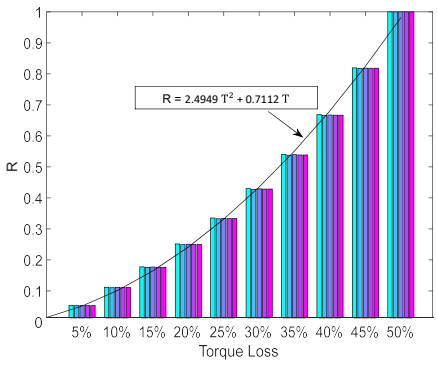

(b) 5 sensors

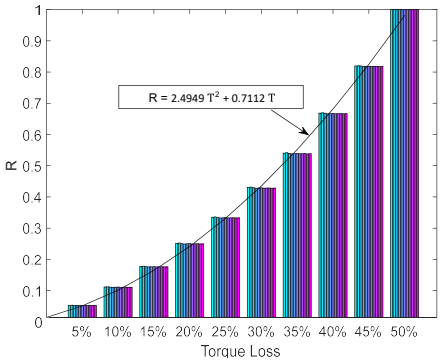

(c) 11 sensors

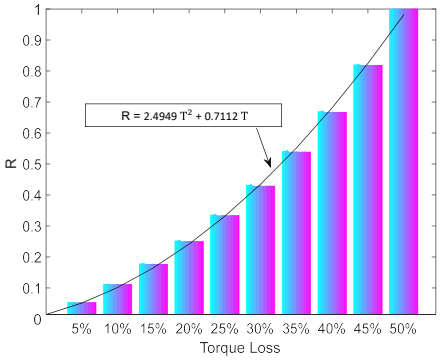

(d) 21 sensors

Figure C12. R-index for $\mathrm{K_{rotz}} - \mathrm{K_{uy}}$ loss with sensors equally distributed and force applied at x = 2L/5.

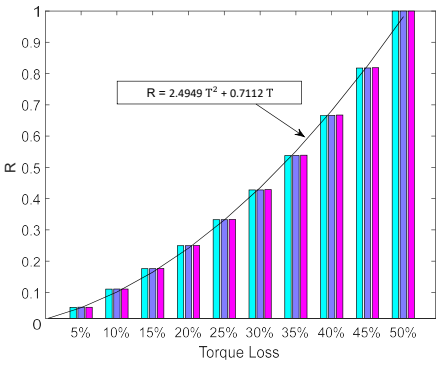

(a) 3 sensors

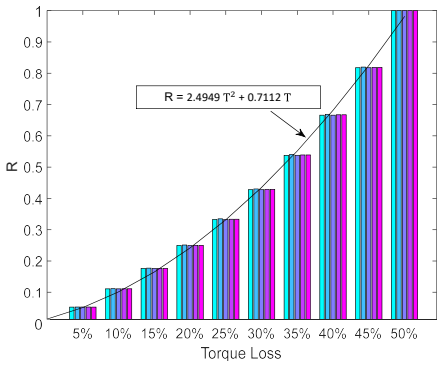

(b) 5 sensors

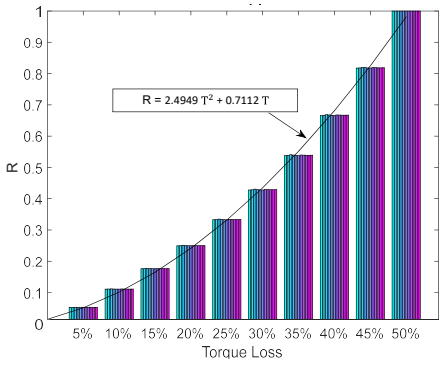

(c) 11 sensors

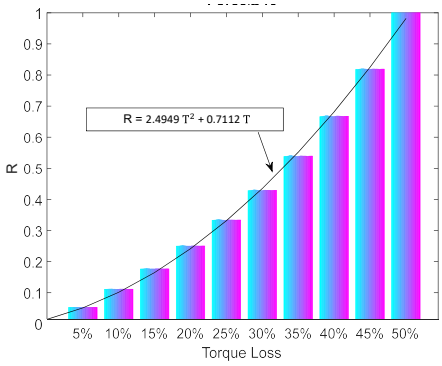

(d) 21 sensors

Figure C13. R-index for $\mathrm{K_{rotz}} - \mathrm{K_{uy}}$ loss with sensors equally distributed and force applied at x = 3L/5.

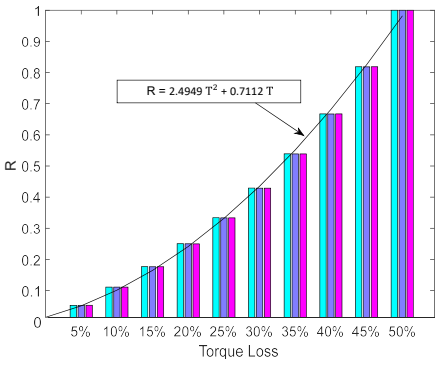

(a) 3 sensors

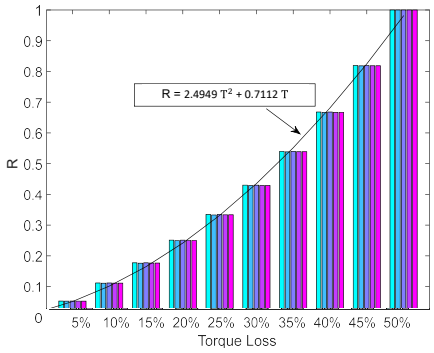

(b) 5 sensors

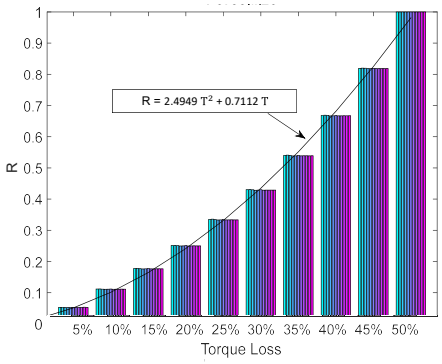

(c) 11 sensors

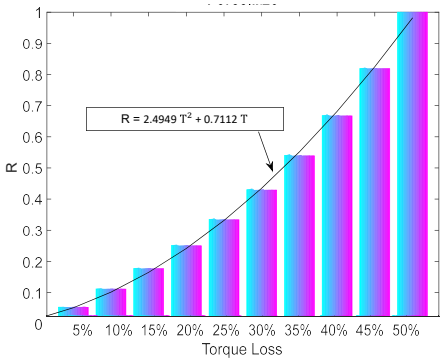

(d) 21 sensors

Figure C14. R-index for $\mathrm{K_{rotz}} - \mathrm{K_{uy}}$ loss with sensors equally distributed and force applied at x = 4L/5.

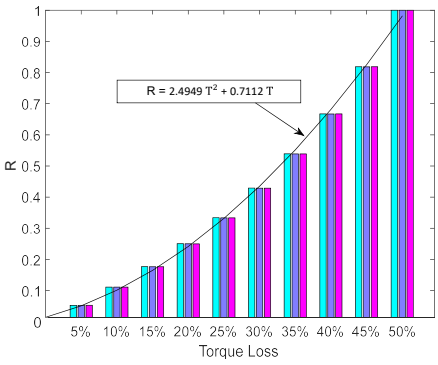

(a) 3 sensors

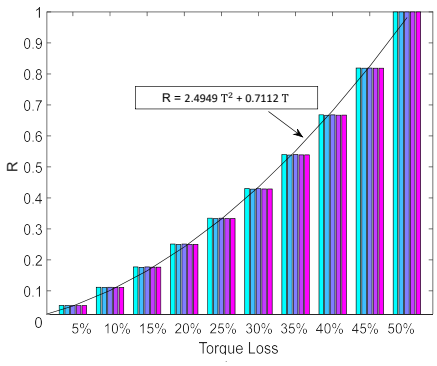

(b) 5 sensors

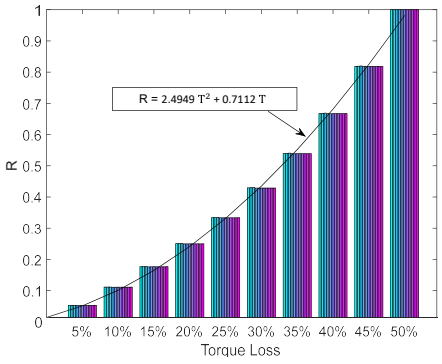

(c) 11 sensors

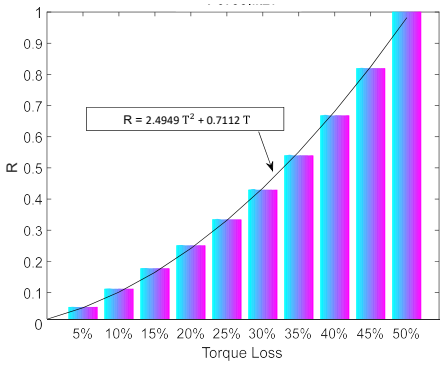

(d) 21 sensors

Figure C15. R-index for $\mathrm{K_{rotz}} - \mathrm{K_{uy}}$ loss with sensors equally distributed and force applied at x = L.